IMPROVING TARGETED RADIONUCLIDE THERAPY USING NUCLEAR NANOTECHNOLOGY

A Thesis

by

JORDAN ANDREW EVANS

Submitted to the Office of Graduate Studies of
Texas A&M University
in partial fulfillment of the requirements for the degree of

MASTER OF SCIENCE

Approved by:

Chair of Committee,	W. Dan Reece
Committee Members,	Robert Tribble
	Sreeram Vaddiraju
	Karen Wooley
Head of Department,	Yassin Hassan

May 2013

Major Subject: Nuclear Engineering

ABSTRACT

The objectives of this thesis are to produce radioactive antibody-conjugated gold nanoparticles to improve the efficacy of targeted radionuclide therapy for the treatment of cancer, and to demonstrate that this product can be produced at Texas A&M University.

We have proposed a method for determining the distribution of radioactive nuclei per nanoparticle, which is critical for determining radiotherapeutic efficacy. Using the distribution of radioactive nuclei per nanoparticle, we have produced methods for calculating the radiative dose to tissue using nano-improved targeted radionuclide therapy, but more importantly we propose procedures to experimentally determine the efficacy of targeted radionuclide therapy improved by application of radioactive nanomaterials in combination with immunotherapy, nanomaterial cytotoxicity, and other cancer therapies such as chemotherapy. These methods can also be used to determine the efficacy of combinatory treatments as a function of time.

Characterization of the antibody-nanoparticle attachment is critical; we have demonstrated successful antibody-nanoparticle conjugation using atomic force microscopy, dynamic light scattering, and agarose gel electrophoresis, providing more conclusive evidence of successful conjugation compared to flow cytometry.

We provide a mathematical derivation from basic electron-transport principles which demonstrates the theoretical dosimetric advantages of applying radioactive nanomaterials to targeted radionuclide therapy. The general formulae can be applied to

any tumor size, any radionuclide, and any pharmacokinetic nanoparticle distribution throughout the body, ultimately allowing a quick method of approximating the necessary activation time and treatment dosage parameters for a specific patient without burdensome Monte Carlo computational simulations.

We further demonstrated that nano-TRT dosage to tumors should be considered as a function of radial position rather than average, as the dose across the tumor may be noticeably non-uniform causing some portions of the tumor to receive (potentially) significantly less dose than average.

ACKNOWLEDGEMENTS

I would like to thank my committee chair, Dr. W. Dan Reece, and my committee members, Dr. Karen Wooley, Dr. Robert Tribble, and Dr. Sreeram Vaddiraju for their guidance, support, and collaboration throughout this research.

We collaborated with several important TAMU members throughout this research project. I would like to thank Dr. Gamal Akabani for the use of his BSL2 laboratory, Dr. Craig Marianno for the use of his HPGe, Dr. Jeffrey Raymond with AFM, Dr. Mahmoud El Sabahy with DLS and electrophoresis imaging, Dr. Reece for the use of the Nuclear Science Center, Dr. Wooley for the use of her chemical laboratory, and Mr. Bill Merka for sealing the quartz vials in preparation for neutron activation experiments.

I would like to thank my friends, particularly Michael Hackemack, Spencer Mickum, and Ben Sheppard, and especially my parents Wayne and Gesine Evans and brothers Joshua and Justin Evans for their continued support and positive influence throughout my life and educational career. I would also like to thank my fiancée Maria Cáceres for her patience, understanding, and support throughout the course of my graduate career.

NOMENCLATURE

A_0	Saturation Activity
A_B	Activity of Isotope "B" (^{198}Au) at Time = $t_{irr} + t_d$
AFM	Atomic Force Microscopy
ATCC	American Type Culture Collection
AuNPs	Gold Nanoparticles
Bq	Becquerel
CD	Cluster of Differentiation
Ci	Curie
CoA	Certificate of Analysis
DLS	Dynamic Light Scattering
EGFR	Epidermal Growth Factor Receptor
Fab Region	Fragment Antigen-Binding Region (Antibody)
Fc Region	Fragment Crystallizable Region (Antibody)
FDA	Food and Drug Administration
FRET	Förster Resonance Energy Transfer
GBM	Glioblastoma Multiforme
HER2	Human Epidermal Growth Factor Receptor Type 2
HPGe	High Purity Germanium Detector
I_∞	Resonance Integral
IARC	International Agency for Research on Cancer

IMRT	Intensity Modulated Radiation Therapy
k	Mean Number of ^{198}Au Nuclei per AuNP
kD	Kilodalton
LET	Linear Energy Transfer
mAb	Monoclonal Antibody
MRI	Magnetic Resonance Imaging
MURR	University of Missouri Research Reactor
N_A	Number of Nuclei of Isotope "A" (^{197}Au)
NAA	Neutron Activation Analysis
NCI	National Cancer Institute
NHS	N-hydroxysuccinimide
NHL	Non-Hodgkin's Lymphoma
NIH	National Institutes of Health
NIST	National Institute of Standards and Technology
NSC	Nuclear Science Center (Texas A&M University)
P	Probability of Randomly Selecting an AuNP with "λ" ^{198}Au Nuclei from a Population of AuNPs whose Average Number of ^{198}Au is "k"
PBS	Phosphate Buffered Saline
PDF	Probability Distribution Function
PDI	Polydispersity Index
PE	R-phycoerythrin
QC	Quality Control

RCF	Relative Centrifugal Force
RPDF	Relative Probability Distribution Function
SEER	Surveillance Epidemiology and End Results
SPR	Surface Plasmon Resonance
TAE	Triethanolamine Buffer
TAMU	Texas A&M University
t_d	Decay Time After Irradiation
TEM	Transmission Electron Microscopy
t_{irr}	Irradiation Time
TRT	Targeted Radionuclide Therapy
XRT	External Beam Radiation Therapy
λ	Number of ^{198}Au Nuclei in a AuNP
σ_{2200}	2200 m/s Cross Section
σ_s	Neutron Scattering Cross Section
ϕ_{2200}	2200 m/s Neutron Flux
ϕ_{epi}	Epithermal Neutron Flux

TABLE OF CONTENTS

Page

ABSTACT ii

ACKNOWLEDGEMENTS iv

NOMENCLATURE v

TABLE OF CONTENTS viii

LIST OF FIGURES x

LIST OF TABLES xv

1. INTRODUCTION 1

    1.1 Targeted Radionuclide Therapy 1
    1.2 Medical Applications of Nanotechnology 4
    1.3 Paradigm Shift - Improving TRT Using Nuclear Nanotechnology 8
    1.4 Cancer Cell Line Investigated in This Study 14
    1.5 Nano-Improved TRT: Final Product Design 15

2. METHODS 17

    2.1 Preliminary Nanoparticle Properties and Characterization 17
    2.2 Neutron Activation Preparation 19
    2.3 Neutron Activation Analysis 21
    2.4 Radioactive Nanoparticle Structural Integrity 22
    2.5 Nuclear Probability Theory: Radioactive Nuclei per Nanoparticle 23
    2.6 Nanoparticle-Antibody Directional Conjugation 26
    2.7 Conjugated Nanoparticle Characterization 28
    2.8 Radioactive Nanoparticle Dosimetry 31
    2.9 Cell Culture 33
    2.10 Flow Cytometry and Fluorescent Microscopic Analysis 34
    2.11 Cell Characterization and Growth Response Analysis 36

3. RESULTS AND DISCUSSION 39

3.1 Small (10 nm & 17 nm Diameter) AuNP Failures 39
3.2 AuNP Agglomeration and Failure Mechanisms 44
3.3 Changing AuNP Size and Surface Energy 46
3.4 Changing Reactor Conditions 49
3.5 Calculated Radioactive Nuclei per 100 nm Diameter Nanoparticle 51
3.6 Final AuNP Activation: 100 nm Diameter without Aluminum Foil 53
3.7 Flow Cytometry Characterization 54
3.8 Gel Electrophoresis Characterization and mAb-AuNP Conjugation 60
3.9 Cytotoxic Effects of Non-Radioactive AuNPs 64
3.10 AuNP Endocytosis 75

4. DERIVATION OF TRT DOSIMETRY USING PROBABILITY THEORY 77

4.1 Tumor Dosimetry Derivation of Endocytosed Nano-TRT 81
4.2 Dose as a Function of Radius 103
4.3 Generic Case Study: 1 cm Diameter Tumor 109

5. FUTURE WORK 112

6. SUMMARY 116

7. REFERENCES 118

APPENDIX 131

LIST OF FIGURES

Page

Figure 1.1 Comparison between Tissue Affected by Radiation in XRT vs. TRT 2

Figure 1.2 Band Structure of Metal Materials 4

Figure 1.3 Illustration of Nanoparticle SPR 5

Figure 1.4 Illustration of FRET 7

Figure 1.5 Example FRET Absorption/Emission Spectra 7

Figure 1.6 Illustration of TRT vs. Nano-Improved TRT 10

Figure 1.7 ^{198}Au Decay Chain 12

Figure 1.8 ^{198}Au Beta Decay Spectrum 13

Figure 1.9 Proposed Final Design, Complete with Radioactive AuNP Core and Attached mAbs 16

Figure 2.1 TEM Image of 17 nm AuNPs Upon Arrival 18

Figure 2.2 TEM Image of 10 nm AuNPs Upon Arrival 19

Figure 2.3 AuNP Neutron Activation Vial Assembly 20

Figure 2.4 Poisson Distribution of Calculated ^{198}Au Nuclei per AuNP Given t_{irr} = 12 h and t_d = 6 h, 10 nm vs. 17 nm 25

Figure 2.5 Antibody Schematic with the Fab Region, and the Fc Region 26

Figure 2.6 Antibody-Cell Attachment Schematic with Fab-Receptor Interaction 27

Figure 2.7 AFM Cantilever and Pointed Tip 30

Figure 2.8 Diagram of AFM Components 31

Figure 2.9 Calculated Dose from Primary β^- Emission vs. 17 nm AuNPs per Cell, Assuming Infinite AuNP Residence Time Approximation 33

Figure 2.10 Microscope Image of Cultured SK-BR-3 Adenocarcinoma Cells 34

Figure 2.11 Flow Cytometer Operating Principles 35

Figure 2.12 PE Absorption and Emission Spectra 36

Figure 2.13 Illustration of xCELLigence System Impedance Variability due to Cell Adhesion 38

Figure 3.1 10 nm Cytodiagnostics AuNPs Before and After Activation, and 5 Week Old Non-Activated 17 nm Nanopartz AuNPs Adhering to Vial ... 40

Figure 3.2 Measured ^{198}Au Nuclei per 17 nm Nanopartz AuNP 41

Figure 3.3 2D and 3D Images of Unconjugated 17 nm Nanopartz AuNPs 42

Figure 3.4 2D and 3D Images of mAb-Conjugated 17 nm Nanopartz AuNPs 42

Figure 3.5 The Surface of a Material with Dangling Bonds 47

Figure 3.6 Discrete Poisson Distribution of Calculated ^{198}Au Nuclei per 100 nm Diameter AuNP Given t_{irr} = 1 h, and t_d = 24 h in TAMU NSC Nuclear Reactor 52

Figure 3.7 Calculated Dose from Primary β^- Emission of TAMU NSC-Activated 100 nm AuNPs vs. 100 nm AuNPs per Cell, Given t_{irr} = 1 h, and t_d = 24 h, Assuming Infinite AuNP Residence Time Approximation 53

Figure 3.8 Absorbance vs. Excitation Wavelength Spectrum of 10 nm AuNPs Using UV-Vis Spectroscopy, with Accuri C6 Flow Cytometer Excitation Lasers Superimposed 55

Figure 3.9 Absorbance vs. Excitation Wavelength Spectrum of 100 nm AuNPs Using UV-Vis Spectroscopy, with Accuri C6 Flow Cytometer Excitation Lasers Superimposed 55

Figure 3.10 Absorbance vs. Excitation Wavelength Spectrum of PE CD340 mAbs, with Accuri C6 Flow Cytometer Excitation Lasers

Superimposed 56

Figure 3.11 Flow Cytometry Scattering of Stock Bare 10 nm and 100 nm AuNPs 57

Figure 3.12 Flow Cytometry Scattering of Stock Bare PE CD340 mAbs 58

Figure 3.13 Flow Cytometry Scattering of PE CD340-Conjugated 100 nm AuNPs .. 59

Figure 3.14 Flow Cytometry Scattering of SK-BR-3 Cancer Cells Alone 60

Figure 3.15 Agarose Gel Electrophoresis with Bare 10 nm AuNPs, Bare 100 nm AuNPs, and PE CD340 Alone 61

Figure 3.16 Figure 3.15 with Resolved Contrast; Bare 10 nm AuNPs, Bare 100 nm AuNPs, and Lanes 11-15 Cropped Out 62

Figure 3.17 Agarose Gel Electrophoresis with PE CD340-Conjugated 100 nm AuNPs, Bare 100 nm AuNPs, and PE CD340 Alone 63

Figure 3.18 Close-Up Resolution-Resolved Views of Lanes 1-5 of Fig. 3.19 with PE CD340-Conjugated 100 nm AuNP, Lanes 6-10 of Fig. 3.19 with Bare 100 nm AuNPs, Lanes 11-15 of Fig. 3.19 with and PE CD340 Alone 64

Figure 3.19 Legend Non-Radioactive 10 nm AuNP Cytotoxicity Experiment, 8x2 Labeled Wells 66

Figure 3.20 Non-Radioactive 10 nm AuNP Cytotoxicity Experiment, Mean Cell Index vs. Time 67

Figure 3.21 Non-Radioactive 10 nm AuNP Cytotoxicity Experiment, Mean Cell Index vs. Time of 250,000 AuNPs/Cell and Zero AuNPs/Cell 70

Figure 3.22 Legend for Non-Radioactive 100 nm AuNP Cytotoxicity Experiment, 8x2 Labeled Wells 71

Figure 3.23 Non-Radioactive 100 nm AuNP Cytotoxicity Experiment, Mean Cell Index vs. Time 74

Figure 3.24 Illustration of Receptor-Mediated Nanoparticle Endocytosis 76

Figure 4.1 Schematic of Radioactive AuNP Geometry inside Cancerous

Cell/Tumor 79

Figure 4.2 β Range vs. Energy in Human Tissue 82

Figure 4.3 ^{198}Au β Energy Distribution and Approximate Polynomial Function..... 83

Figure 4.4 ^{198}Au β Range Distribution and Approximate Polynomial Function..... 84

Figure 4.5 Solid Angle in Spherical Coordinates 87

Figure 4.6 Incorrect Angular Distribution, with $w(\theta) = w(\varphi) = 1$ 88

Figure 4.7 Correct Angular Distribution, with $w(\varphi) = 1, w(\theta) = \sin(\theta)$..... 88

Figure 4.8 Spherical Volume such that the Distance to the Surface in the Upward Direction is between "c" and "dc" 91

Figure 4.9 Change of Variables from "r" to "c" for Particle Isotropy and Spherical Symmetry 92

Figure 4.10 $P(c)$ vs. c for Particle Isotropy in a Sphere 93

Figure 4.11 Illustration of β Path through Tissue 98

Figure 4.12 Illustration of Tumor and Surrounding Healthy Tissue 101

Figure 4.13 Tumors B and D with Exposed Healthy Surrounding Tissue 104

Figure 4.14 Illustration of Tumor D Dose vs. Radius 105

Figure 4.15 Approximate Dose to Cancerous Tissue vs. Radial Position, $b = 0.1R$..... 108

Figure 4.16 Approximate Dose to Cancerous Tissue vs. Radial Position, $b = R$..... 108

Figure 4.17 Distribution of ^{198}Au Nuclei per 50 nm AuNP for General Case Study..... 111

Figure 5.1 Discrete Poisson Distribution of Calculated ^{198}Au Nuclei per 100 nm Diameter AuNP Given t_{irr} = 10 min, and t_d = 24 h in the MURR.... 114

Figure 5.2 Calculated Dose from Primary β^- Emission of MURR-Activated

100 nm AuNPs vs. 100 nm AuNPs per Cell, Given t_{irr} = 10 min, and t_d = 24 h, Assuming Infinite AuNP Residence Time Approximation 115

LIST OF TABLES

Page

Table 2.1 CoA Measured AuNP Characteristics (Nanopartz)..... 18

Table 2.2 CoA Calculated AuNP Characteristics (Nanopartz) 18

Table 3.1 Neutron Interaction Cross Sections for AuNP Surfactant Nuclei vs. Natural Gold and Natural Aluminum 46

Table 3.2 Size-dependent Surface Energy for 1 g of Three Different Sized Gold Spheres 48

Table 3.3 Non-Radioactive 10 nm AuNP Cytotoxicity Experiment, Well Layout Information at Initiation of Treatment 65

Table 3.4 Non-Radioactive 100 nm AuNP Cytotoxicity Experiment, Well Layout Information at Initiation of Treatment 72

Table 4.1 Energy Deposition and Dosimetry Ratios of Cancerous vs. Surrounding Healthy Tissue Subject to Nano-TRT 103

LIST OF EQUATIONS

Page

Equation 1.1 Au^{197} to Au^{198} Nuclear Reaction Equation 11

Equation 1.2 Au^{198} Nuclear Decay Equation 11

Equation 2.1 Neutron Activation Analysis Equation for the Calculation of the Time-Dependent Population of Nuclide "B" 21

Equation 2.2 Neutron Activation Analysis Equation for Saturation Activity 21

Equation 2.3 The Poisson Distribution 24

Equation 4.1 Law of Cosines 79

Equation 4.2 β Energy vs. Range through Human Tissue 81

Equation 4.3 β Stopping Power through Human Tissue 81

Equation 4.4 ^{198}Au β Energy Distribution Polynomial Approximation 83

Equation 4.5 ^{198}Au β Range Distribution Polynomial Approximation 84

Equation 4.6 Discrete Single Variable Weight Function Average 85

Equation 4.7 Continuous Single Variable Weight Function Average 85

Equation 4.8 General Formula for a PDF using Weight Functions 85

Equation 4.9 PDF of "c" 92

Equation 4.10 Average Energy Deposited to Healthy vs. Cancerous Tissue 95

Equation 4.11 β Energy Deposited to Healthy Surrounding Tissue vs.

Variable Range through Human Tissue 97

Equation 4.12 "g" Factor for Large Tumors 99

Equation 4.13 General Formula for Nano-TRT Average Energy Deposited to Healthy Surrounding Tissue 99

Equation 4.14 Mass of Healthy Surrounding Tissue 100

Equation 4.15 General Formula for Average Nano-TRT Dose to Surrounding Healthy Tissue 102

Equation 4.16 Dose vs. Radial Position 107

1. INTRODUCTION

The 2012 Surveillance Epidemiology and End Results (SEER) report published by the National Cancer Institute (NCI) estimates that 848,170 men, and 790,740 women in the United States of America will be diagnosed with some form of cancer in 2012, and 577,190 people will die of cancer [1]. Common cancer treatments include chemotherapy, surgery, brachytherapy, and external beam radiation therapy (XRT). These treatments are not ideal, as they either do not discriminate healthy tissue from cancerous tissue (i.e. chemotherapy), or are confined to and treat only a small area of tissue (i.e. surgery or XRT). More effective, more targeted treatment options are necessary for patients afflicted with cancerous minimal residual disease or disseminated cancerous disease, as these conditions cannot be treated effectively by focusing on one portion of the body, nor by treating the entire body (and therefore subjecting the entire body to potentially lethal doses of treatment).

1.1 Targeted Radionuclide Therapy

Targeted radionuclide therapy (TRT) is attractive in that radioactive materials are designed to seek and destroy molecular and functional targets in the patient's cancerous tissue, augmenting the lethality to cancerous tissue while greatly reducing the effects to healthy surrounding tissue (see Figure 1.1 highlighting the tissues affected by radiation). TRT uses a targeting agent to transport a radioactive short-ranged nuclide to cancerous tissue. Monoclonal antibodies (mAbs), for example, are synthesized by identical

immune cells and are clones of the same parent cell. For this reason, mAb can be used to guide cancer treatment agents, since they preferentially bind to cancer cell-specific receptors.

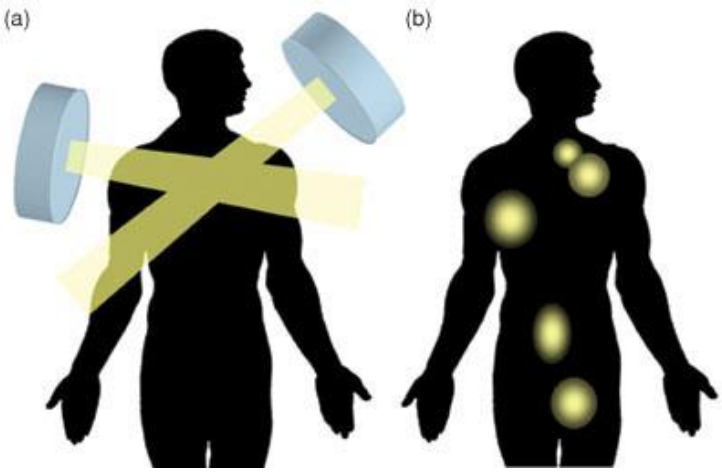

Fig. 1.1: Comparison between Tissue Affected by Radiation (yellow) in XRT (a) vs. TRT (b) [2]

A cancer may overexpress cell surface molecules known as clusters of differentiation (CD), which act as receptors or ligands. These CDs are unique to certain cancer tissues, and can be used as targets for mAb-based therapies [3]. By using α or β^- emitting radionuclides, which travel a short distance in human tissue in comparison to photons, radiative emissions will traverse and damage cancerous tissue and stop only microns to millimeters in surrounding healthy tissue. The effectiveness of TRT is primarily dependent upon three factors [4, 5]:

1. The affinity for the mAb to bind with tumor cells.

2. The physical and chemical characteristics of the radionuclide/mAb. These include factors such as the radionuclide physical half-life, the mAb biological half-life and retention time, the mAb uptake rate, and the rejection rate of mAb from tissues.
3. Treatment planning and administration. The effectiveness of TRT is a strong function of the choice of radionuclide, as well as type and dosage of other treatments used in combination with TRT.

Diseases for which TRT may be particularly effective include leukemias, lymphomas, cancerous metastases, and cancers which have invaded the body's lymph nodes. Two current examples of TRT treatments in the United States approved by the US Food and Drug Administration (FDA) are Zevalin and Bexxar [6]. These medications both treat non-Hodgkin's Lymphoma (NHL) by combining a beta-emitting radionuclide (^{90}Y for Zevalin, ^{131}I for Bexxar) and a mAb designed to attach to the CD20-positive receptor of afflicted cells. Though this new generation of monoclonal antibody-based therapies directly targets tumor cells, further research is necessary to increase the efficacy of these treatments. Many methods of TRT enhancement are currently under investigation, including augmentation of effector functions, direct and indirect arming, delaying mAb decomposition, and pre-targeting of radionuclides [7].

1.2 Medical Applications of Nanotechnology

Recent advances allow the synthesis of materials with one or more dimensions on the nanometer scale that can be used to treat or diagnose human diseases. The field of nanomedicine can, in fact, be defined as the design and implementation of nanomaterials to improve detection, treatment, and monitoring of disease. Since nanomaterials can be designed to perform multiple simultaneous biochemical functions at the nanometer scale, nanomedicine has become the focus of many research efforts, especially for the diagnosis and treatment of cancer [8].

One recent application of nanomedicine is the variation in photon interaction cross sections for nanoparticles depending on the particle size. Metallic materials have electrons which do not have to overcome a Fermi Gap to move from the valence band to the conduction band, shown below in Figure 1.2.

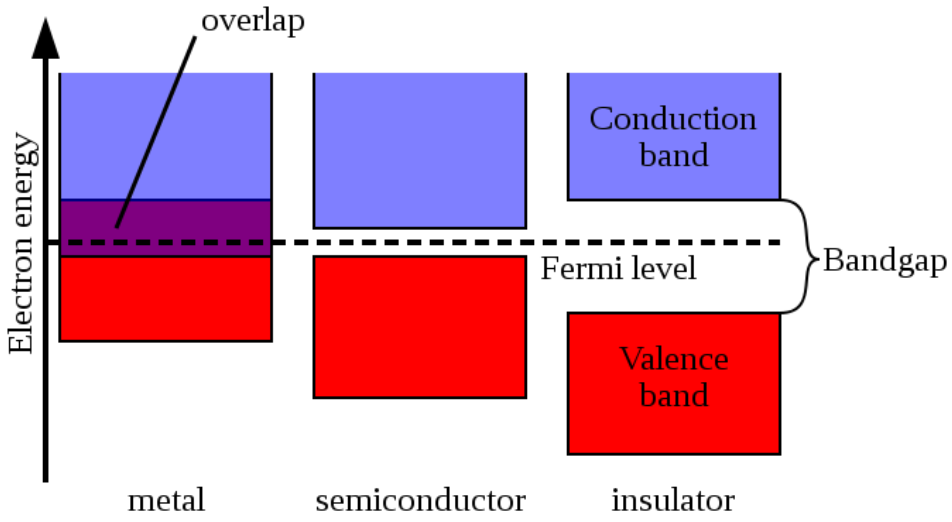

Fig. 1.2: Band Structure of Metal (Left) Materials [9]

When metallic nanoparticles are bombarded with electromagnetic radiation, the electron cloud can respond by oscillating in the constrained nano-scale structure in one large cohesive group. These collective oscillations of the nanoparticle electron cloud induced by electromagnetic waves can dramatically affect the material's photon interaction cross sections, a phenomenon known as surface plasmon resonance (SPR) [10]. Figure 1.3 illustrates SPR below, where the purple line represents the electric field component of the Poynting vector, the dark blue circles represent the physical metal nanoparticle, and the light blue represents the nanoparticle electron cloud responding to the incident oscillating electromagnetic field.

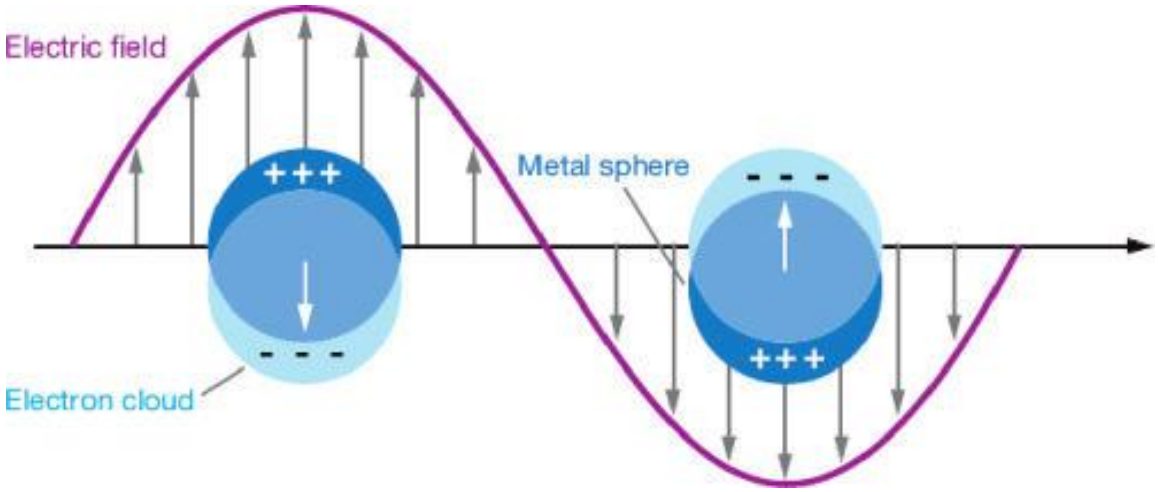

Fig. 1.3: Illustration of Nanoparticle SPR [11]

Binding a suitable nanoparticle with certain proteins and exciting the system with the appropriate wavelength of light yields a phenomenon known as Förster resonance energy transfer (FRET); the nanoparticle (aka “donor”) absorbs the incident photon and transfers the energy to its bound fluorophore (aka “acceptor”) via virtual photon energy transfer, which then emits the energy in the form of a photon [12]. Figures 1.4 and 1.5 below illustrate the FRET process, as well as the resulting absorption/emission spectra. FRET can be used to amplify extremely faint signals in real-time with high spatial resolution, and could potentially be useful for characterizing the nanomaterials involved in this research [13-17].

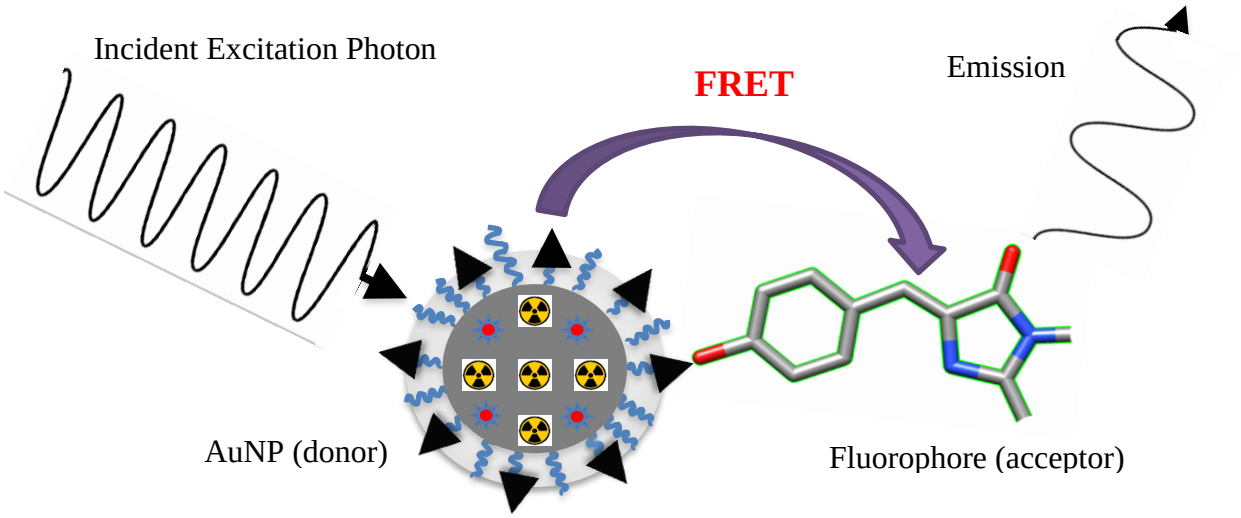

Fig. 1.4: Illustration of FRET

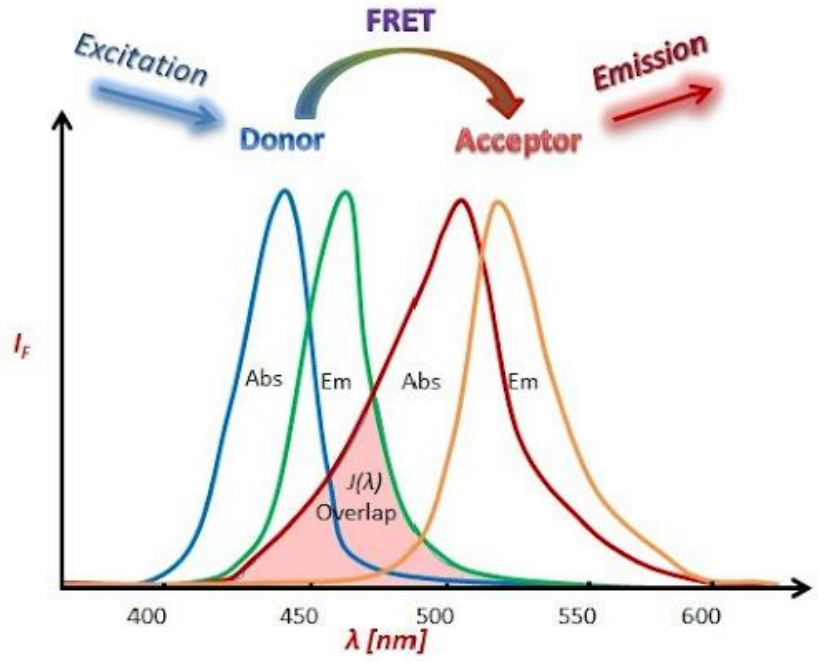

Fig. 1.5: Example FRET Absorption/Emission Spectra

In addition to nanoparticle-photon interactions, iron oxide nanoparticles are used as contrast agents in magnetic resonance imaging (MRI) exams due to their ability to change spin-spin relaxation times of neighboring water molecules, thereby enhancing the signal to noise ratio to provide clearer diagnostic images of the patient [18]. Biodegradable nanoparticles have been developed recently as drug carriers to administer a range of drugs to varying parts of the body for sustained periods of time [19]. Single-walled carbon nanotubes were recently used to transport cancer treatment into effected tissues using near-infrared radiative stimulation [20]. Magnetic nanoparticles can be subjected to an AC magnetic field, causing them to heat up within a patient's tumor tissue to induce hyperthermia that has been shown to enhance the therapeutic effect of cancer treatments such as XRT [21]. Though biochemical applications of nanomedicine are under intense investigation, further research is necessary to develop and improve radiotherapy.

1.3 Paradigm Shift - Improving TRT Using Nuclear Nanotechnology

Novel cancer treatments could be invented by merging radiation therapy with nanotechnology. Several recent studies demonstrated that injecting gold nanoparticles directly into cancerous tissue during XRT augments therapeutic effects due to the nanoparticles' high photoelectric interaction cross section [22-25]. In 2010, Polf et al. demonstrated that injecting gold nanoparticles into tumor tissue also enhances external proton beam therapy [26]. Al though this gold nanoparticle injection technique is

promising for enhancing external beam therapies, these treatments remain localized to known tumor tissue, and still subject healthy tissue to ionizing radiation.

The fundamental objective of this research is to augment TRT effectiveness and reduce potential side effects by merging nanotechnology with TRT. Radioactive nanoparticles functionalized to target specific receptors of cancerous tissues via mAb conjugation will be studied for use in cancer therapy. By introducing radioactive nanoparticles as radioactive payload carriers, the TRT treatment should be enhanced because the number of radioactive atoms per tumor cell is increased as shown below in Figure 1.6. Furthermore, by separating the radionuclide from the mAb, it may be possible to improve TRT pharmacokinetics by avoiding radiolysis and decomposition of the antibody. In 2006, Katti et. al. demonstrated that radioactive gold nanoparticles can be coated to yield greater than 80% uptake in mice liver cells with minimal accumulation in blood and other non-target tissues, which supports this hypothesis [27].

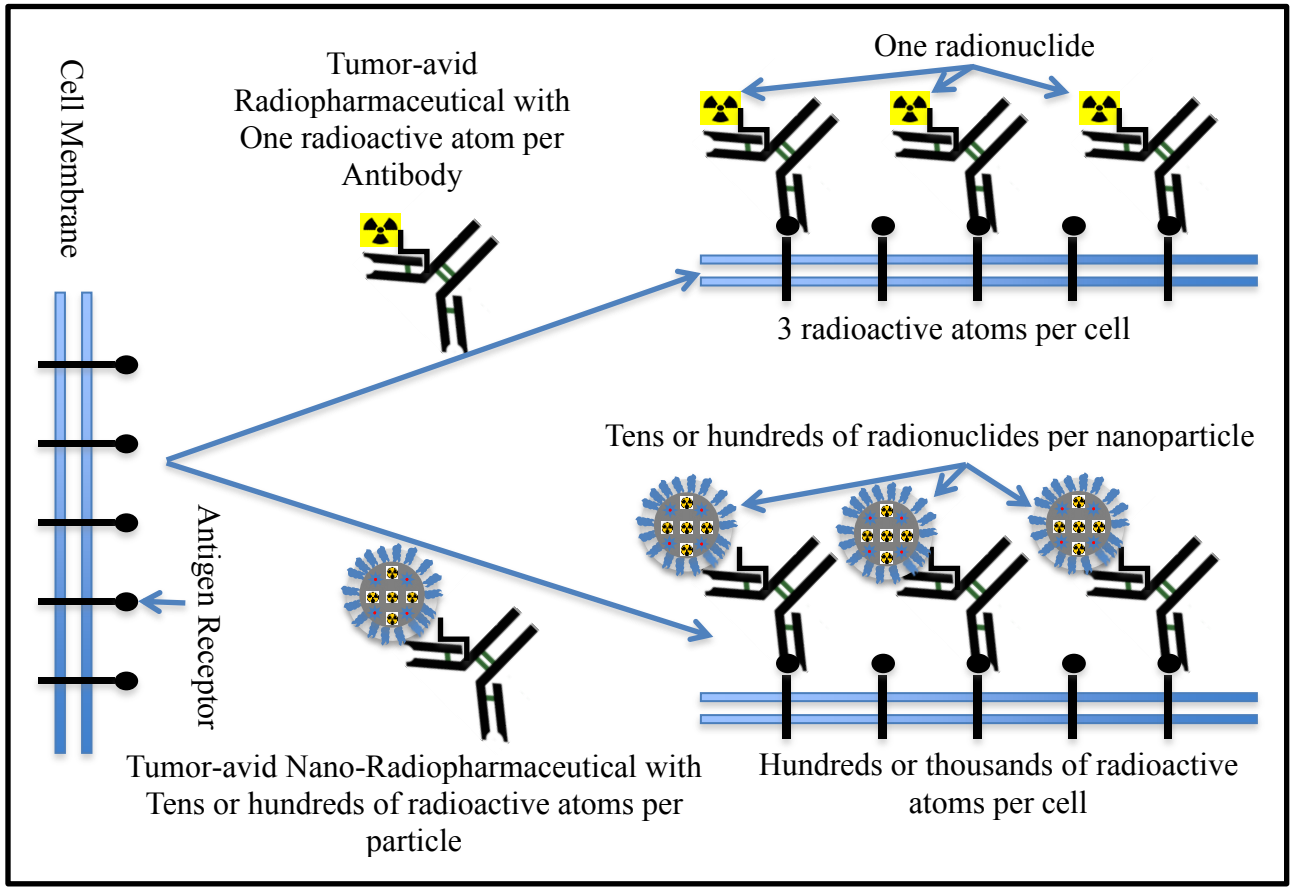

Fig. 1.6: Illustration of TRT (top) vs. Nano-Improved TRT (bottom)

The radionuclide used in the present research is ^{198}Au. Nanoparticles containing ^{198}Au can be produced by a variety of ways [28]. For this research, we produced ^{198}AuNPs by neutron activation of natural gold nanoparticles in a nuclear reactor. Equation 1.1 below describes this process.

(Eq. 1.1)

$$^{197}Au + n \rightarrow {}^{198}Au^{*} \rightarrow {}^{198}Au + \gamma$$

The typical nuclear decay reaction of ^{198}Au is shown in Equation 1.2 (see Figure 1.7 below for the decay chain of ^{198}Au). ^{198}Au decays by β^- emission. This emission provides therapeutic effect by damaging cancerous tissue as it loses kinetic energy traveling through it. The nuclide has a half-life of approximately 2.69 days and a 100% chance per decay to emit a β^- particle; the average β^- energy is about 312.4 keV (recall that the antineutrino carries away an average of about 2/3 of the total energy).

(Eq. 1.2)

$$^{198}Au \rightarrow {}^{198}Hg^{*} + \beta^{-} + \bar{\nu}, \quad {}^{198}Hg^{*} \rightarrow {}^{198}Hg + \gamma$$

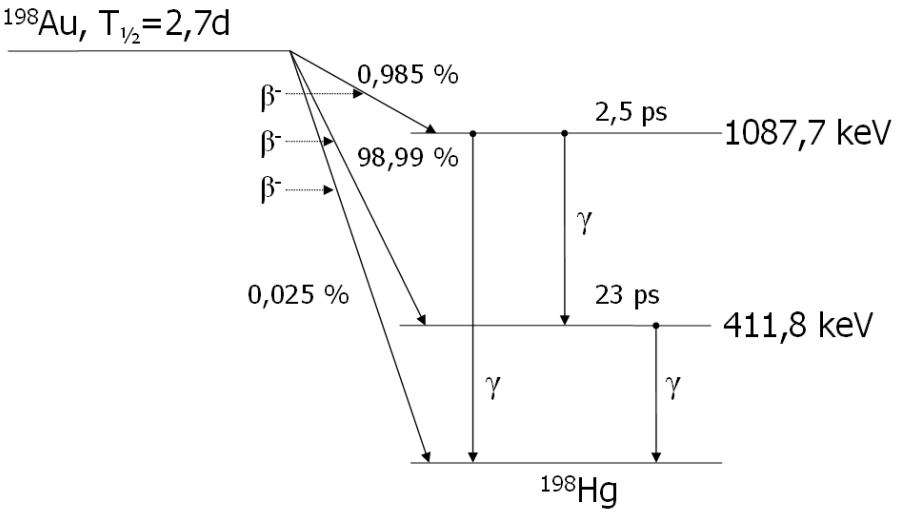

Fig. 1.7: ^{198}Au Decay Chain [29]

The beta emission spectrum of ^{198}Au is shown below in Figure 1.8. The range in typical human tissue of the mean energy ^{198}Au β^- emission is approximately 0.95 mm. This is a long enough path length to affect surrounding cancer cells which may under-express the cancerous target receptor (a phenomenon sometimes called "cross-fire"), while sparing most surrounding healthy tissue and nearby organs from direct radiation insult. 95.6% of ^{198}Au decays are accompanied by a γ decay of about 411.8 keV that is easily detectable using appropriate gamma detection equipment.

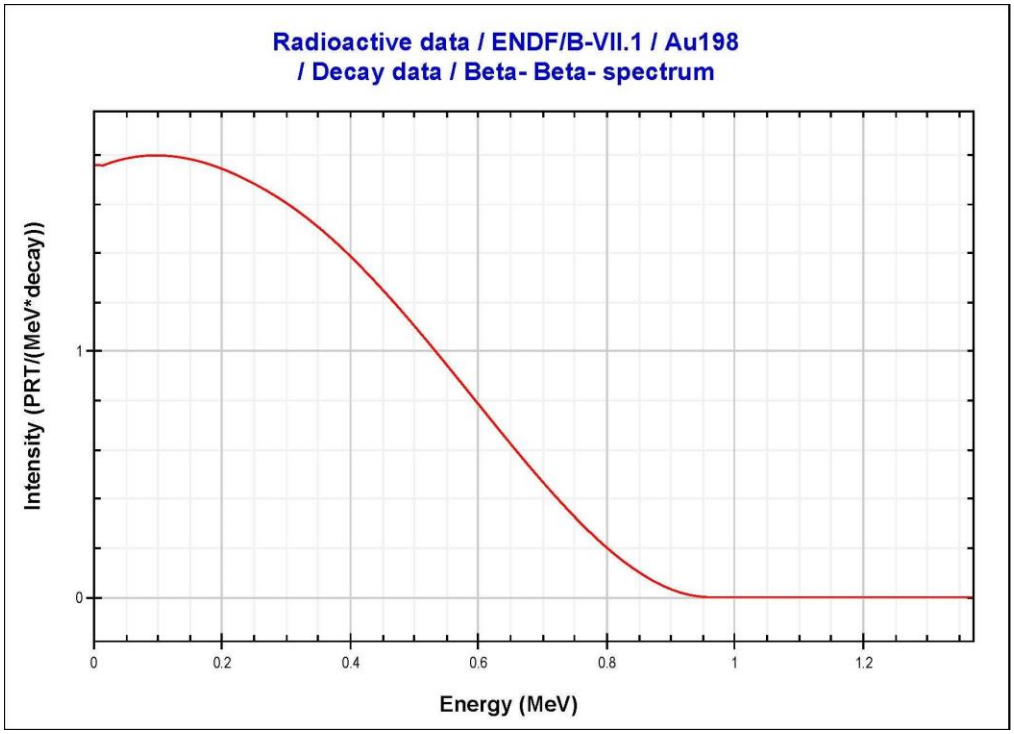

Fig. 1.8: ^{198}Au Beta Decay Spectrum [30]

Auger electrons can be released during ^{198}Au decay with an average energy of about 15.1 keV. Cancerous tissue can become radiosensitized by low-energy (tens of keV) electrons; thus these Auger electrons may further augment the effect of radiation therapy [31, 32]. This phenomenon is likely due to the high-LET nature of electrons in this lower energy regime [33]. However, only about 2.3% of ^{198}Au β^- emissions are accompanied by the emission of an Auger electron, and will therefore be ignored.

These gold nanoparticles (AuNPs) may also incorporate other therapeutic drugs as well. Radiation therapy is often more effective when used in combination with one or more alternate treatment methods [32, 34]. By merging TRT with nanotechnology, it

may be possible to incorporate cytotoxic drugs into the TRT-nanoparticle for simultaneous radiochemical treatments, further augmenting therapeutic effect.

1.4 Cancer Cell Line Investigated in This Study

Theoretically TRT can be applied to any type of cancer that overexpresses a known receptor for which a unique mAb may be synthesized. SK-BR-3 (ATCC; HTB-30™) adenocarcinoma breast cancer tissue was the cell line of interest for this study. This cell line overexpresses the human epidermal growth factor receptor type 2 (HER2). According to the International Agency for Research on Cancer (IARC), an agency which is part of the World Health Organization of the United Nations, nearly 39% of cancers found in women are breast cancers, of which 20-30% dramatically overexpress HER2 [1, 35, 36].

The HER2 receptor is one of four members of the epidermal growth factor receptor (EGFR) family (the others being HER1, HER3, and HER4). The EGFR family is present in normal tissue (though they are not found in the abundance found in many cancer types), and plays important roles in cell differentiation, migration, wound healing, and other functions essential to cell survival [37]. Cells which mutate and over-express EGFRs rapidly multiply and become more resistant to apoptosis, driving the development and survival of these cancers. HER1 is overexpressed in at least 50% of epithelial malignancies, and HER3 and HER4 are variably expressed in several types of cancers [38]. Subsequently, EGFR inhibitor research for the development of anticancer agents (including mAbs) has been active in the last twenty years [34].

1.5 Nano-Improved TRT: Final Product Design

Trastuzumab (also known by its brand name as Herceptin) from Genentech is a humanized mAb which binds to the extracellular juxtamembrane domain of HER2 [35]. In addition to providing a method of targeting HER2-overexpressed cancer tissue for selective nano-TRT treatment, Trastuzumab alone inhibits the survival and growth of these tumors through several possible processes including preventing the activation of intracellular tyrosine kinase, inhibiting extracellular domain shedding, immune activation, and ligand blocking [34, 35]. Herceptin was approved by the FDA in 1998, and has since been used to treat various HER2 cancers. Unfortunately this medical-grade product is quite expensive. Alternatively, PE anti-human CD340 monoclonal antibody from Biolegend also targets the HER2 receptor but costs a fraction of Herceptin's price. This mAb is also tagged with the fluorophore R-phycoerythrin (PE), which will be discussed further in Section 2.10. CD340 is a member of the EGFR family of cell membrane tyrosine kinases containing a single transmembrane domain and has a molecular weight of about 185 kD. The final design shown below in Figure 1.9 is a nanoparticle with multiple radioactive atoms, coated with a stabilizing surfactant (to prevent AuNP agglomeration) with mAbs attached.

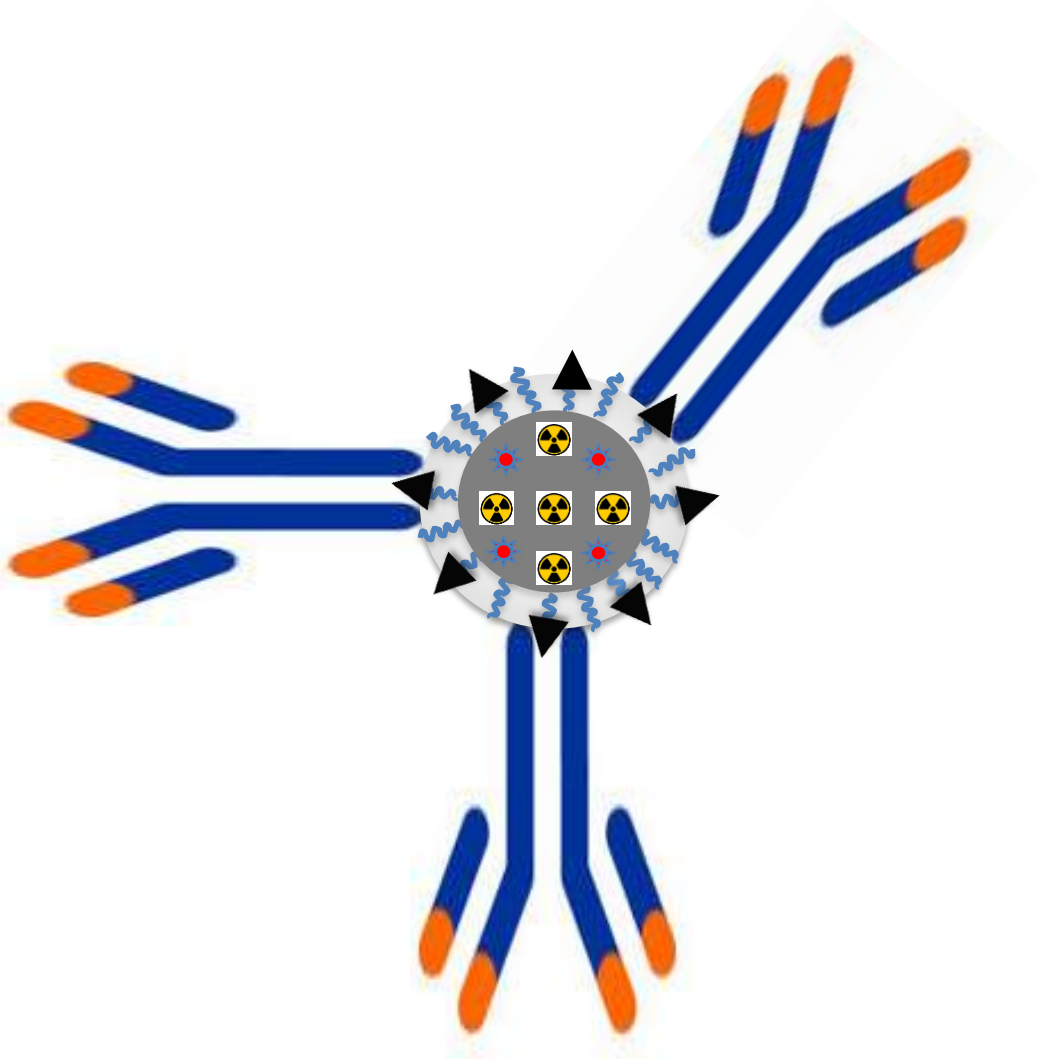

Fig. 1.9: Proposed Final Design, Complete with Radioactive AuNP Core and Attached mAbs

2. METHODS

2.1 Preliminary Nanoparticle Properties and Characterization

We initially investigated two sets of gold nanoparticles from different vendors in this research. One set had an average diameter of 17 nm, purchased from Nanopartz Inc., Salt Lake City, USA, while the other set had an average diameter of 10 nm from Cytodiagnostics Inc., Ontario, Canada. The Nanopartz nanoparticles contained a concentration of 1.33×10^{14} particles mL^{-1} with a Certificate of Analysis (CoA) containing TEM, UV-VIS, and dynamic light scattering (DLS) measurements and calculations shown below in Table 2.1 and Table 2.2. Figure 2.1 below shows a vendor-provided TEM image of these gold nanoparticles prior to shipment. The Nanopartz AuNPs were encased in a polymer with N-hydroxysuccinimide (NHS) ester terminal groups to protect the AuNPs from salt and variations in pH, as well as reduce non-specific binding and aggregation. The AuNPs were stored at 4 °C while not in use to maintain nanoparticle coating stability and prevent nanoparticle coagulation. Nanopartz guaranteed directional conjugation whereas Cytodiagnostics initially did not. The potential implications of this will be discussed later.

Table 2.1: CoA Measured AuNP Characteristics (Nanopartz)

	Measurement Method	Units	Measured Value
Avg. Diameter	DLS, TEM, UV-VIS	nm	17
PDI	DLS, TEM	StdDev/size	7%
SPR Abs. Peak	UV-VIS	nm	521
Zeta Potential	DLS	mV	-15

Table 2.2: CoA Calculated AuNP Characteristics (Nanopartz)

Characteristic	Units	Calculated Value
Concentration	NPs mL^{-1}	$1.33x10^{14}$
Wt. Concentration	mg mL^{-1}	6
ppm		6000
Wt. %	%	0.6000%
Molarity	μM	0.212133
Molar Ext.	M^{-1} cm^{-1}	$5.43x10^{8}$

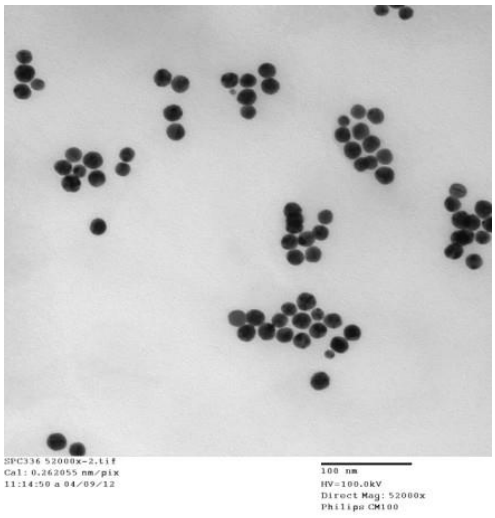

Fig. 2.1: TEM Image of 17 nm AuNPs Upon Arrival (Nanopartz)

The AuNPs from Cytodiagnostics (shown in TEM below in Figure 2.2) were supplied at a particle density of 5.98×10^{12} AuNPs mL^{-1}, and an SPR peak of 518 nm.

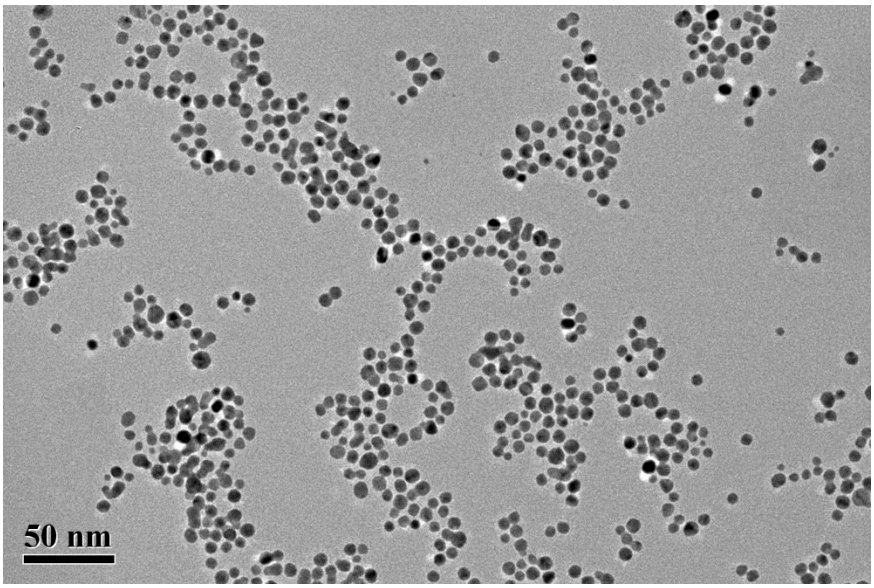

Fig. 2.2: TEM Image of 10 nm AuNPs upon Arrival (Cytodiagnostics)

2.2 Neutron Activation Preparation

All gold nanoparticles were purchased as natural gold (^{197}Au). The AuNPs were made radioactive through the nuclear reaction shown in Equation 1.1. We initially activated gold nanoparticles at the TAMU Nuclear Science Center (NSC). Sample temperatures could reach as high as 80 °C, which is significantly lower than the temperatures required to cause thermal-induced gold structural changes such as thermal annealing [39]. We transferred samples of the nanoparticle solution into a quartz vial in preparation for neutron activation. Quartz has excellent neutronic properties that allow

thermal neutrons to reach the gold nanoparticles without damaging the vial during irradiation, and has already been established as an effective vessel for activating gold nanoparticles in previous research efforts [40]. Quartz vials were sealed at the TAMU Department of Chemistry Glass Shop by freezing the quartz in liquid nitrogen and rapidly melting the tip shut with a blow torch. The sealed vials are sealed in an aluminum can filled with aluminum foil during irradiation to protect the vial from damage during movement to and from the reactor core while still allowing neutrons to reach the nanoparticles within. The prepared vial is shown below in Fig. 2.3.

Fig. 2.3: AuNP Neutron Activation Vial Assembly

After neutron activation, the quartz vials must be opened to extract the nanoparticles. Initially we opened the quartz vial using a diamond-coated saw. This

method resulted in contaminating the sample inside due to quartz dust from sawing through the vial. Instead, we subsequently used a blow torch to melt a hole in the lid of the quartz.

2.3 Neutron Activation Analysis

Neutron Activation Analysis (NAA) equations can be used to calculate the activity of a sample material which has been exposed to a neutron field for a given time. The fundamental equations for NAA, shown below in Equations 2.1 and 2.2, are valid assuming the neutron flux does not change throughout the activation, negligible burnup of daughter atoms, and negligible decrease of target atoms.

(Eq. 2.1)

$$A_B(t_{irr}, t_d) = A_0\left(1 - e^{-\lambda_B t_{irr}}\right)e^{-\lambda_B t_d}$$

(Eq. 2.2)

$$A_0 = N_A\left(\sigma_{2200}\phi_{2200} + I_\infty\phi_{epi}\right)$$

Although the total activity of the activated sample is a concern for dose to personnel handling the nanoparticles, the primary concern for therapeutic effect is not the total sample activity injected, but rather the number of radioactive atoms per nanoparticle. This is discussed later in the section.

To conduct high resolution gamma spectroscopy, we used a Model BE2020 Canberra High Purity Germanium Detector (HPGe) provided by TAMU Nuclear Engineering Professor Dr. Craig Marianno. The total activity of the samples was on the order of several hundreds of μCi. Such a high activity source could yield significant detector dead time. To avoid this, the detector and source were placed 2.8 meters apart (± 1 mm), significantly reducing the solid angle of emissions from the source to the detector.

To ensure that the Genie2000 software associated with the HPGe was applying geometry calculations properly, we used a calibration method involving a known gold source. Since ^{198}Au only has a half-life of 2.69 days, we had to produce this known radioactive gold source for every nanoparticle activation trial. We purchased NIST-certified FLUKA Gold Standard Solution from Sigma-Aldrich for which the gold concentration was known. For each activation experiment, the nanoparticle vial was accompanied by a second vial of the Gold Standard solution, both of which had the same geometry and was activated simultaneously. Given known reactor conditions, the gold standard activity can be calculated using NAA equations, which provided us with a reasonably accurate calibration standard to measure the nanoparticle sample activity.

2.4 Radioactive Nanoparticle Structural Integrity

Neutron activation can degrade structural integrity of the nanoparticles and their coatings; to monitor integrity we used transmission electron microscopy (TEM). TEM is ideal for imaging AuNPs because of the metal's high density and ability to scatter

electrons. For this experiment, we used the JEOL JEM-2010 TEM at the TAMU Microscopy & Imaging Center. Using the images from this analysis, we could quantitatively characterize the size of nanoparticles, including mean diameter, standard deviation, maximum and minimum sizes, etc. The open-source program, ImageJ, developed by the National Institutes of Health (NIH), is well suited for this analysis. Note that AuNP-mAb conjugation must occur after neutron activation, as the antibodies and/or bindings will likely not survive the radiation fields they would experience during the activation process.

2.5 Nuclear Probability Theory: Radioactive Nuclei per Nanoparticle

Each nanoparticle must contain at least one radioactive atom to yield any potential radiotherapeutic effect, therefore the distribution of radioactive atoms among the nanoparticles in the sample should be known. The total sample activity and the number of radioactive atoms per nanoparticle are dependent on irradiation and decay time, as well as the neutron flux in the reactor. Even using the same activation conditions, however, the number of radioactive atoms per nanoparticle is a function of the size of the nanoparticle, because larger nanoparticles contain more ^{197}Au nuclei and therefore more potential activations.

The statistical Poisson Distribution applies when: (1) the event of interest (i.e. a ^{197}Au nucleus absorbs a neutron) can be counted in discrete whole numbers, (2) occurrences are independent such that one occurrence does not diminish nor increase the probability of another, (3) the average frequency of the occurrence is known, and (4) it is

possible to count how many events have occurred. Since the total decrease of ^{197}Au nuclei from the population due to neutron absorption during activation is negligible, it is reasonable to approximate the above four parameters are met. The number of ^{198}Au nuclei per nanoparticle can therefore be calculated using the Poisson Distribution, shown below in Equation 2.3. Assuming a 12 hour irradiation and 6 hours of decay in the NSC nuclear reactor for both trials, the following "^{198}Au nuclei per nanoparticle" distributions in Figure 2.4 show a clear comparison when using 10 nm vs. 17 nm diameter nanoparticles.

(Eq. 2.3)

$$P(k;\lambda) = \frac{\lambda^k e^{-\lambda}}{k!}$$

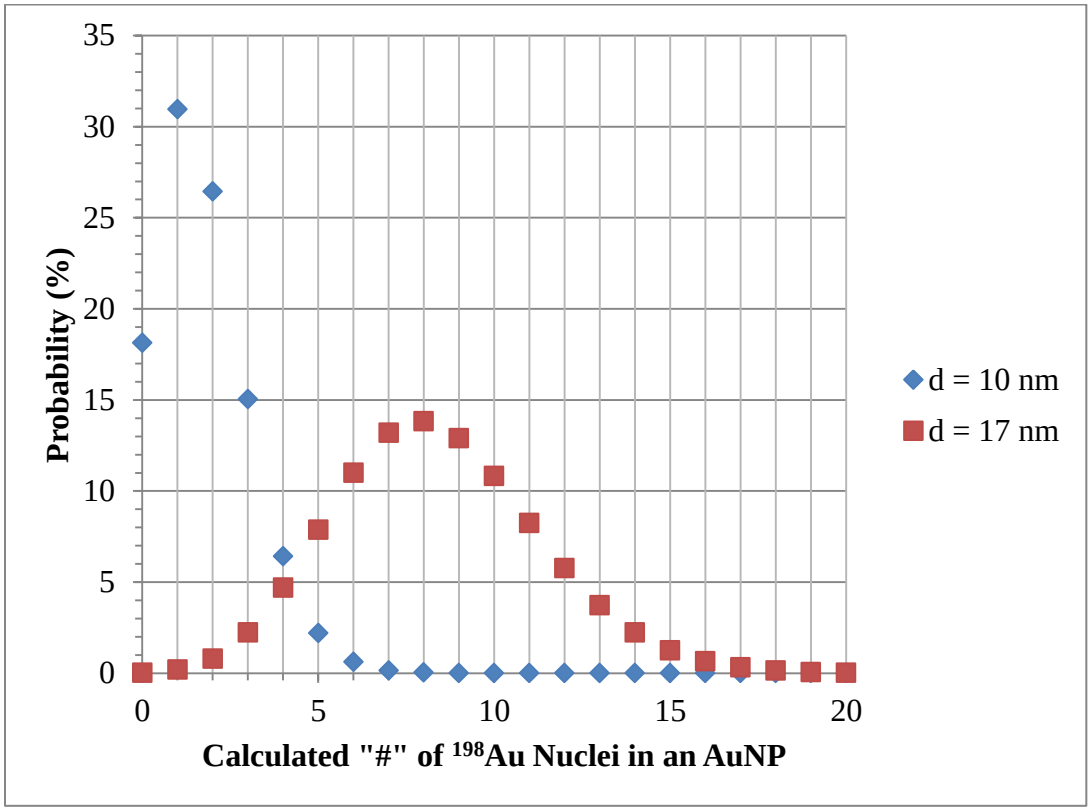

Fig. 2.4: Poisson Distribution of Calculated ^{198}Au Nuclei per AuNP Given t_{irr} = 12 h (in TAMU NSC Reactor) and t_d = 6 h, 10 nm vs. 17 nm

Under the given activation conditions, nearly 18% of the 10 nm nanoparticles contain no radioactive nuclei; thus, nearly 18% of these nanoparticles yield no TRT effect. Almost all of the 17 nm AuNPs, however, contain at least one ^{198}Au nucleus. Under these irradiation conditions, the 10-nm sample has an average of about 1 radioactive nucleus per nanoparticle, whereas the 17-nm sample has an average of about 8 radioactive nuclei per nanoparticle.

2.6 Nanoparticle-Antibody Directional Conjugation

Two major concerns when conjugating nanoparticles with antibodies are the weak non-covalent antibody attachment to nanoparticles and the potentially random orientation of bound antibodies to the gold nanoparticle surface due to their electrostatic interactions [41]. A weak antibody-ligand bond may lead to antibody replacement by other molecules, while randomly oriented antibodies bound to ligands may significantly reduce the likelihood of antibody-cell interaction. Nanopartz Inc. coats nanoparticles with a proprietary ligand which covalently bonds specifically with the fragment crystallizable (Fc) region of the antibody. This directional conjugation is critical, as the fragment antigen-binding (Fab) region of the mAb is responsible for interacting with the cancer cells' receptors, and small (~10 nm) AuNPs will likely have only a few antibodies attached per nanoparticle. This can be visualized from Figures 2.5 and 2.6 below.

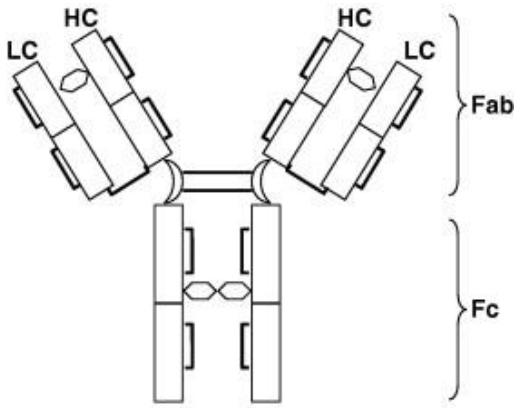

Fig. 2.5: Antibody Schematic with (Top) the Fab Region, and (Bottom) the Fc Region [42]

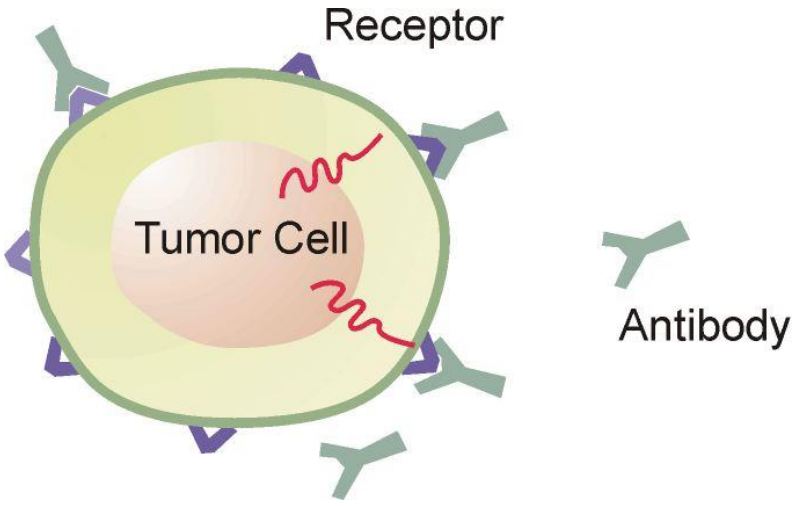

Fig. 2.6: Antibody-Cell Attachment Schematic with Fab-Receptor Interaction

The procedure to directionally conjugate the Nanopartz nanoparticles is as follows. Non-potassium containing phosphate buffered saline (PBS) from Thermo Pierce (# 28372) was used as a conjugation buffer. Gold nanoparticles were added to the CD340 in PBS with a mAb:AuNP molar ratio of approximately 500:1 and placed in a vortex machine for 1 to increase the rate at which mAbs interact with AuNPs, thereby increasing the rate of conjugation. The mAb:AuNP ratio is sufficiently large such that nearly all AuNPs have attached mAbs, bypassing the need to separate the conjugated and unconjugated AuNPs. The supernatant was then removed by centrifuging for 30 minutes at 12,000 relative centrifugal force (RCF). Conjugated AuNPs are stored in pure water at 4 °C.

Throughout this thesis AuNPs from Cytodiagnostics are referred to as “bare” since they are not coated with materials which drive directional mAb conjugation. In reality, the AuNPs from Cytodiagnostics are coated with the stabilizing surfactant

trisodium citrate ($Na_3C_6H_5O_7$). This surfactant reduces the degree of AuNP agglomeration and does not drive conjugation.

2.7 Conjugated Nanoparticle Characterization

There are several methods to determine the direction and density of mAb attachment to the AuNPs. A FRET technique, discussed in Chapter 1.2, was initially conceived, which could be collected using flow cytometry. We realized that additional data would be available through agarose gel electrophoresis from the suggestion of Dr. Mahmoud El Sabahy, Co-Assistant Director of the TAMU Laboratory for Synthetic-Biological Interactions. With proper control groups, gel electrophoresis can provide strong evidence of mAb conjugation due to the distinct migration of particles based on charge and size [43, 44]. We conducted electrophoresis using BIO-RAD gel electrophoresis equipment with a 100 V driving potential for 1 hour. The agarose gel was prepared by heating 400 mL of pure water [with 6 mL of triethanolamine (TAE) 50x buffer (pH of 8.3)] to boiling. Once boiling, 3 g of agarose powder was added and boiling continued until the powder was dissolved. The mixture was heated with stirring until the final volume was 300 mL, and then allowed to cool until warm to the touch. The solution was poured into the mold and allowed to set for approximately 45 minutes. The gel was then transferred to the BIO-RAD electrophoresis template and filled with the buffer solution, prepared by adding 20 mL of TAE buffer to 980 mL of triple-distilled water.

Besides electrophoresis, dynamic light scattering (DLS) measurements can provide evidence of mAb attachment [45-47]. Nanoparticles suspended in solution experience Brownian motion, which causes fluctuations in light scattering intensity during laser stimulation. These fluctuations can provide information such as particle size distribution, polydispersity, and zeta potential of the sample [48]. These values should change if conjugation is successful. The DLS instrument used, provided by TAMU Professor Dr. Karen Wooley, was the Delsa Nano C Particle Analyzer from Beckman Coulter.

While the above techniques yield macroscopic information representing a population of AuNPs, individual AuNP characterization is also necessary [49]. TEM is ineffective for imaging mAb-conjugated AuNPs for several reasons. The kinetics associated with the high energy/intensity electron beam may dissociate the attachment between the nanoparticle and the antibodies. The high vacuum conditions inside the TEM may also destroy these bonds. Most important, however, proteins generally scatter energetic electrons with very low efficiency. While the metal nanoparticles can be seen clearly in TEM, the signal from any proteins will be indistinguishably faint. However, atomic force microscopy (AFM) is a viable alternative. AFM generally has resolution on the order of fractions of a nanometer, and is capable of generating 3-dimensional images of nanomaterials (a capability which TEM generally cannot do). The instrument operates by scanning the surface of a specimen with a sharp-tipped probe connected to a cantilever (shown below in Figure 2.7). As the tip passes over a different material (for example, going from substrate to a nanoparticle), the tip is deflected vertically. This

deflection is measured by reflecting a laser beam from the top surface of the cantilever into a photodiode array (see Figure 2.8). It may be possible to confirm mAb-AuNP attachment by using AFM to image the nanoparticles before and after mAb conjugation. We collected images using the Bruker Multimode-8 Atomic Force Microscope under the supervision of the TAMU Laboratory for Synthetic-Biological Interactions Co-Assistant Director Dr. Jeffrey Raymond.

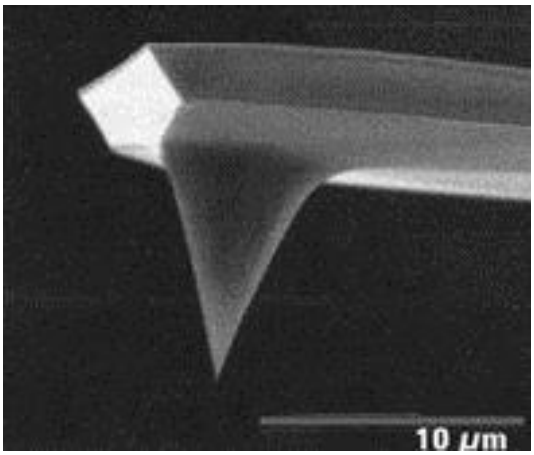

Fig. 2.7: AFM Cantilever and Pointed Tip [50]

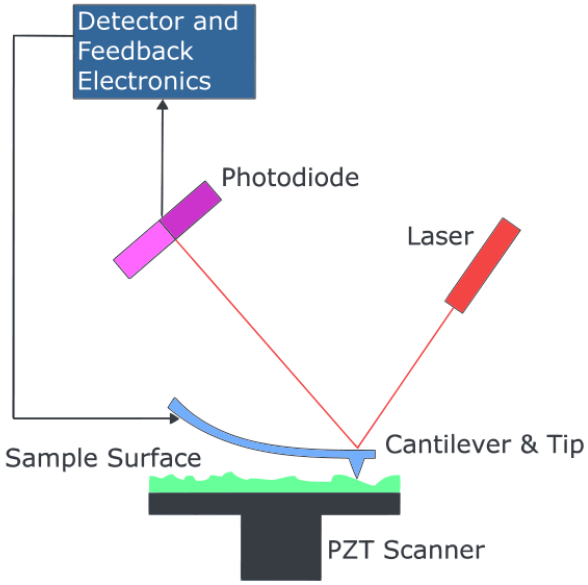

Fig. 2.8: Diagram of AFM Components [51]

2.8 Radioactive Nanoparticle Dosimetry

TRT dosimetry is complex in comparison to XRT due to the pharmacokinetics associated with the radionuclide agents. Assuming that all nanoparticles are conjugated with targeting agents (in this case CD340), there is no guarantee that 100% of conjugated AuNPs will encounter and bind to cancerous tissue; in fact recent studies have shown that the binding efficiency of Trastuzumab-conjugated AuNPs can be as low as 65% for large (>200 nm) nanoparticles [52]. By using smaller 150 nm nanoparticles, however, a recent study suggests that the presence of the nanoparticles may actually increase the likelihood of mAb-cell interaction by up to 25% [53]. If the conjugated AuNPs do encounter and interact with the cells, the nanoparticles will eventually be released from the cells (hence a biological half-life). The whole-body biological half-

life of Trastuzumab, however, has been shown to vary from 3-4 weeks, which is equivalent to 8-11 physical ^{198}Au half-lives [54].

The following calculation assumes an infinite AuNP residence time within the target cell. Assuming the same 12 hour neutron activation and 6 hour decay of nanoparticles, the 17 nm AuNPs will have an average of 8 radioactive nuclei per nanoparticle. Given that the primary β^- emission from ^{198}Au yields 311 keV Bq^{-1} s^{-1} and assuming an infinite nanoparticle residence time within the cancerous tissue, a correlation between 17 nm AuNPs per cell vs. dose from the primary β^- emission may be calculated directly, shown below in Figure 2.9. This dose calculation approximates an infinite medium of cancer cells with a homogeneous distribution of radioactive nanoparticles such that, on average, as a β exits a cell, an identical one enters it. This allows a quick estimation of dose by allowing us to assume that, effectively, all the β energy is deposited into a cell. While studies show that hematopoietic malignancies such as NHL only require TRT doses as low as 15 Gy to observe significant therapeutic effects, solid tumors may require doses higher than 60 Gy [55].

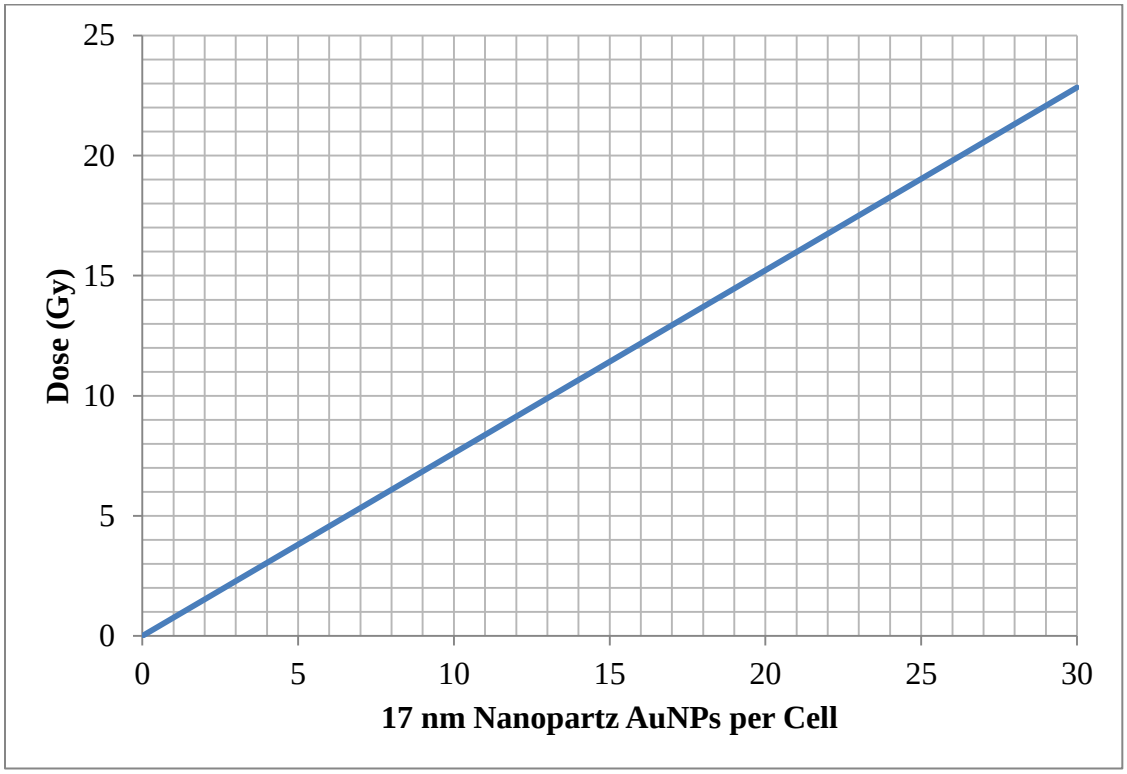

Fig. 2.9: Calculated Dose (Gy) from Primary β^- Emission vs. 17 nm AuNPs per Cell, Assuming Infinite AuNP Residence Time Approximation

2.9 Cell Culture

Methods for the culture and maintenance of the SK-BR-3 cell line are available online via ATCC. Imaged below in Figure 2.10 is cultured SK-BR-3 adenocarcinoma (before treatment).

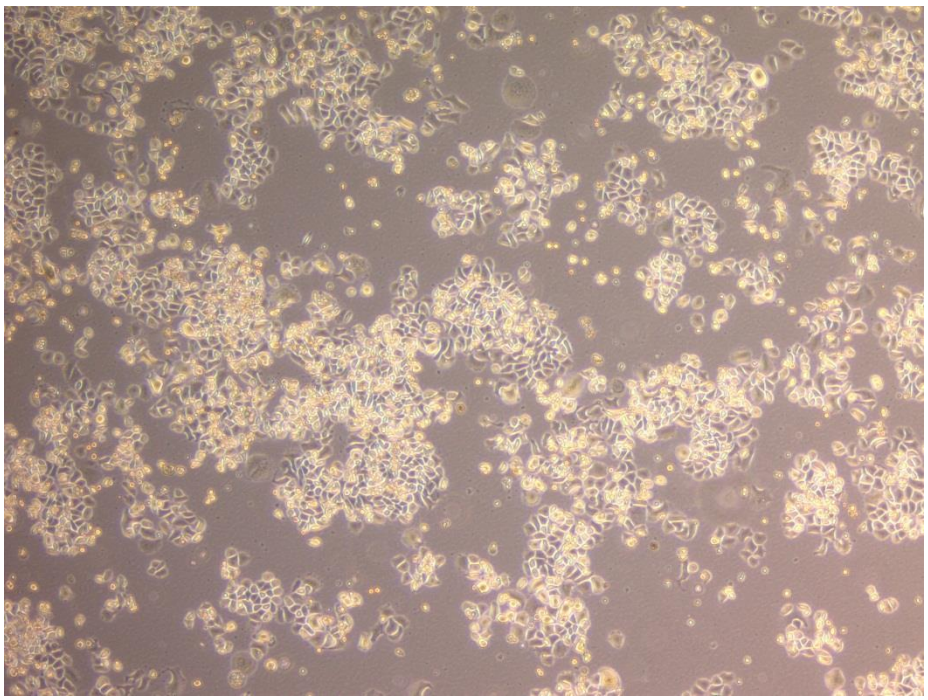

Fig. 2.10: Microscope Image of Cultured SK-BR-3 Adenocarcinoma Cells

2.10 Flow Cytometry and Fluorescent Microscopic Analysis

The affinity with which conjugated nanoparticles bind to target cells is critical. Cell binding was assessed using the Accuri C6 Flow Cytometer, equipped with two excitation lasers that operate at wavelengths of 488 nm and 640 nm. To complement the quantitative flow cytometer measurements, we collected fluorescent images using the Invitrogen FLoid™ Cell Imaging Station from Life Technologies Corporation. Flow cytometry provides a means of measuring physical and chemical properties of individual cells simultaneously (or other particles, such as mAbs or AuNPs) in a fluid stream at speeds on the order of tens of thousands of cells per second [56, 57]. For an illustration of how flow cytometry works, see Figure 2.11 below. The instrument funnels particles

into a single-file stream. The focused particles pass through and interact with laser beams. Cells which express receptors unique to that cell type, such as HER2 for the case of SK-BR-3, may be bound with a mAb. By using mAbs which are tagged with a fluorochrome, flow cytometry provides an effective means of determining whether the conjugated nanoparticles are attached to the cells.

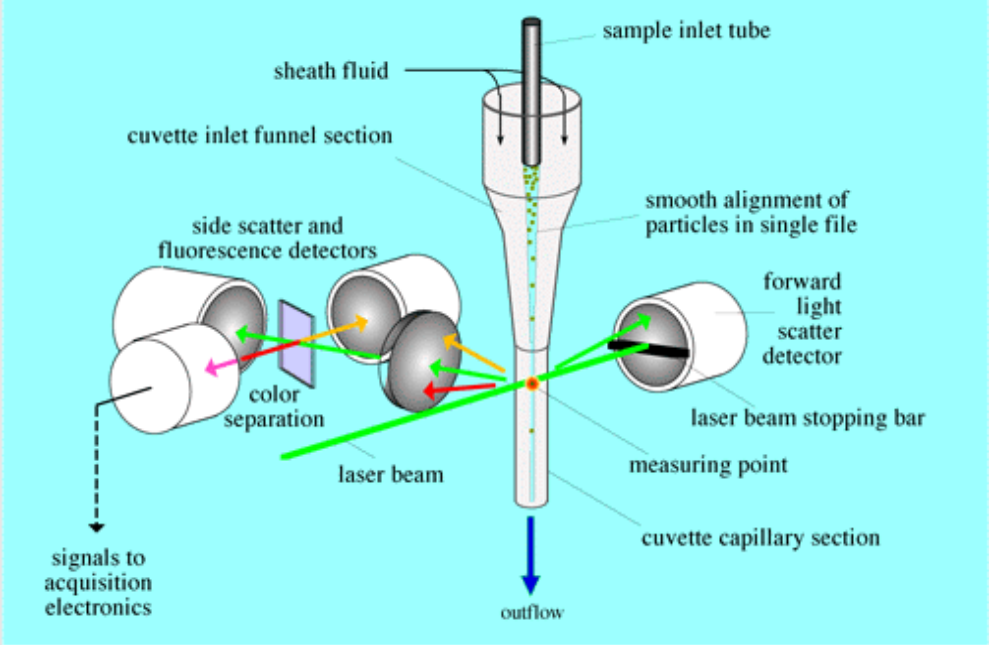

Fig. 2.11: Flow Cytometer Operating Principles

As cells pass through a laser beam, the mAbs fluoresce and scatter light in all directions. Light scattered in the forward direction (i.e. deflected by a small angle) can be used to determine the size of the particle. Scattering events at 90° to the incident laser beam can be used to determine cell cytosolic structure (e.g. inclusions or granules)

[58]. Fluorescence indicates the presence of a cell with fluorochrome-tagged antibodies. Cells that are bound with fluorochrome-containing antibodies can then be imaged with the fluorescent microscope. This combination of instruments provides both quantitative and qualitative analysis of the interactions between the cancer cells and the antibodies that selectively seek and bind to them. As mentioned in Section 1.5, the CD340 antibodies are tagged with PE. This fluorochrome's absorption and emission spectrum are below in Figure 2.12.

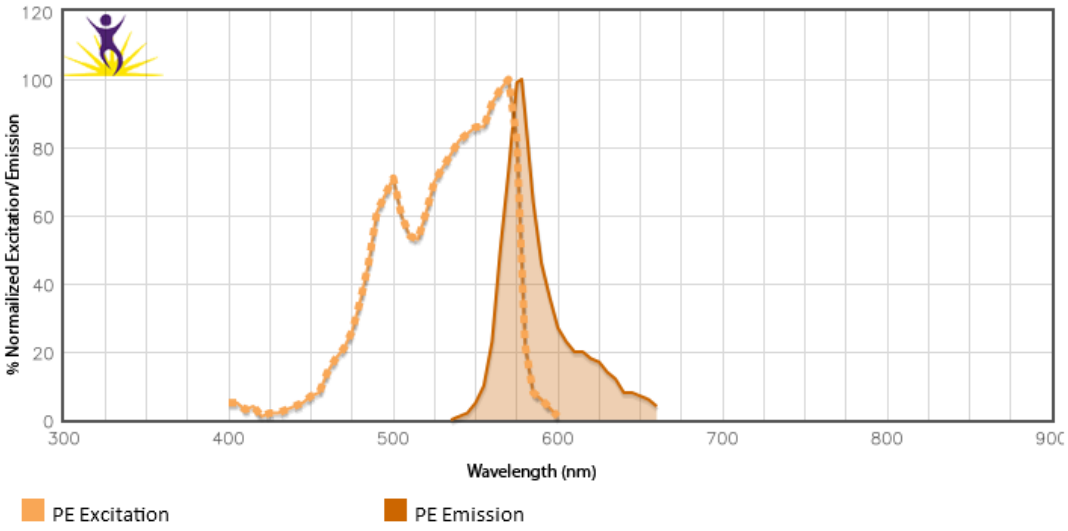

Fig. 2.12: PE Absorption and Emission Spectra [59]

2.11 Cell Characterization and Growth Response Analysis

Clonogenic Assays are typically used to determine radiation-induced cellular response. However, there are two significant disadvantages associated with a clonogenic assay for the purposes of TRT-induced cellular response [60-63]. The first disadvantage

is one of impracticality; clonogenic assays are time consuming and require a large number of cells, antibodies, nanoparticles, etc. More important, a traditional clonogenic assay inherently cannot determine cell response as a function of time.

Alternative to clonogenic assays is the xCELLigence System from Roche Applied Science [64-66]. This system monitors cell population in real time without the use of labels or probes by measuring the electrical impedance across an electrode array at the bottom of the tissue culture plates. The dimensionless parameter "cell index" is derived as the relative change in impedance to represent cell status. This provides a method of measuring cell number, viability, and morphology as a function of time. In comparison to XRT, these real-time measurements are especially important for the purposes of TRT-induced cell response since the radiative emissions occur gradually over time rather than in one short burst.

The xCELLigence system operates while inside the incubator. Since it measures cell characteristics over time, this system can provide quantitative data of cell growth and cell death on multiple samples and controls simultaneously. A schematic of xCELLigence system functionality is shown below in Figure 2.13.

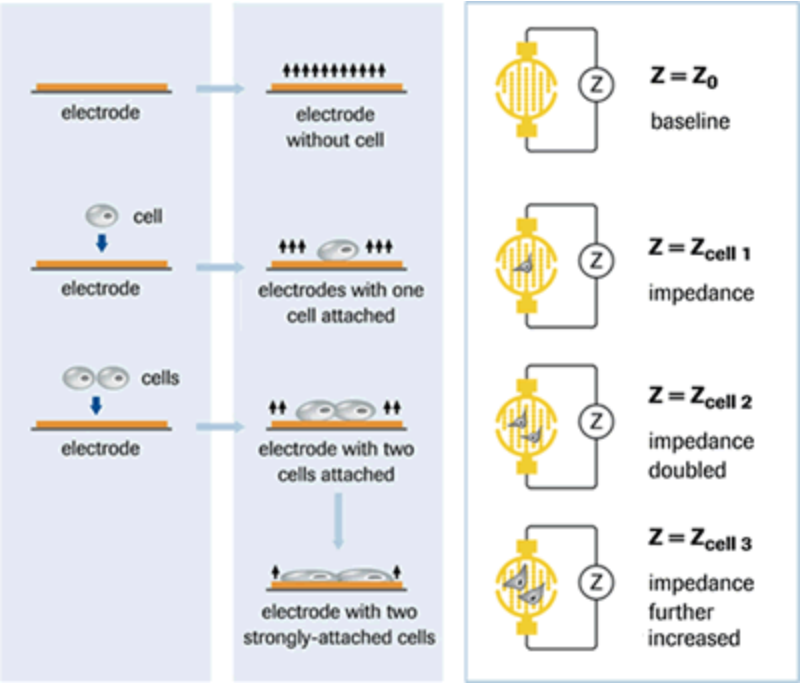

Fig. 2.13: Illustration of xCELLigence System Impedance Variability due to Cell Adhesion [67]

An additional advantage to using this system is freedom in experimental control groups as a function of time. For example, researchers have recently calculated the dose of radioactive nanoparticles to solid tumors with computational simulations that may predict biological effects [68-70]. However, simulations do not account for phenomena which influence radiation-induced biological effects, such as metal nanoparticle cytotoxicity. As previously discussed, cancer therapy regimens often incorporate multiple kinds of treatments which can augment one another's effectiveness [32, 34]. These effects need to be assessed together to determine full treatment efficacy.

3. RESULTS AND DISCUSSION

3.1 Small (10 nm & 17 nm Diameter) AuNP Failures

To determine surfactant longevity nanoparticles from both vendors were intentionally aged (at 4 °C) past their shelf life and tested until they failed. Since Nanopartz guaranteed directional conjugation and Cytodiagnostics initially did not, these different coatings could have yielded different product shelf lives.

The AuNP trisodium citrate stabilizer from Cytodiagnostics (see original TEM image Figure 2.2) consistently failed during 8- and 6-hour neutron activations in the NSC nuclear reactor; however non-activated samples from this batch were normal to the naked eye 9 months later. In Fig. 3.1, the nanoparticles after neutron irradiation (middle) have clearly agglomerated into a closely packed group, leaving the water clear instead of the red hue before neutron activation (left). The proprietary stabilizer from Nanopartz (see original TEM image Figure 2.1) failed without neutron activation after 5 weeks of 4 °C storage. The Nanopartz AuNPs adhered to the walls of the vial as shown below in Figure 3.1 (right).

Fig. 3.1: 10 nm Cytodiagnostics AuNPs Before (left) and after (middle) Activation, and 5 Week Old Non-Activated 17 nm Nanopartz AuNPs (right) Adhering to Vial

After discussing the passive AuNP agglomeration with Nanopartz, the vendor sent an additional sample of nanoparticles suspended in phosphate buffered saline (PBS). The AuNPs did not appear to coat the walls of the container as before. Using the same preparation and sealing procedures discussed earlier, we activated a sample of the new Nanopartz 17nm AuNPs for 6 hours in the TAMU NSC reactor, and this surfactant also failed.

After the 6 hour activation and subsequent 47.5 hours of decaying in the NSC reactor pool, the sample had clearly agglomerated to the naked eye and appeared similar to that of Figure 3.1 (middle). Had the nanoparticles survived, however, the distribution of ^{198}Au nuclei per AuNP would be similar to that shown below in Figure 3.2. Activating 17 nm AuNPs for 6 hours in the NSC nuclear reactor will not produce the

goal of at least one radioactive atom per nanoparticle, even if the nanoparticles had not agglomerated. Failure mechanisms and solutions to this issue are discussed in the next sections.

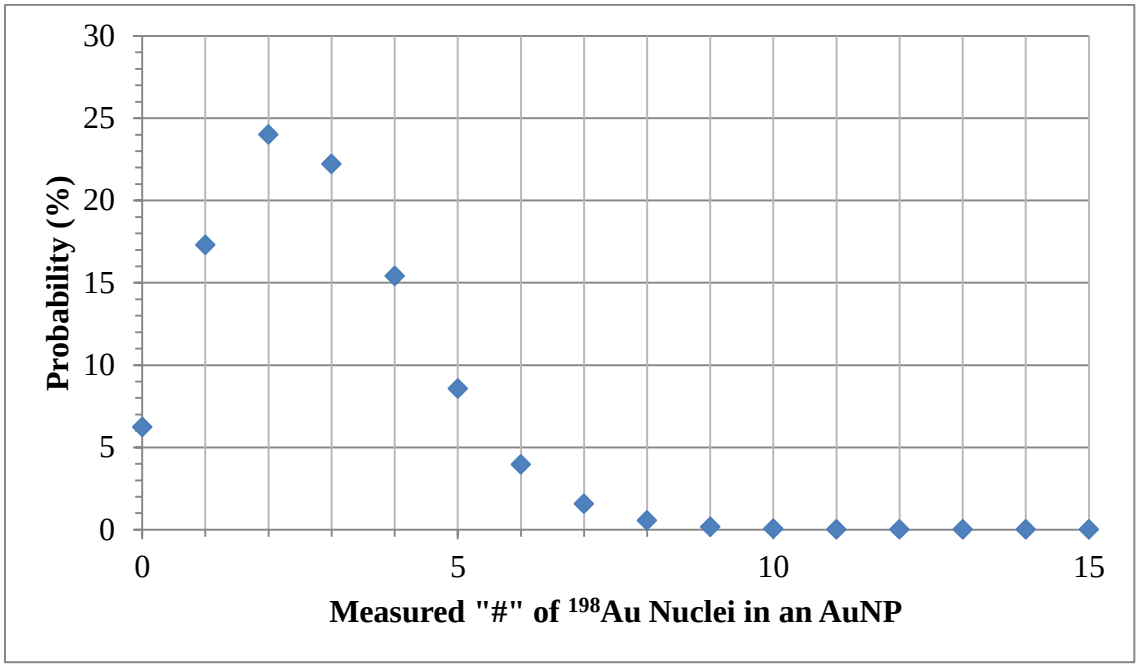

Fig. 3.2: Measured ^{198}Au Nuclei per 17 nm Nanopartz AuNP (Had the AuNPs Survived)

Even though the non-activated nanoparticles in solution from Nanopartz appeared to be stable to the naked eye, the first sample (which passively failed far before the expiration date) combined with the failure of the recent activated sample invoked our curiosity as to how effective the current surfactant was. We used AFM to attain 3D images and data for the new Nanopartz sample, both unconjugated (Figure 3.3) and

conjugated with the PE CD-340 antibodies (Figure 3.4). Several AFM images collected for this analysis are shown below.

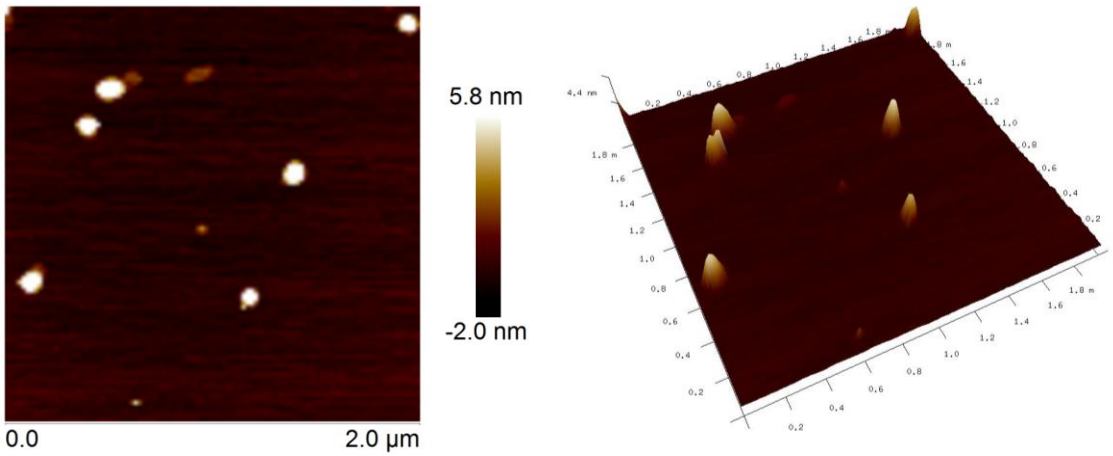

Fig. 3.3: 2D (Left) and 3D (Right) Images of Unconjugated 17 nm Nanopartz AuNPs

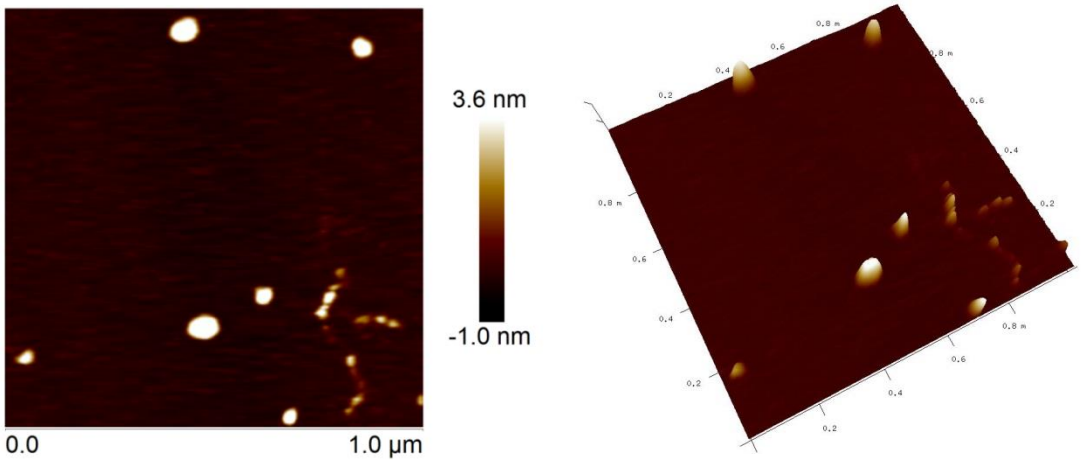

Fig. 3.4: 2D (Left) and 3D (Right) Images of mAb-Conjugated 17 nm Nanopartz AuNPs

The collection of images from this experiment yields two critical results. First, the new sample of 17 nm AuNPs provided by Nanopartz was almost exclusively comprised of larger (>60 nm in all three dimensions) aggregates. Since these nanoparticles had not yet been activated, had been stored in the proper 4 °C environment, and still had several months left on the predicted shelf life of three months provided by the manufacturer, we concluded that the surfactant used by Nanopartz is not effective in preventing nanoparticle agglomeration. AFM spectral analysis revealed that the few unconjugated AuNPs were consistently 16-19 nm, whereas the conjugated AuNPs were consistently 22-25 nm. These images provide strong evidence that our procedures to conjugate the nanoparticles were indeed successful.

After AFM, we looked at these AuNP samples using DLS. The resulting hydrodynamic diameters by number of the bare and conjugated AuNPs were of little use due to severe AuNP agglomeration (40 ± 10 nm for bare, and 41 ± 10 nm for conjugated). The zeta potential, which is simply the electrokinetic potential of colloidal systems used to determine coagulation potential, was -19 ± 2 mV for the bare sample and -28 ± 1 mV for the conjugated sample. This further suggests that, although the Nanopartz AuNPs were aggregating, our attempts to conjugate remaining single AuNPs were successful.

The three primary methods to mitigate AuNP agglomeration during neutron activation are to reduce the amount of time the nanoparticles are subjected to the high temperature of the nuclear reactor, reduce the nanoparticle surface energy, and reduce

the gamma ray dose rate during activation. These methods will be discussed in the following two sections.

3.2 AuNP Agglomeration and Failure Mechanisms

As discussed, the Cytodiagnostics "bare AuNPs" are coated with the stabilizing surfactant trisodium citrate. There are several mechanisms that may cause this surfactant to fail, thereby allowing nanoparticle aggregation to occur. The AuNPs are activated while inside a sealed quartz vial (see Figure 2.3). Recall that this vial is closed using liquid nitrogen and a high temperature flame. If the vial is cooled too long with liquid nitrogen during sealing, the contents of the vial will freeze, bringing the AuNPs closer together and potentially compromising the stabilizing surfactant. This failure mechanism did not occur during any of our tests. Similarly, if the AuNPs are exposed to sufficiently high temperatures (for example those found in some nuclear reactors), the trisodium citrate surfactant will also fail. The amount of time required to cause surfactant failure depends on temperature. We tested the Cytodiagnostics surfactant in a 90 °C water bath for 48 hours and observed negligible agglomeration, indicating that the high temperature environment of the NSC reactor did not drive agglomeration.

Radiation produced from the nuclear reactor core (primarily neutron and γ at the sample location) contribute to surfactant failure. Any nucleus is capable of absorbing neutrons; however the nuclei which compose the trisodium citrate surfactant ($Na_3C_6H_5O_7$) all have extremely low probabilities to do so, shown below in Table 3.1 in comparison with natural gold. Other neutron interactions with these nuclei dominate,

especially elastic scattering. The thermal neutron elastic scattering cross section for ^{1}H is approximately 20.5 barns; since the ^{1}H nucleus has similar mass to a neutron, conservation of momentum requires that a "head-on" (0° neutron deflection angle) elastic neutron scattering transfers nearly all of its kinetic energy to the nucleus, which may be enough to remove the nucleus from the molecule. Similar phenomena can occur with the other nuclei can occur, however, the scattering cross sections are smaller. Fissions occurring inside the reactor core also release γ radiation which can destroy the surfactant; however, γ exposure originating from outside the sample can be attenuated and reduced by surrounding the sample with a lead shield (which is more transparent to neutrons than γ's).

The ^{197}Au nucleus releases a prompt γ upon neutron absorption, after which the resulting ^{198}Au nucleus can release a β and γ during radioactive decay. Surfactant exposure from these radiations is unavoidable.

Table 3.1: Neutron Interaction Cross Sections for AuNP Surfactant Nuclei vs. Natural Gold and Natural Aluminum

Nuclide	Thermal σ(n,γ) (barns)	I_∞ σ(n,γ) (barns)	Thermal σ_s (barns)	Fis. Spectrum Avg. σ_s (barns)
^{23}Na	0.53	0.311	3.024	3.142
^{12}C	0.0035	0.0015	4.746	2.363
^{1}H	0.332	0.149	20.47	3.926
^{16}O	0.00019	0.000085	3.780	2.742
^{198}Au	98.65	1550		
^{27}Al	0.231	0.14		

3.3 Changing AuNP Size and Surface Energy

The surfaces of all materials have a certain degree of "surface energy". Surface energy can be defined as the work required removing a molecule from bulk to surface, or the degree to which the surface of a material is in an excited state in comparison to the bulk. Surface energy can be better understood using Figure 3.5 below.

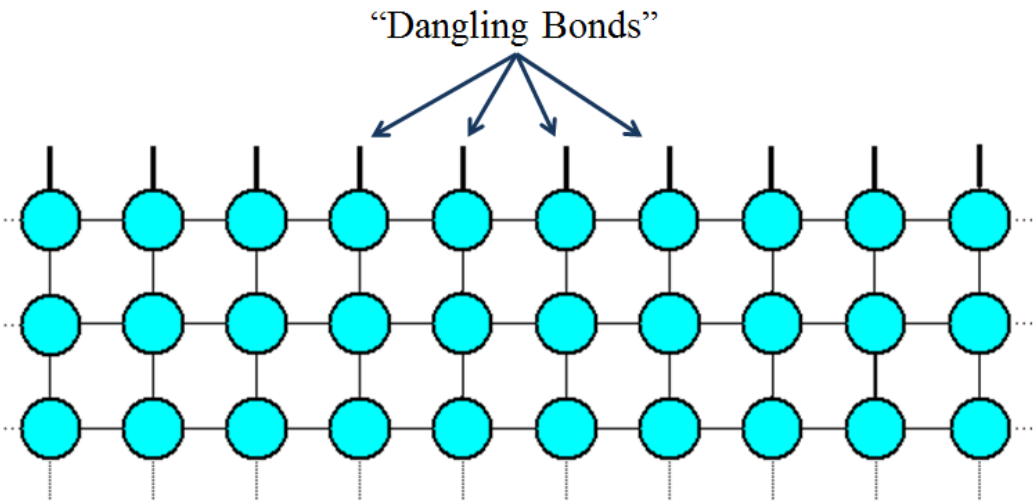

Fig. 3.5: The Surface of a Material with Dangling Bonds (Top) [71]

As shown in Figure 3.5, the surface of any material is not bound in all directions, resulting in "dangling bonds" (top). These dangling bonds reside in a high energy state. A form of surface restructuring can take place, which could produce lattice dislocations, voids, or other thermodynamically unfavorable phenomena [72]. In the macroscopic world we do not notice surface energy due to the extremely small fraction of object's atoms which lie on the surface. For materials in the nano-scale regime, however, surface energy is much more noticeable.

Assuming gold has a surface energy density of approximately 1 J m^{-2}, the surface energy of gold nanoparticles based on size can easily be calculated [73]. Table 3.2 below illustrates the size-dependent surface energy for three 1 g samples of gold spheres with arbitrary radii of (a) 1 mm, (b) 50 nm, and (c) 8 nm. Note that if the AuNPs were 50 nm in radius rather than 8 nm, the surface energy decreases by a factor of 6.25.

Table 3.2: Size-dependent Surface Energy for 1 g of Three Different Sized Gold Spheres

Radius (cm)	# AuNPs	Total Surface Energy (J)
0.1	1.2E+01	1.5E-04
5.00E-06	9.9E+13	3.1
8.00E-07	2.4E+16	19.4

Higher AuNP surface energy increases the attraction between adjacent nanoparticles, preferentially driving agglomeration. Researchers suggest that 100 nm approaches the upper limit of AuNP size which can still traverse the cell membrane of many types of cancer cells [31]. Using a 100-nm diameter AuNP rather than a 17-nm diameter AuNP will help mitigate agglomeration issues during neutron activation due to its lower surface energy.

We purchased the 100 nm AuNPs from Cytodiagnostics to study surfactant stability compared to the 10 nm Nanopartz sample. Since 100-nm AuNPs have a much larger surface area to which mAbs may attach and therefore many more attached antibodies per nanoparticle, directional mAb conjugation is less critical. Non-directional conjugation is simple; the mAbs will undergo passive adsorption to the AuNP surface mediated by their respective electrostatic and hydrophobic interactions. Antibody adsorption to AuNPs is most successful at or around the isoelectric point of the antibody of interest (the pH at which the antibody carries no electrical charge). Fortunately the isoelectric point of PE CD340 is 7.2, which is almost exactly the pH of the stock 100 nm AuNP mixture provided by Cytodiagnostics, and close to that of water. This implies that

buffers for pH titration and optimization may not be necessary. In order to reach conjugation saturation, the mAb:AuNP ratio was no less than 1 μg of pure CD340 mAb per 100 μL of stock AuNP mixture (or 3.84E8 AuNPs since the stock solution had a density of 3.84×10^{9} AuNPs mL^{-1}). Knowing that CD340 weighs approximately 185 kD, this yields a mAb:AuNP molar mixing ratio of about 8500:1. The CD340 provided by Biolegend was already sufficiently diluted such that a mixing ratio of 1 mL of mAb stock solution to 1 mL of AuNPs stock mixture yielded a mAb:AuNP molar ratio of about 10,600:1. This mixture was gently stirred using a vortex machine at 4 °C overnight to drive the conjugation reaction. The sample was centrifuged for 10 minutes at 400x RCF and the supernatant was extracted; 2 mL of triple-distilled water was added such that the sample contained only conjugated AuNPs in water.

To ensure successful antibody attachment and appropriate pH conditions, we added 100 μL of 10% NaCl solution to the conjugated AuNPs. According to the vendor, if the conjugation conditions were suboptimal, the NaCl would have induced aggregation and changed the color of the mixture to the naked eye. The addition of NaCl had no effect, suggesting that the above conjugation methods were successful.

3.4 Changing Reactor Conditions

One additional method to mitigating AuNP agglomeration during neutron activation is to use a nuclear reactor with a much larger neutron flux. The 1 MW TAMU NSC nuclear reactor has a neutron thermal flux of approximately 10^{13} n s^{-1} cm^{-2}. If we have access to a nuclear reactor with a thermal neutron flux of about 6×10^{14} n s^{-1} cm^{-2}.

With a flux this large, it may be possible to significantly reduce AuNP activation time. If such a high flux reactor also maintains a lower full power primary coolant outlet temperature (T_{hot}), this could also improve the likelihood of surfactant survival.

Utilizing activation methods/reactors outside of TAMU is currently outside the scope of this project. It may be possible, however, to prevent irreparable agglomeration during 100 nm AuNP activation in the TAMU NSC reactor due simply to the larger particle size. The 100 nm AuNPs are composed of many more gold nuclei, and will therefore contain more radioactive atoms per nanoparticle compared to 10 nm AuNPs under identical activation conditions. This will allow us to activate the nanoparticles for a much shorter period of time while maintaining the requirement that every nanoparticle must contain radioactive atoms. If agglomeration is apparent but minimal due to this shorter activation time, the nanoparticles may be sonicated to potentially re-disperse them. Furthermore, subsequent nanoparticle activations will not incorporate aluminum foil padding (see Figure 2.3). This will decrease the gamma decay dose from the radioactive isotope ^{28}Al. Although the added aluminum foil is relatively transparent to neutrons (see Table 3.1), a significant quantity of aluminum foil has been present in previous activation attempts. Considering ^{28}Al decays are accompanied with 1.779 MeV gamma rays with an intensity of 100% and a half-life of approximately 2.24 minutes, gamma radiation-induced surfactant failure can be slightly reduced by not incorporating aluminum foil for subsequent activations. Other present nuclides may contribute to neutron absorption-induced gamma exposure through interactions such as ^{23}Na (n,γ)

^{24}Na, however interactions which involve surfactant nuclides are unavoidable as they are crucial to nanoparticle anticoagulant stability.

3.5 Calculated Radioactive Nuclei per 100 nm Diameter Nanoparticle

As previously discussed, we postulate that a lower limit of nano-TRT treatment efficacy requires that each nanoparticle have at least one radioactive atom in order for the AuNP to provide radiotherapeutic effect (see page 25). When using a 100 nm diameter AuNP instead of 10 nm, NAA shows that the average number of radioactive atoms per AuNP may be increased dramatically even while activating the nanoparticles for a much shorter period of time. Activating 100 nm AuNPs in the TAMU NSC reactor for 1 hour yields an average of about 161 radioactive atoms per nanoparticle (after 24 hours of decay, this will be approximately 124 radioactive atoms per nanoparticle), that is significantly higher than that of using 10 nm AuNPs (nearly 85% of these nanoparticles would not contain any radioactive atoms after 1 hour of activation). Figure 3.6 below shows the Poisson probability distribution of radioactive atoms (^{198}Au) per 100 nm nanoparticle when activated for 1 hour in the TAMU NSC nuclear reactor (and allowed to decay for 24 hours).

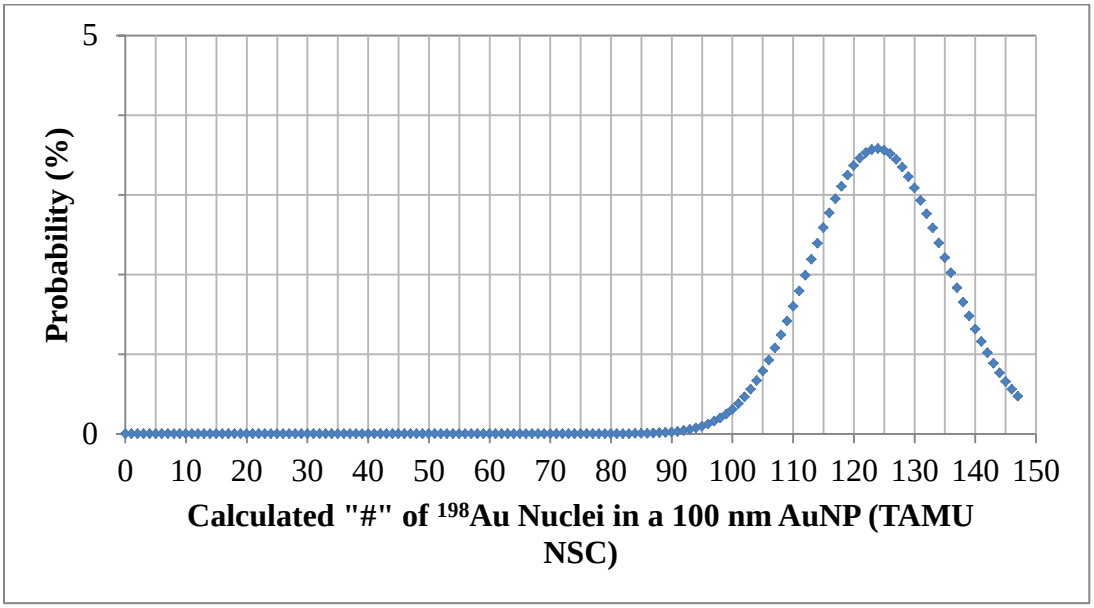

Fig. 3.6: Discrete Poisson Distribution of Calculated ^{198}Au Nuclei per 100 nm Diameter AuNP Given t_{irr} = 1 h, and t_d = 24 h in TAMU NSC Nuclear Reactor

While it is likely that there will be fewer nanoparticles per cancer cell, each nanoparticle now has orders of magnitude more radioactive nuclei. Based on the activation conditions shown in Figure 3.6, the average nanoparticle contains approximately 124 radioactive atoms. Again assuming infinite AuNP residence time, and the dose from the primary β^- emission to cancerous tissue vs. 100 nm AuNPs per cell is shown below in Figure 3.7.

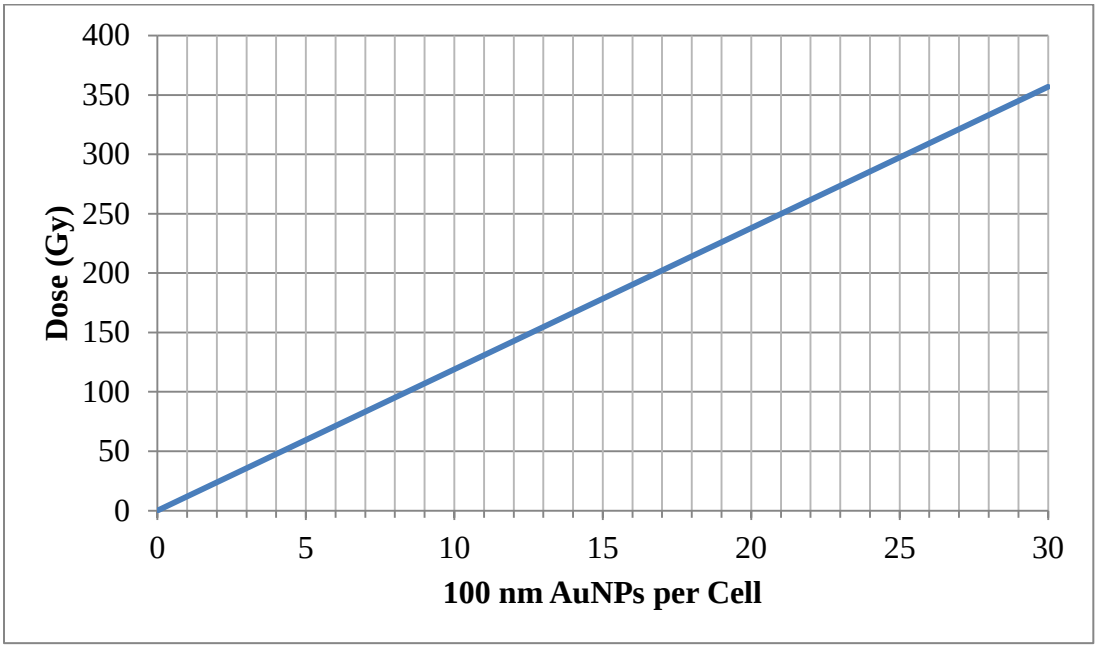

Fig. 3.7: Calculated Dose (Gy) from Primary β^- Emission of TAMU NSC-Activated 100 nm AuNPs vs. 100 nm AuNPs per Cell, Given t_{irr} = 1 h, and t_d = 24 h, Assuming Infinite AuNP Residence Time Approximation

3.6 Final AuNP Activation: 100 nm Diameter without Aluminum Foil

Previous attempts to produce radioactive AuNPs (both 10 nm and 17 nm) ended in surfactant failure and irreversible agglomeration. We hypothesized that decreasing the surface energy (by using larger nanoparticles), not filling the activation vessel with aluminum foil, and activating for a shorter period of time would prevent surfactant failure and agglomeration. The quartz ampoule survived the activation, and did not crack during insertion or removal from the reactor core, suggesting that the aluminum foil padding was not necessary. After one hour of activation and two hours of decay, the sample solution had not yet changed color and no particulates were visible, indicating

that surfactant failure was negligible to the naked eye. The sample's ^{198}Au activity after two hours of decay was about 50 μCi, and the ^{24}Na activity (which has a half-life of about 15 hours, compared to ^{198}Au's 2.69 days) was about 0.14 μCi. We had intended to conduct TEM or AFM to further characterize the AuNPs after activation; however, the project was canceled immediately after this activation despite its success. Subsequently, sample characterization followed by nano-TRT cell treatment was not carried out.

3.7 Flow Cytometry Characterization

Our initial supply of antibodies was small, and we were unable to purchase more due to lack of funding. We had to experiment with the mAbs sparingly. Before doing so, however, we explored flow cytometry with 10 nm AuNPs, 100 nm AuNPs, and SK-BR-3 cells to establish control groups. As shown below in Figure 3.8 and Figure 3.9, the absorption spectra of the two different sized nanoparticles differ considerably. The absorption/emission spectrum of PE is also shown in Figure 3.10. The Accuri C6 Flow Cytometer excitation lasers (488 nm and 640 nm) have been superimposed onto the figures. Note that the concentrations of 10 nm AuNPs mL^{-1}, 100 nm AuNPs ml^{-1}, and PE-CD340 mAbs mL^{-1} are 5.98×10^{12}, 3.84×10^{9}, and 4.07×10^{13}, respectively.

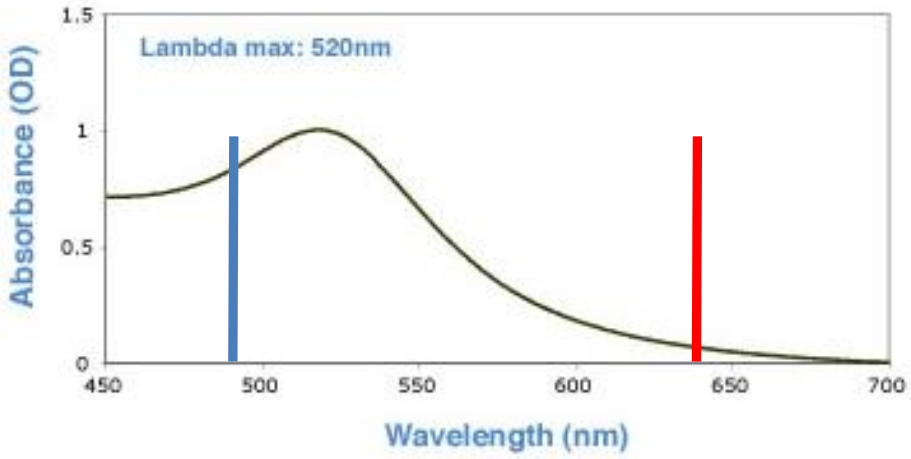

Fig. 3.8: Absorbance vs. Excitation Wavelength Spectrum of 10 nm AuNPs (Cytodiagnostics) Using UV-Vis Spectroscopy, with Accuri C6 Flow Cytometer Excitation Lasers (488 nm in Blue, 640 nm in Red) Superimposed

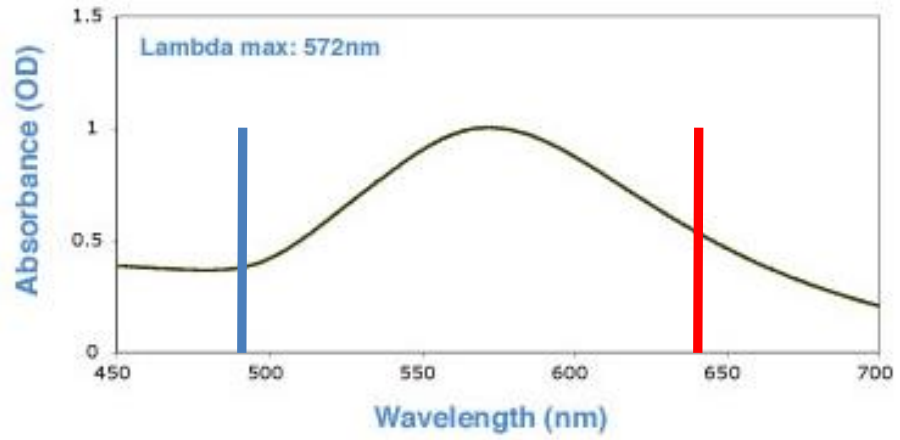

Fig. 3.9: Absorbance vs. Excitation Wavelength Spectrum of 100 nm AuNPs (Cytodiagnostics) Using UV-Vis Spectroscopy, with Accuri C6 Flow Cytometer Excitation Lasers (488 nm in Blue, 640 nm in Red) Superimposed

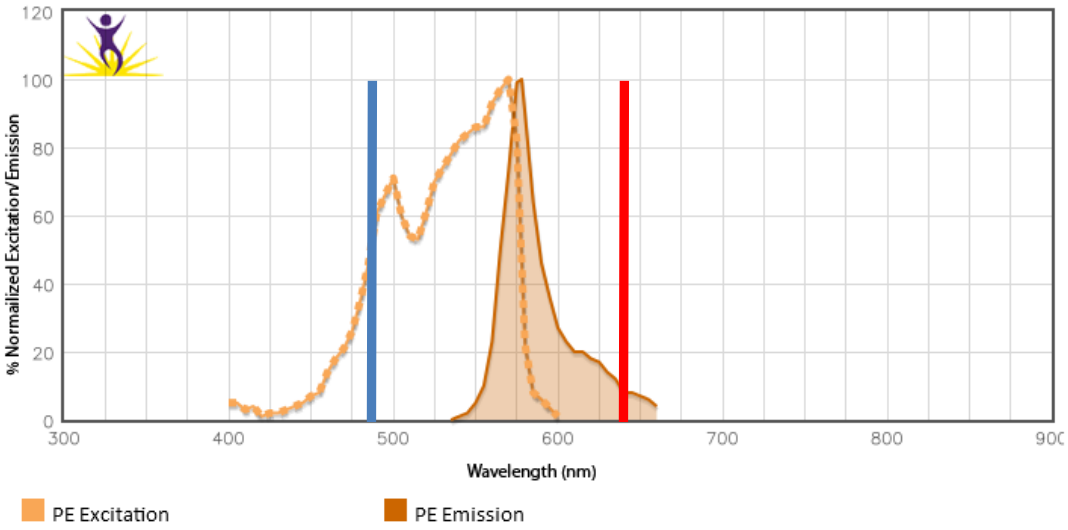

Fig. 3.10: Absorbance vs. Excitation Wavelength Spectrum of PE CD340 mAbs (Biolegend), with Accuri C6 Flow Cytometer Excitation Lasers (488 nm in Blue, 640 nm in Red) Superimposed [59]

Both lasers miss the SPR of both 10 nm and 100 nm AuNPs. The 488 nm laser is well within the absorption region (normalized absorbance of about 70%) of the 10 nm AuNPs to yield a detectable signal, while the 640 nm laser will yield almost no signal (normalized absorbance of about 5%). The 100 nm AuNPs will absorb both the 488 nm laser and the 640 nm laser with normalized absorbance of about 40% and 60%, respectively. Figure 3.11 below shows the flow cytometer forward scattering (FSC) and side scattering (SSC) associated with bare 10 nm AuNPs (left) and bare 100 nm AuNPs (right). The 10 nm AuNPs are both older and more concentrated, which may contribute to the higher degree of forward scattering and the greater number of counts. These experiments show a clear side scattering trend associated with the nanoparticles. Note

that all flow cytometry experiments were conducted with the same flow conditions for the same 5 minute period. The total number of counts for the 10 nm AuNPs, 100 nm AuNPs, and PE CD340 mAbs (see Figure 3.12) were 6,429, 587, and 47,492, respectively. Note that it is difficult to determine mAb attachment per nanoparticle, or precise nanoparticle concentration in the conjugated sample (see Figure 3.13) due to inefficiencies in removing supernatant; however the conjugated AuNPs yielded 692 counts.

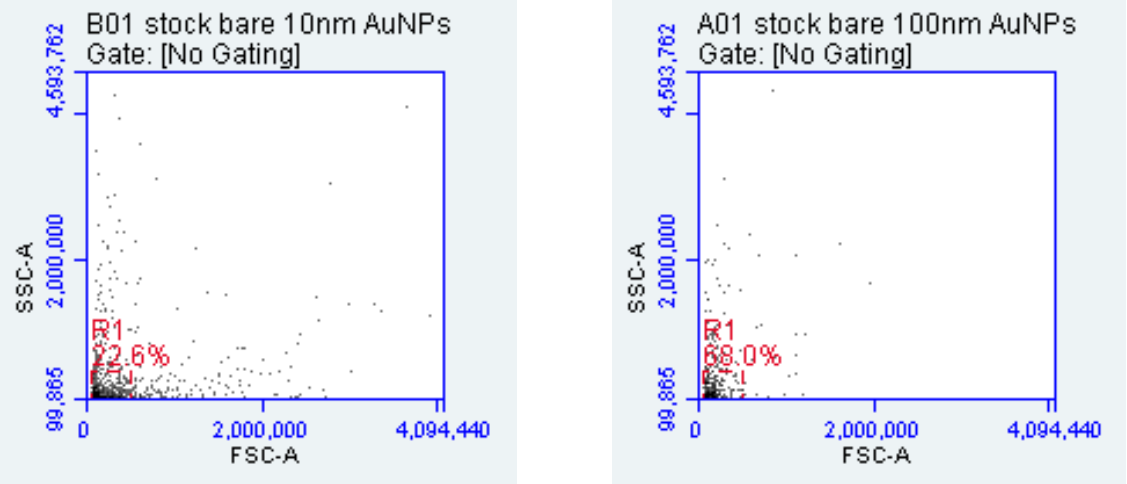

Fig. 3.11: Flow Cytometry Scattering of Stock Bare 10 nm (Left) and 100 nm (Right) AuNPs

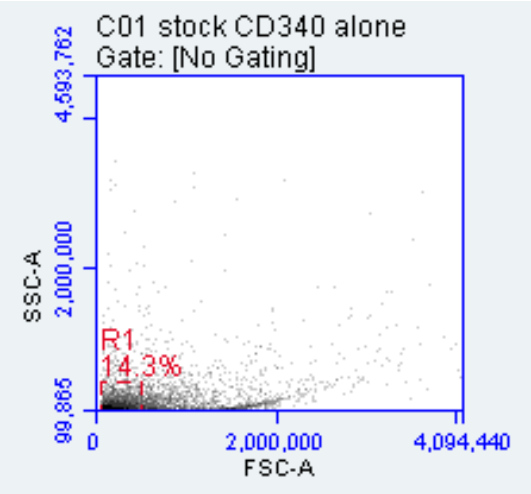

Fig. 3.12: Flow Cytometry Scattering of Stock Bare PE CD340 mAbs

Contrary to the side scattering associated with the nanoparticles, the PE CD340 mAbs appear to show a large degree of forward scattering, shown below in Figure 3.14. We then conjugated the 100 nm AuNPs with PE CD340, whose flow cytometry results yielded inconclusive information shown below in Figure 3.13. If conjugation were unsuccessful, we would expect to see the spectrum dominated by bare PE CD340 with the bare 100 nm AuNP spectrum superimposed onto it. This in fact did not occur. Not only does this suggest that something has altered the PE CD340 spectrum (i.e. they may now be attached to an AuNP), but our attempts to remove the supernatant were relatively successful. The 100 nm AuNPs are quite large, and the SPR can dramatically increase the total photon interaction cross section of materials (as compared to bulk) based on particle size and excitation wavelength.

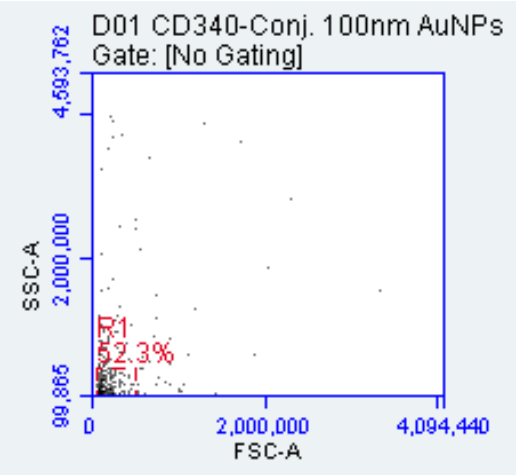

Fig. 3.13: Flow Cytometry Scattering of PE CD340-Conjugated 100 nm AuNPs

We had intended on exploring flow cytometry by treating SK-BR-3 cells with conjugated AuNPs, unconjugated AuNPs, and mAbs alone; however sufficient antibodies were not available. The SK-BR-3 cells do indeed have a distinct scattering spectrum (Figure 3.14), however, which suggests that these experiments may yield useful information.

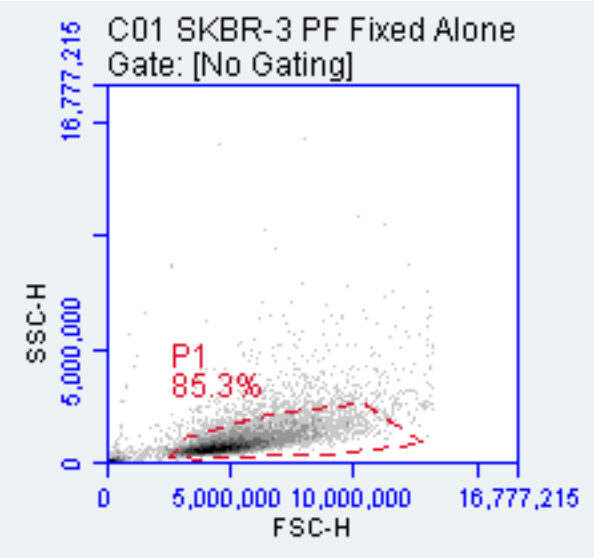

Fig. 3.14: Flow Cytometry Scattering of SK-BR-3 Cancer Cells Alone

3.8 Gel Electrophoresis Characterization and mAb-AuNP Conjugation

The experiments in the previous section suggest that flow cytometry does not yield conclusive evidence of mAb-conjugated 100 nm AuNPs with these spectra, so other methods to determine conjugation were explored. The first experiment using gel electrophoresis was conducted simply to observe bare AuNP response to electrophoresis as a function of size. Shown in Figure 3.15 below from left to right, lanes 1-5 are bare 10 nm AuNPs (Cytodiagnostics), lanes 6-10 are bare 100 nm AuNPs (Cytodiagnostics), and lanes 11-15 are PE CD340 alone.

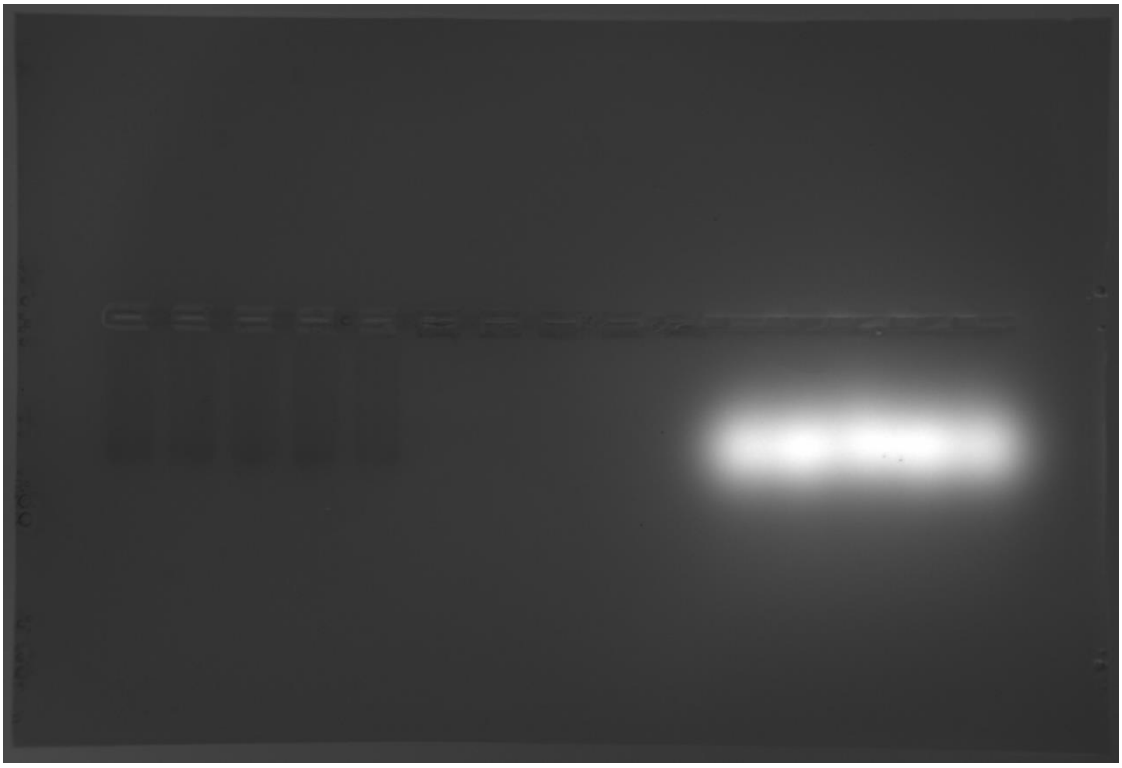

Fig. 3.15: Agarose Gel Electrophoresis with Bare 10 nm AuNPs (Lanes 1-5), Bare 100 nm AuNPs (Lanes 6-10), and PE CD340 Alone (Lanes 11-15)

Figure 3.15 is the original image which may be difficult to see due to the bright signal from the PE CD340. Figure 3.16 below shows this image without lanes 11-15 to resolve contrast, which may be easier to see the AuNPs more distinctly. Note that the 100 nm sample is less concentrated, which accounts for the weak signal. This simple experiment revealed that bare 10 nm AuNPs are small enough to travel through the agarose gel under these conditions, while the bare 100 nm AuNPs are too large to do so.

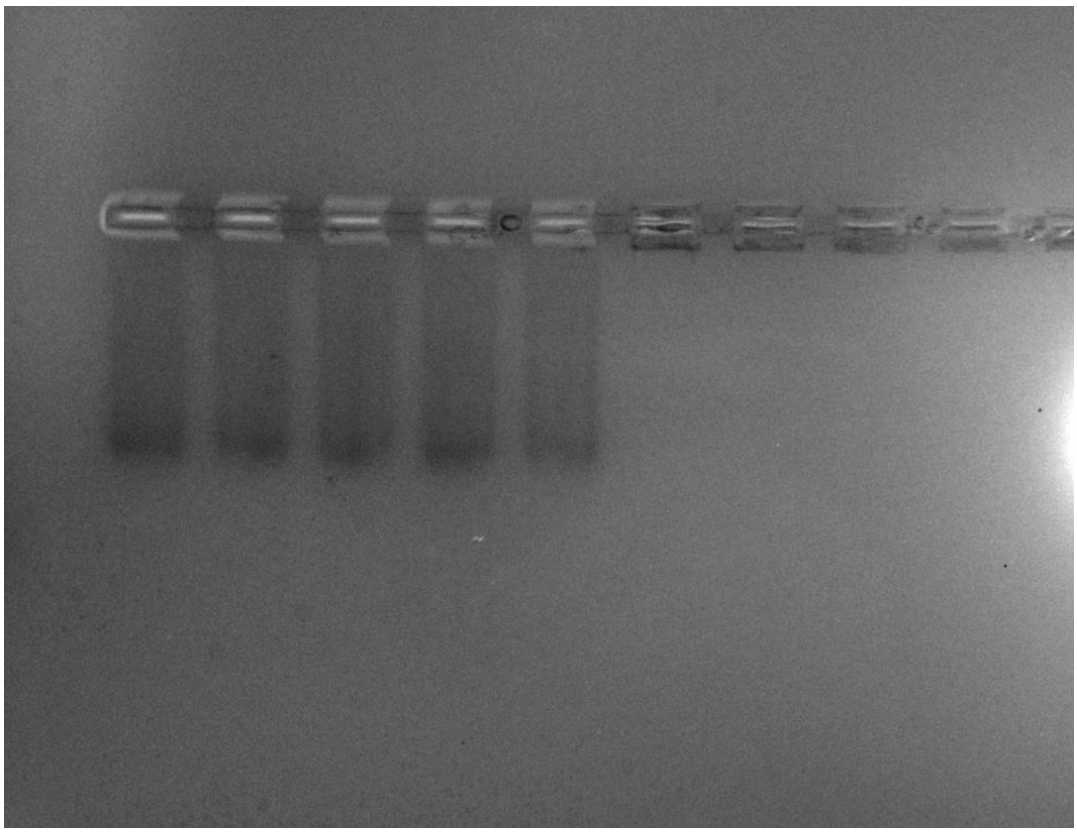

Fig. 3.16: Figure 3.15 with Resolved Contrast; Bare 10 nm AuNPs (Lanes 1-5), Bare 100 nm AuNPs (Lanes 6-10), and Lanes 11-15 Cropped Out

We replicated the previous electrophoresis experiment with 100 nm AuNPs (Cytodiagnostics), both bare and mAb-conjugated. Recall that CD340 is tagged with PE, which has spectral properties similar to that of the fluorophore Cy3 (see Figure 2.13). Shown below in Figure 3.17, lanes 1-5 contain 100 nm AuNPs conjugated with PE CD340, lanes 6-10 contain bare 100 nm AuNPs, and lanes 11-15 contain PE CD340 alone.

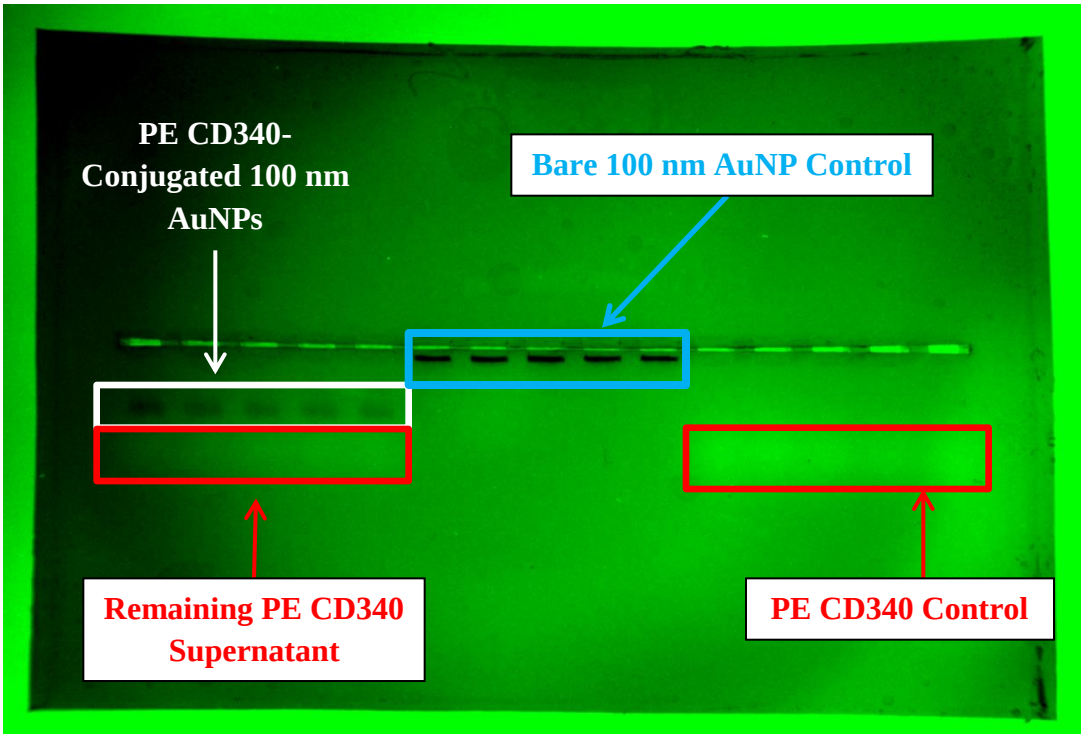

Fig. 3.17: Agarose Gel Electrophoresis with PE CD340-Conjugated 100 nm AuNPs (Lanes 1-5), Bare 100 nm AuNPs (Lanes 6-10), and PE CD340 Alone (Lanes 11-15)

This experiment reveals several important features. Comparing Figures 3.15 and 3.16 (lanes 1-10) with 3.17 above (lanes 6-10), it is again obvious that the larger size of the 100 nm AuNPs retards their travel through the gel such that, under identical operating conditions, the bare 100 nm AuNPs barely moved in comparison to the 10 nm AuNPs. Figure 3.17 also strongly suggests that the AuNPs in lanes 1-5 are indeed conjugated since the AuNPs in lanes 1-5 (dark black rectangles) moved much further than the bare AuNPs in lane 6-10. The bright shapes on the left in lanes 1-5 are consistent with the PE CD340 antibodies in the right in lanes 11-15, indicating that our

attempt to fully remove the remaining unconjugated mAb supernatant was not perfect. See Figure 3.18 for resolution-resolved views of lanes 1-5 (left), 6-10 (middle), and 11-15 (right).

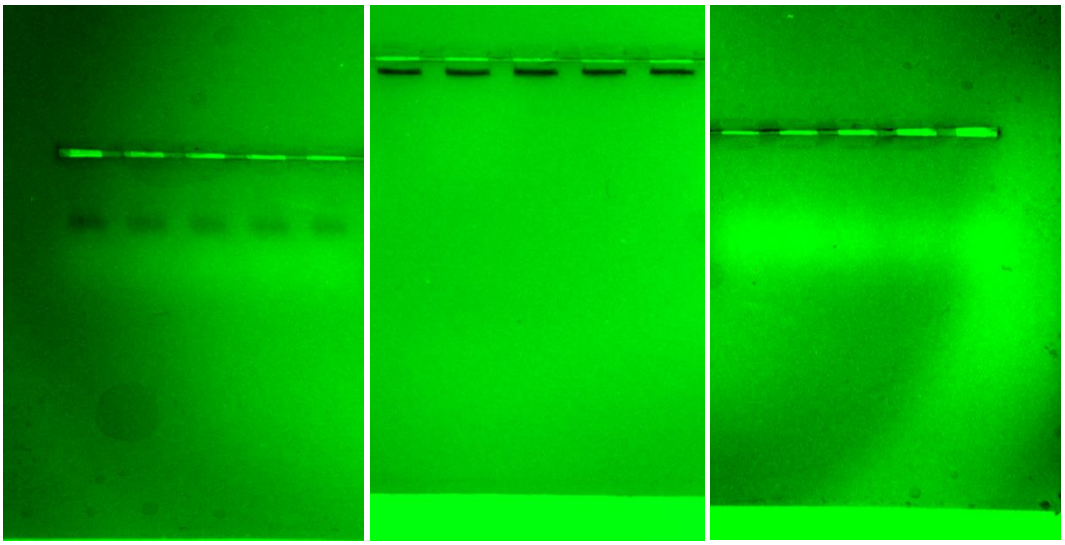

Fig. 3.18: Close-Up Resolution-Resolved Views of Lanes 1-5 of Fig. 3.19 with PE CD340-Conjugated 100 nm AuNPs (Left), Lanes 6-10 of Fig. 3.19 with Bare 100 nm AuNPs (Middle), Lanes 11-15 of Fig. 3.19 with and PE CD340 Alone (Right)

3.9 Cytotoxic Effects of Non-Radioactive AuNPs

We decided to explore the cytotoxic effect of non-radioactive AuNPs in SK-BR-3 cancer cells by introducing various concentrations of AuNPs to cells and observing cellular response as a function of time using the xCELLigence system. Our system is an 8x2 (16-well) plate for which the wells are defined as shown below in Figure 3.19 and loaded with 10 μL incremental titrations of increasingly dilute AuNP mixture yielding

the concentrations shown in Table 3.3. Due to the small size of the 10 nm AuNPs, the AuNPs are significantly more abundant than cells. The control group wells H1 and H2 have no cells or AuNPs. The cellular response to the AuNP treatment as a function of time is shown in Figure 3.20.

Table 3.3: Non-Radioactive 10 nm AuNP Cytotoxicity Experiment, Well Layout Information at Initiation of Treatment

Well ID	Cell Type	Cells Well^{-1}	Compound	Concentration (AuNPs Well^{-1})	Concentration (AuNPs Cell^{-1})
A1	SK-BR-3	120,000	10 nm AuNPs	3.00E+10	250,000
B1	SK-BR-3	120,000	10 nm AuNPs	1.50E+10	125,000
C1	SK-BR-3	120,000	10 nm AuNPs	7.50E+09	62,500
D1	SK-BR-3	120,000	10 nm AuNPs	3.75E+09	31,250
E1	SK-BR-3	120,000	10 nm AuNPs	1.88E+09	15,667
F1	SK-BR-3	120,000	10 nm AuNPs	9.38E+08	7,817
G1	SK-BR-3	120,000	10 nm AuNPs	0	0
A2	SK-BR-3	120,000	10 nm AuNPs	3.00E+10	250,000
B2	SK-BR-3	120,000	10 nm AuNPs	1.50E+10	125,000
C2	SK-BR-3	120,000	10 nm AuNPs	7.50E+09	62,500
D2	SK-BR-3	120,000	10 nm AuNPs	3.75E+09	31,250
E2	SK-BR-3	120,000	10 nm AuNPs	1.88E+09	15,667
F2	SK-BR-3	120,000	10 nm AuNPs	9.38E+08	7,817
G2	SK-BR-3	120,000	10 nm AuNPs	0	0

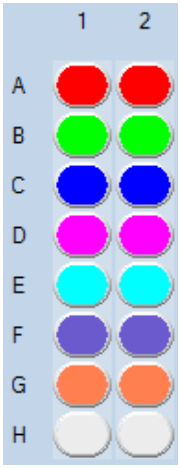

Fig. 3.19: Legend for Non-Radioactive 10 nm AuNP Cytotoxicity Experiment, 8x2 Labeled Wells

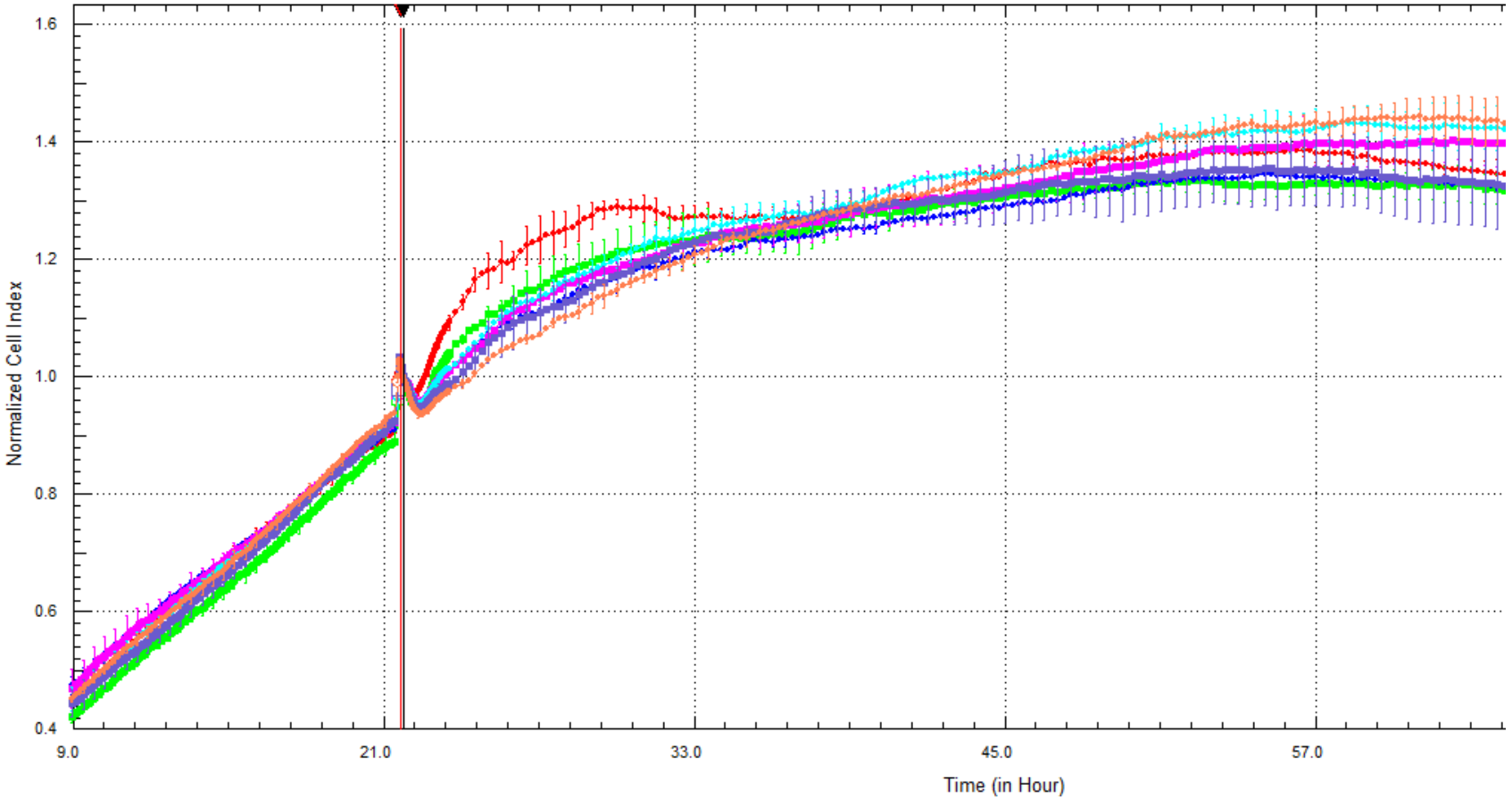

Fig. 3.20: Non-Radioactive 10 nm AuNP Cytotoxicity Experiment, Mean (± Standard Deviation) Cell Index vs. Time

The cytotoxic effects of non-radioactive 10 nm AuNPs can be seen above in Figure 3.20. The vertical line at 21 hours 35 minutes of cell growth signifies when the non-radioactive 10 nm AuNP treatment was initiated. While the impact of the nanoparticles is noticeable, two conclusions may be drawn with reasonable confidence: the cytotoxic effects of non-radioactive 10 nm AuNPs (at least up to concentrations of 250,000 AuNPs $cell^{-1}$) are non-lethal. Secondly, over the lifetime of the experiment there are variations which may or may not be associated with the nanoparticles at all. While the control group that wasn't treated with any AuNPs (G1 and G2) does have the highest cell index as expected, the group which was treated with the highest AuNP concentration (A1 and A2) did not show the lowest cell index, indicating random variations associated with cell growth.

This experiment also suggests that the presence of a high density of 10 nm AuNPs has little to no effect on the measured impedance of the device. Prior research has shown that AuNP cytotoxicity is a strong function of nanoparticle size, with smaller nanoparticles being more cytotoxic; this suggests that cellular response to the 100 nm AuNPs will be even less noticeable [74], and will be discussed later in this section.

This first 10-nm non-radioactive AuNP cytotoxicity experiment yields information which would otherwise would not be observable from a traditional clonogenic assay, and can best be illustrated by looking only at the two groups which had the highest (A1 and A2) and lowest (G1 and G2) concentrations of gold nanoparticles shown below in Figure 3.21. If the AuNPs caused a noticeable change in detector impedance, the rise in wells A1 and A2 would have been permanent. The cell index rises, and then within 10 hours drops down again, indicating a defensive cellular response at the beginning of treatment followed by noticeable cytotoxic effects hours later.

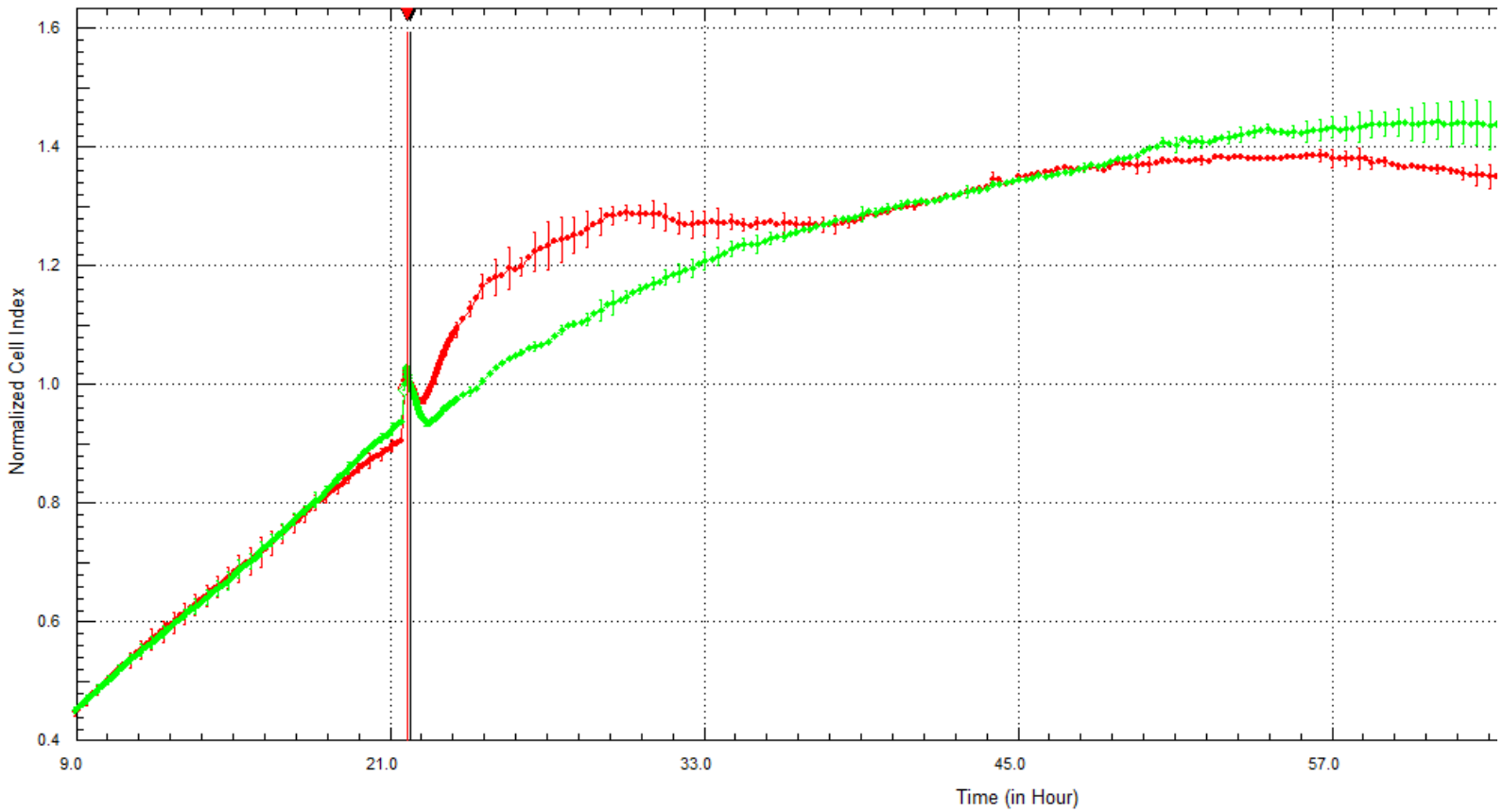

Fig. 3.21: Non-Radioactive 10 nm AuNP Cytotoxicity Experiment, Mean (± Standard Deviation) Cell Index vs. Time of 250,000 AuNPs/Cell (Red) and Zero AuNPs/Cell (Green)

We ran an additional experiment with the 100 nm AuNPs from Cytodiagnostics to determine gold cytotoxicity changes due to using larger nanoparticles. See Table 3.4 and Figure 3.22 below for the concentrations and "Well ID's" for the 100 nm AuNP cytotoxicity experiment.

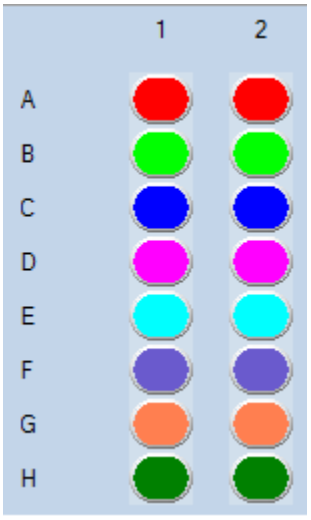

Fig. 3.22: Legend for Non-Radioactive 100 nm AuNP Cytotoxicity Experiment, 8x2 Labeled Wells

Table 3.4: Non-Radioactive 100 nm AuNP Cytotoxicity Experiment, Well Layout Information at Initiation of Treatment

Well ID	Cell-Type	Cells Well^{-1}	Compound	Concentration (AuNPs Well^{-1})	Concentration (AuNPs Cell^{-1})
A1	SK-BR-3	120,000	100 nm AuNPs	3.84E+07	320
B1	SK-BR-3	120,000	100 nm AuNPs	1.92E+07	160
C1	SK-BR-3	120,000	100 nm AuNPs	9.60E+06	80
D1	SK-BR-3	120,000	100 nm AuNPs	4.80E+06	40
E1	SK-BR-3	120,000	100 nm AuNPs	2.40E+06	20
F1	SK-BR-3	120,000	100 nm AuNPs	1.20E+06	10
G1	SK-BR-3	120,000	100 nm AuNPs	0	0
A2	SK-BR-3	120,000	100 nm AuNPs	3.84E+07	320
B2	SK-BR-3	120,000	100 nm AuNPs	1.92E+07	160
C2	SK-BR-3	120,000	100 nm AuNPs	9.60E+06	80
D2	SK-BR-3	120,000	100 nm AuNPs	4.80E+06	40
E2	SK-BR-3	120,000	100 nm AuNPs	2.40E+06	20
F2	SK-BR-3	120,000	100 nm AuNPs	1.20E+06	10
G2	SK-BR-3	120,000	100 nm AuNPs	0	0

The 100 nm AuNPs were added to the wells at approximately 23.5 hours, shown by the collective line humps. As shown below in Figure 3.23, the cell sample became contaminated with bacteria at approximately 38 hours, evident by the drastic increase in cell index toward the end of the timeline. The downward and upward jumps at approximately 41.5 hours are a result of opening the incubator and removing the well plates for inspection. The bacteria did not begin to affect the sample significantly until at least 14 hours after the 100 nm AuNPs were added to the cell samples. This suggests that even though the samples were contaminated, it also demonstrates that 100 nm non-

radioactive AuNPs have no cytotoxic effect to the SK-BR-3 cells due to the lack of growth rate change before/after treatment administration.

Wells A-F were all treated with 10 μL of solution with varying AuNP concentrations diluted in triple distilled water, and wells G1-G2 were treated with 10 μL of pure triple distilled water as a control. Figure 3.23 clearly shows that wells G1 and G2 were not contaminated with bacteria while wells A-F were. This indicates that the water used to dilute the AuNP mixture was not contaminated, and further reveals that our treatment procedures were successfully executed in a sterile manner. Therefore the stock 100 nm AuNP mixture from the vendor itself may be contaminated with bacteria. As a result, subsequent experiments with this batch of nanoparticles will first be treated with penicillin prior to combining with the cells to kill any bacteria which may be in the stock AuNP mixture.

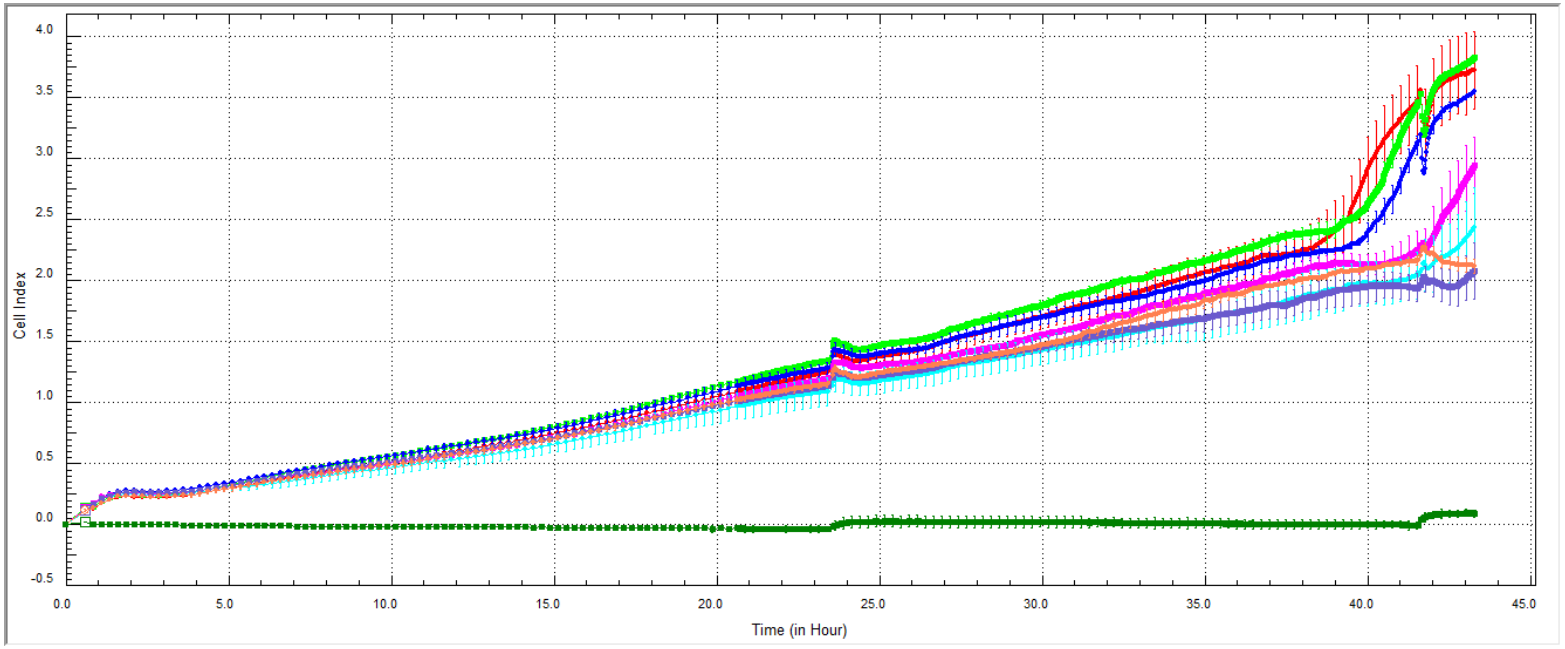

Fig. 3.23: Non-Radioactive 100 nm AuNP Cytotoxicity Experiment, Mean (± Standard Deviation) Cell Index vs. Time

3.10 AuNP Endocytosis

Figure 3.21 shows a clear cellular response due to treating with non-radioactive AuNPs. One likely cause of this phenomenon is a process called endocytosis, where the nanoparticles with pass through the cell membrane by one of several various "engulfing" mechanisms [75]. The optimal AuNP size for Trastuzumab-conjugated nanoparticles to maximize cancerous AuNP endocytosis is 50 nm in diameter [76]. Conjugated AuNP endocytosis enters the cell through receptor-mediated endocytosis, shown below in Figure 3.24 [76]. The key factors which influence this process are the size, shape, and charge of the nanoparticle, the conjugation density and orientation, the cellular receptor expression levels, and cellular response mechanisms.

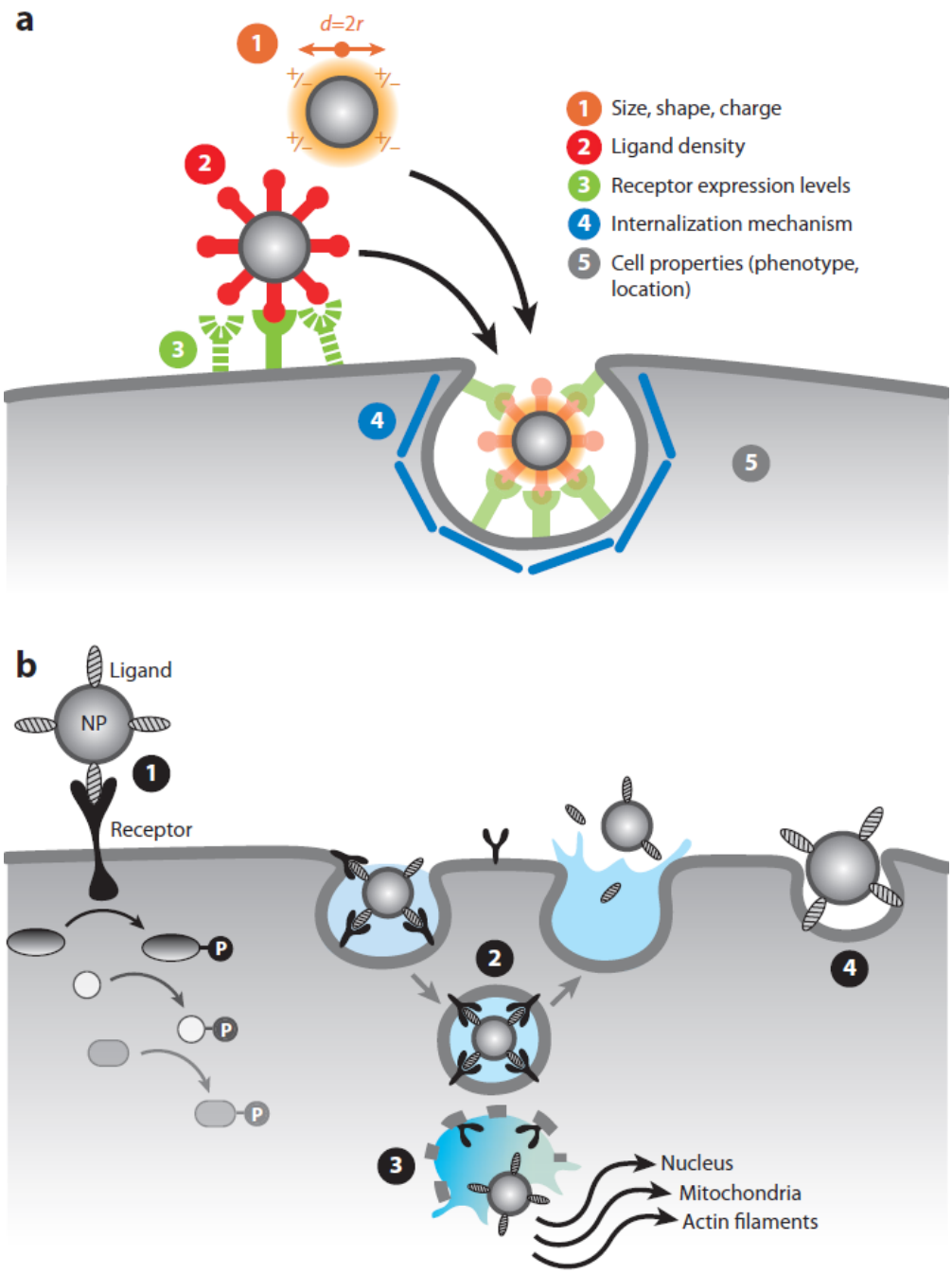

Fig. 3.24: Illustration of Receptor-Mediated Nanoparticle Endocytosis [76]

4. DERIVATION OF TRT DOSIMETRY USING PROBABILITY THEORY

The ultimate objectives of this derivation are (1) to calculate how many radioactive atoms per AuNP are required to produce a desired dose to tumors of varying size, and (2) to calculate the resulting dose to surrounding healthy tissue. There are several ways to calculate these doses [77]. Alternatively, one common method to determine the degree with radiation effects tissue is to generate a code using a computer program, such as MCNPX, and run it a large number of times to simulate the particles depositing energy as they travel through tissue. For this research, however, we have chosen to calculate these dose distributions by using probability theory, specifically the manipulation of nested multivariable trigonometric weight functions. This method is advantageous in that probability distribution functions (PDFs) can be easily retrofitted with pharmacokinetic data specific to the patient or cancer type, allowing a simple coupling of pharmacokinetics and dosimetry [78, 79]. For a simple 2-dimensional example of manipulating weight functions, see the Appendix.

The pharmacokinetics associated with nano-TRT may depend on several factors that may dramatically affect the nanoparticle distribution in the patient's body. For this reason, we derive a general formula which can be used to calculate the doses to healthy and cancerous tissue. We demonstrate its applicability by considering AuNPs which are inside of or attached to cancer tissue for this derivation. Not all AuNPs may be attached to or inside cancerous tissue; however, this is dependent upon pharmacokinetics and can

be accounted for using appropriate probability distributions. To simplify the equations involved in this example, we have assumed that the tumors and cells are approximately spherical in shape, and that the AuNPs are isotropically distributed within the tumor. We also approximate an isotropic AuNP distribution within individual cancer cells (important if individual cancer cells such as leukemia are treated and the AuNPs are endocytosed) assuming the AuNP movement within the cytoplasm is random [80, 81]. Emission occurs from within the nanoparticles; however, because the nanoparticles are sufficiently small, we approximate that the AuNPs are points rather than spheres, ignoring AuNP self-shielding and dose enhancement effects as emissions exit the nanoparticle. We also assume that cancerous tissue and healthy surrounding tissue are physically identical, and tissue density is constant; this may not be true for tumors in or very close (within a few millimeters) to bone or other dense deposits.

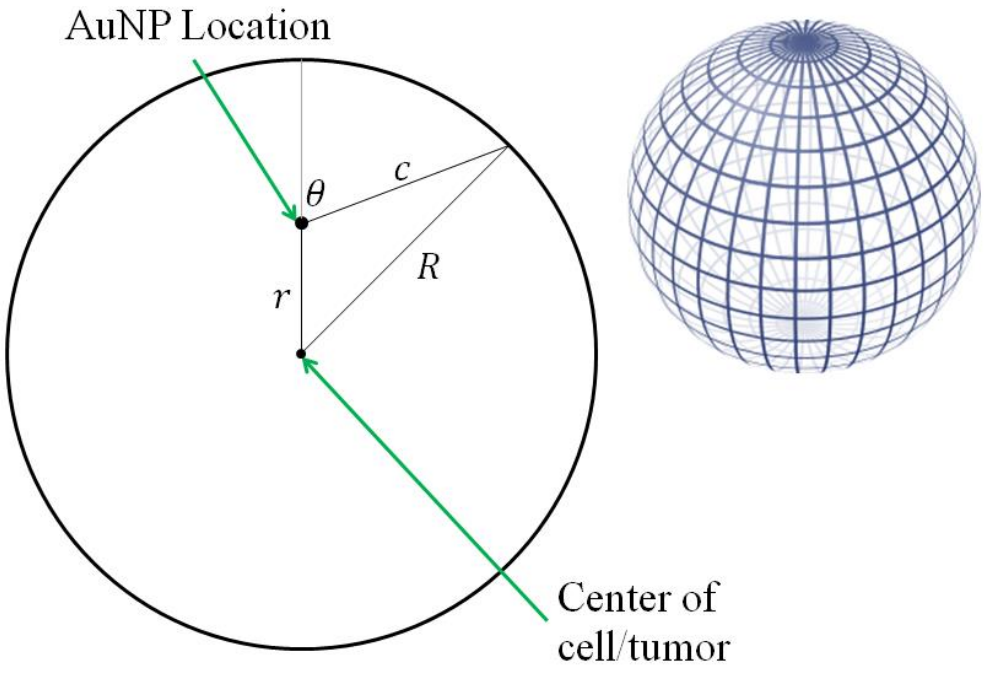

Fig. 4.1: Schematic of Radioactive AuNP Geometry inside Cancerous Cell/Tumor

(Eq. 4.1)

$$c = \sqrt{R^2 - r^2 \sin^2(\theta)} - r\cos(\theta)$$

When the conjugated AuNP is located inside the cancerous cell/tumor, the geometry of the AuNP, cell/tumor, and β emission path is illustrated by Figure 4.1 above. The path length of the β^- emitted by the AuNP can be calculated using the law of cosines (Equation 4.1, solved for variable "c") where...

R = the radius of the cancerous cell/tumor

θ = polar β emission angle with respect to the closest outer edge point of the boundary

r = AuNP distance from the center of the cancerous cell/tumor at the time of decay

c = the length of cancerous tissue the β emission must traverse to exit the cell/tumor

$0 \leq \theta \leq \pi$

$0 \leq r \leq R$

$0 \leq c \leq 2R$

Because of spherical symmetry, all points at distance "r" from the center can be rotated to the position shown in Figure 4.1 with no loss of generality. Note that with the given assumptions the mathematics are the same for both tumors and individual cancer cells; the only difference is the radius of the sphere, "R". With these conventions, if the β emission occurs at an angle of $\theta = 0$, then the β particle travels directly away from the center of the cell/tumor, thereby taking the shortest path possible to reach surrounding healthy tissue. If the β emission occurs at an angle of $\theta = \pi$ radians, then the β particle travels directly toward the center of the cell/tumor. In cases of treating both individual cancer cells (such as leukemia) and treating solid tumors, the probability distribution of AuNPs located a distance "r" away from the center of the cell/tumor is not constant. In order to account for this, we must apply the weight function (w), which is a mathematical device used when performing sums, integrals, or averages to give some elements more "weight" or influence on the result than other elements. This is discussed in the next section.

4.1 Tumor Dosimetry Derivation of Endocytosed Nano-TRT

We used probability theory to determine the ratio of dose deposited to cancerous tissue vs. dose to surrounding healthy tissue. Deriving these doses is complicated by the fact that β particles are not always emitted with the same energy, as shown earlier in Figure 1.8. The β particle range through tissue is therefore a distribution as well. β range through human tissue is correlated to energy by Equation 4.2 (shown from 0 to 1000 keV in Figure 4.2 below), where energy is keV and range is μm [82]. This relationship is only valid for energies between 20 eV and 2 MeV. The derivative of Equation 4.2 with respect to "R_β" gives the change in energy per unit length, also known as the "stopping power" (Equation 4.3). Note that β particles lose more energy per length traveled at lower energies than at high energies.

(Eq. 4.2)

$$E(R_\beta) = 5.9(R_\beta + 0.007)^{0.565} + 0.00413{R_\beta}^{1.33} - 0.367$$

(Eq. 4.3)

$$\frac{dE}{dR_\beta} = 3.33(R_\beta + 0.007)^{-0.435} + 0.0055{R_\beta}^{0.33}$$

∴

$$E(R_\beta) = -0.367 + \int_0^{R_{\beta,max}} \left(\frac{dE}{dR_\beta}\right) dR_\beta$$

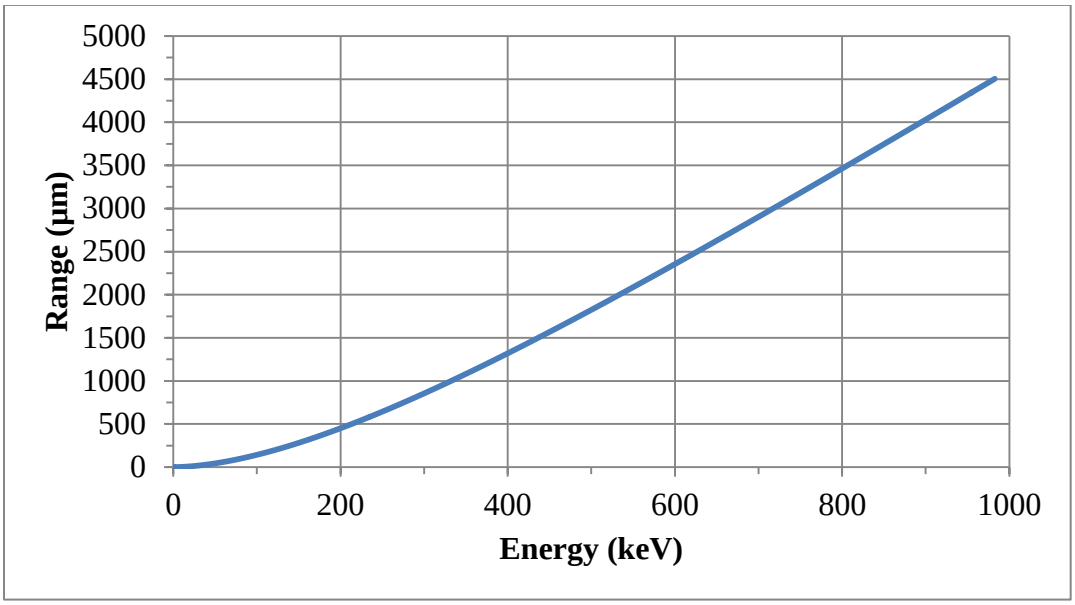

Fig. 4.2: β Range vs. Energy in Human Tissue

In probability theory, a relative probability distribution function (RPDF) is a PDF which may not be normalized, in which case is synonymous with a "weight function". The RPDF of the initial β energy from the decay of ^{198}Au shown in Figure 1.8 from Fermi theory of beta decay is complex and unwieldy to integrate. This RPDF can be approximated by a simpler polynomial equation, and the PDF of the range of β's can therefore be directly produced from Equation 4.2, shown below in Equations 4.4 and 4.5 respectively. The RPDFs derived from Fermi theory of beta decay are shown in Figures 4.3 and 4.4 below in blue while the polynomial curves are superimposed in black. More

accurate results could perhaps be achieved by using Fermi Theory rather than a polynomial approximation; but for this example, the polynomial approximation is sufficient. The polynomial in Equation 4.4 is only valid from 20 eV to 2 MeV.

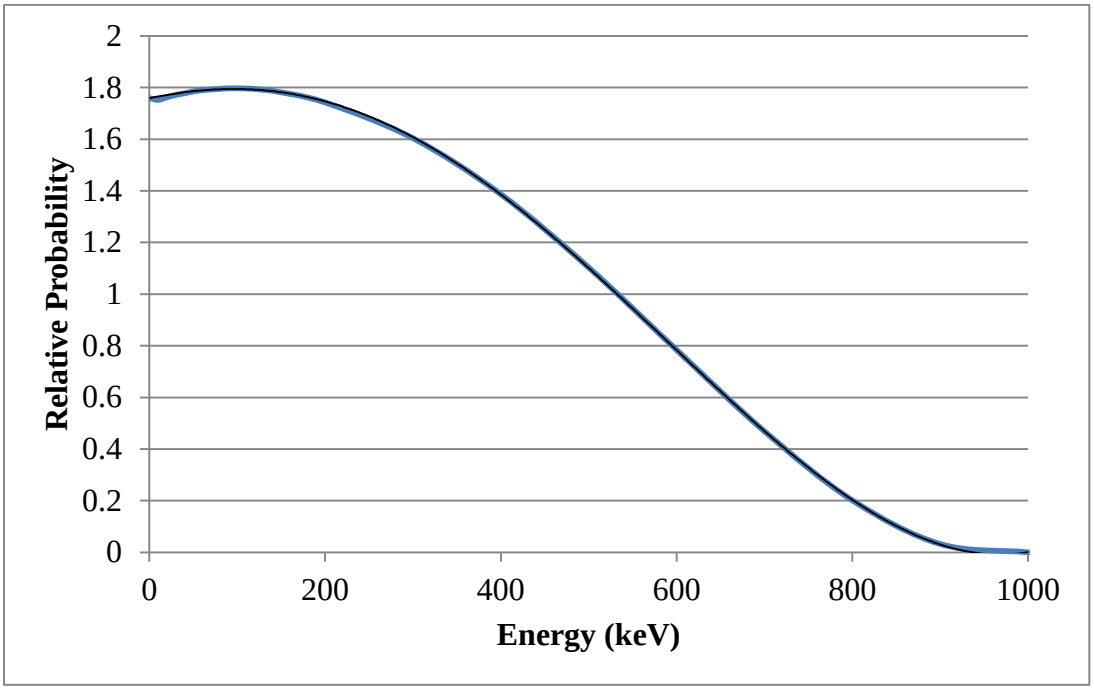

Fig. 4.3: ^{198}Au β Energy Distribution and Approximate Polynomial Function

(Eq. 4.4)

$$y = 6.857 * 10^{-19}x^6 - 3.825 * 10^{-15}x^5 + 9.971 * 10^{-12}x^4 - 6.406 * 10^{-9}x^3$$

$$- 2.882 * 10^{-6}x^2 + 6.977 * 10^{-4}x + 1.759$$

$$R^2 = 1.000$$

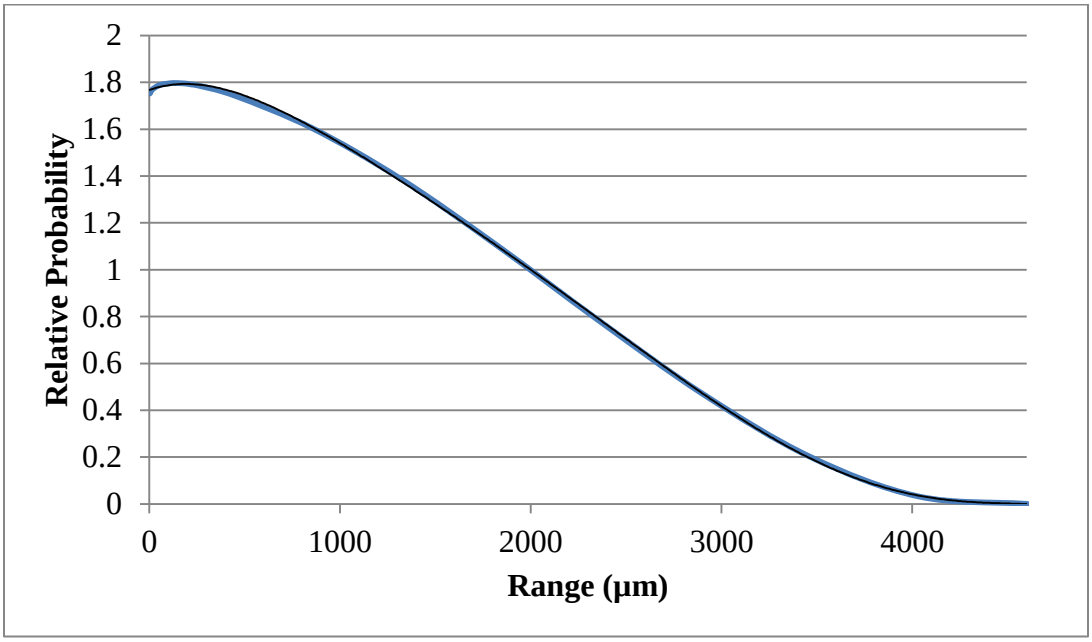

Fig. 4.4: ^{198}Au β Range Distribution and Approximate Polynomial Function

(Eq. 4.5)

$$y = -2.434 * 10^{-21}x^6 + 3.532 * 10^{-17}x^5 - 1.960 * 10^{-13}x^4 + 5.577 * 10^{-10}x^3$$
$$- 9.121 * 10^{-7}x^2 + 2.907 * 10^{-4}x + 1.767$$
$$R^2 = 0.9999$$

A weight function is a mathematical device used when performing a sum, integral, or average to give some elements more influence or "weight" on the result than other elements in the same set. In discrete probability theory, the average value "$\bar{r}$" of discrete variable "r" with associated weight function "$w(r)$" is given by Equation 4.6 below. In the case of continuous functions/variables, the average value "$\bar{r}$" of

continuous variable "r" is given by Equation 4.7. The function "$f(r)$" can be thought of as "what we want to know the average of"; it can be a variable or a function with nested variables.

(Eq. 4.6)

$$\bar{r} = \frac{\sum f(r)w(r)}{\sum w(r)} = \frac{r_1 w_1 + r_2 w_2 + \cdots}{w_1 + w_2 + \cdots}$$

(Eq. 4.7)

$$\bar{r} = \frac{\int f(r)w(r)\,dr}{\int w(r)\,dr}$$

A PDF can be defined as a normalized weight function, shown below in Equation 4.8 where $P(r)$ is the PDF of variable "r". Note that the "area under the curve" for the PDF between the minimum and maximum values of "r" is equal to one. This implies that the probability of the variable "r" attaining a value between its minimum and maximum bounds is 1, or 100%.

(Eq. 4.8)

$$P(r) = \frac{w(r)}{\int_{r_{min}}^{r_{max}} w(r)\,dr}$$

As an example, given a sphere of radius "R", the PDF of the radius inside this sphere can be derived using Equation 4.8. In the context of this problem, "R" could be the radius of a tumor, and "$P(r)$" can be thought of as the probability of finding a nanoparticle a distance "r" away from the center of the tumor.

$$P(r) = \frac{w(r)}{\int_{r_{min}}^{r_{max}} w(r)\, dr}$$

$$w(r) = 4\pi r^2$$

$$P(r) = \frac{4\pi r^2}{\int_0^R 4\pi r^2\, dr} = \frac{3}{R^3} * r^2$$

In probability theory, two variables "a" and "b" are independent if the following identity is true.

$$P(a, b) = P(a)P(b)$$

This identity states that if the probability of a multivariable event $P(a, b)$ whose outcome is "a" and "b" is equal to the product of the probabilities of the two events, $P(a)$ and $P(b)$, then the two variables "a" and "b" are independent. It should be obvious in the context of this problem that the location of the AuNP with respect to the

center of the tumor (expressed by variable "r") and the angle of β emission (expressed by variable "θ") are independent; i.e. the location of the AuNP does not influence the direction of radioactive emission, and vice versa. Since we are assuming that the nanoparticles are distributed in the tumor isotropically with respect to volume, the value of the variable "r" has a non-uniform weight function.

The value of interest, c, is given by the law of cosines (Equation 4.1). Radioactive emissions are released with no preferential solid angle direction, so the weight function for solid angle is therefore unity. Any solid angle direction, Ω, can be expressed in spherical coordinates with the variables "θ" and "φ", which are the polar and azimuthal angles of emission, respectively. The differential solid angle element expressed in terms of "θ" and "φ", however, is given by $d\Omega = \sin(\theta)\,\mathrm{d}\theta\mathrm{d}\varphi$, shown below in Figure 4.5 [83].

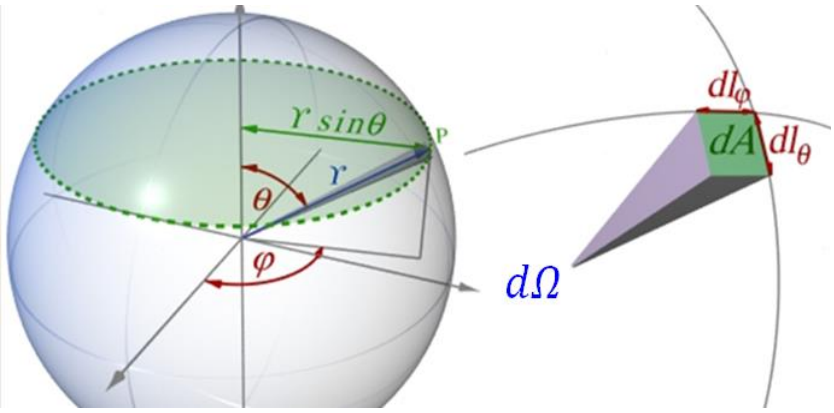

Fig. 4.5: Solid Angle in Spherical Coordinates

If the weight functions for both "θ" and "φ" are equal to "1", then the distribution of emission angles will be incorrectly "bunched" at the poles of the sphere, shown below in Figure 4.6 where the left and right spheres are the top and side views, respectively [84]. Instead, the weight function for the polar coordinate must be set equal to "$\sin(\theta)$", yielding the expected isotropic solid angle distribution in Figure 4.7, where the left and right spheres are the top and side views, respectively [84].

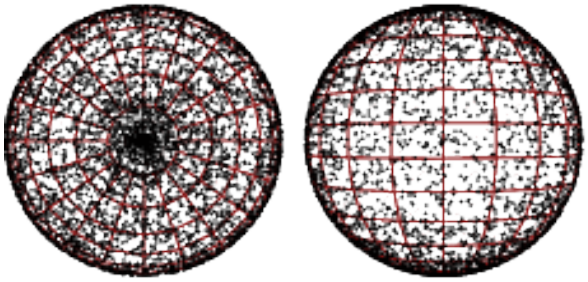

Fig. 4.6: Incorrect Angular Distribution, with $w(\theta) = w(\varphi) = 1$

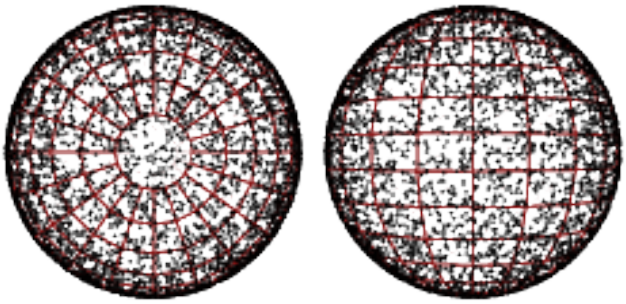

Fig. 4.7: Correct Angular Distribution, with $w(\varphi) = 1,\ w(\theta) = \sin(\theta)$

We can first find the average distance the AuNP is located from the center of the tumor or cell. If the AuNP's location inside the tumor/cell is random and isotropic with respect to volume, then the solution is shown below. This solution should make sense, because the volume of the sphere increases with radius by a factor of r^2, meaning that the answer should be between "$0.5R$" and "R".

$$\bar{r} = \frac{\int f(r)w(r)\,dr}{\int w(r)\,dr}$$

$$f(r) = r$$

$$w(r) = \pi r^2$$

$$\bar{r} = \frac{\int_0^R (r)(\pi r^2)\,dr}{\int_0^R (\pi r^2)\,dr}$$

$$\bar{r} = 0.75R$$

There is no simple "plug in and plot" method to produce the PDF of c with respect to c since it is a dependent variable. In other words, $P(c)$ is a "function of two multivariable functions". One could derive $P(c)$ rigorously by executing a transformation of variables (which would probably be necessary for complicated

probability distributions associated with pharmacokinetics), but we can simplify things in this example by exploiting the symmetry of the sphere with particles located isotropically inside of it [85, 86]. In general, $P(c)$ is defined as the probability distribution of distances the β particle must travel through cancerous tissue before reaching surrounding tissue. Specifically for this problem, we can define the following:

$$P(c)dc = [\text{Volume such that the distance to the surface in the (upward)} \uparrow \text{ direction is between "c" and "c + dc"}]/\left(\frac{4}{3}\pi R^3\right)$$

This volume can be expressed by the equation below, and is illustrated in Figure 4.8. In this case, the differential height "dh" is simply "dc".

$$Vol = \int_0^r 2\pi r dr \int_{h_{min}}^{h_{max}} dh$$

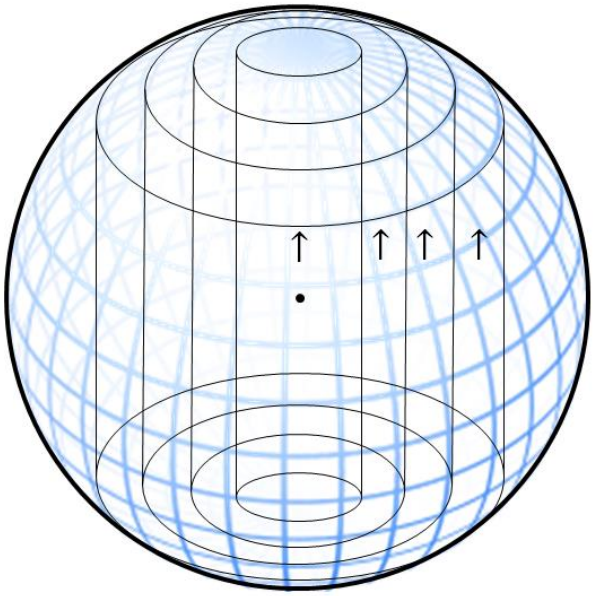

Fig. 4.8: Spherical Volume such that the Distance to the Surface in the Upward Direction is between "c" and "dc"

In order to perform a change of variables, we must now express the radial component in terms of "c". Since the maximum value "c" can attain is the diameter of the sphere (or "$2R$"), and due to the symmetry of the geometry, we can split the sphere into top and bottom halves, each with heights "$c/2$" (shown below in Figure 4.9). This allows us to express "r" in terms of "c" by using the Pythagorean Theorem. Integrating below, the distribution $P(c)$ becomes Equation 4.9 shown below.

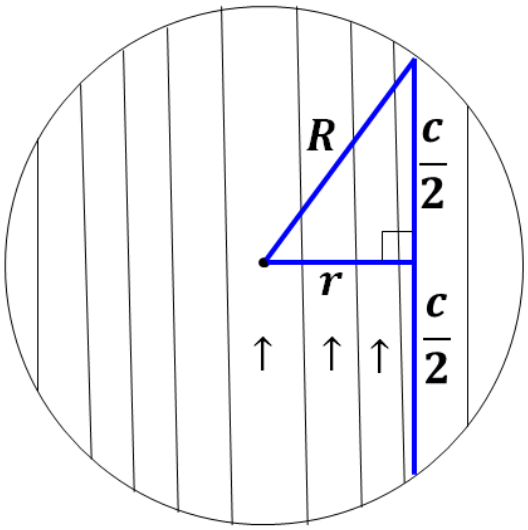

Fig. 4.9: Change of Variables from "r" to "c" for Particle Isotropy and Spherical Symmetry

$$P(c) = \frac{\int_0^{"r"} 2\pi r dr}{\frac{4}{3}\pi r^3}$$

$$P(c) = \frac{\int_0^{\sqrt{R^2-\left(\frac{c}{2}\right)^2}} 2\pi r dr}{\frac{4}{3}\pi r^3}$$

(Eq. 4.9)

$$P(c) = \left(\frac{3}{2}\right)\left(\frac{1}{2R}\right)\left[1-\left(\frac{c}{2R}\right)^2\right]$$

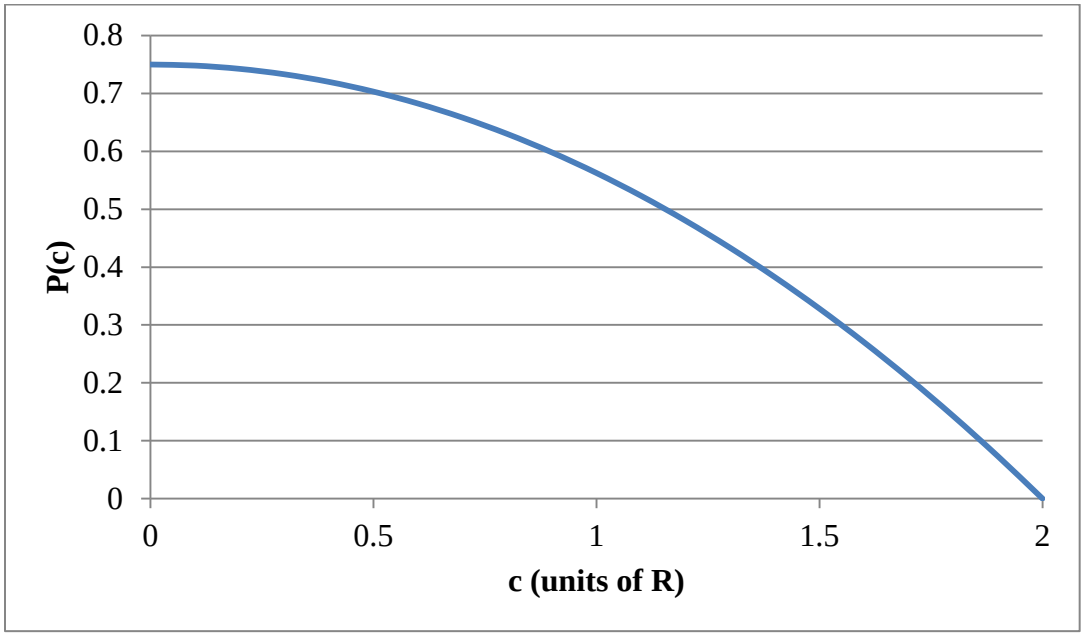

Fig. 4.10: $P(c)$ vs. c for Particle Isotropy in a Sphere

Figure 4.10 above is the PDF of c. One can immediately identify that the average distance the β emissions must travel through the tumor is less than the radius of the tumor; in other words, the average value of c should be between "0" and "R". The true average value of c is calculated below. Note that $P(c)$ is already normalized (because it is a PDF), so the denominator is unity.

$$\bar{c} = \frac{\int f(c)w(c)dc}{\int w(c)dc} = \int f(c)w(c)dc$$

$$\bar{c} = \int_0^{2R} (c)\left(\frac{3}{2}\right)\left(\frac{1}{2R}\right)\left[1 - \left(\frac{c}{2R}\right)^2\right]dc = \frac{3}{4}R$$

We can verify that the PDF for Figure 4.10 is correct by utilizing the multivariable weight functions (Equation 4.5) for "r", "θ", and "φ", and by expressing "c" in terms these variables by using Equation 4.1, shown below.

$$\bar{c} = \frac{\int\int\int f(r,\theta,\varphi)w(r,\theta,\varphi)\,drd\theta d\varphi}{\int\int\int w(r,\theta,\varphi)\,drd\theta d\varphi}$$

$$f(r,\theta,\varphi) = \sqrt{R^2 - r^2\sin^2(\theta)} - r\cos(\theta)$$

$$w(r,\theta,\varphi) = w(r)w(\theta)w(\varphi)$$

$$w(r) = 4\pi r^2$$

$$w(\theta) = \sin(\theta)$$

$$w(\varphi) = 1$$

$$\bar{c} = \frac{\int_0^{2\pi}\int_0^{\pi}\int_0^{R}\left[\sqrt{R^2 - r^2\sin^2(\theta)} - r\cos(\theta)\right](\pi r^2)(\sin\theta)drd\theta d\varphi}{\int_0^{2\pi}\int_0^{\pi}\int_0^{R}(\pi r^2)(\sin\theta)drd\theta d\varphi}$$

$$\bar{c} = \frac{3}{4}R$$

The value of $\bar{c}$ is again $0.75R$. We now have everything required to determine the average amount of energy deposited to tumor tissue, which, in turn, can be used to directly calculate the energy to healthy tissue. We can use Equation 4.10 below to calculate energy to tumor vs. energy to healthy surrounding tissue ratios, where $\overline{E_\beta}$ is the total average amount of energy the β will deposit to human tissue (both cancerous and healthy), $\bar{E}_t$ is the average amount of energy the β will deposit only to cancerous tissue, and $\overline{E_h}$ is the average amount of energy the β will deposit only to surrounding healthy tissue.

$$\overline{E_{tot}} = \overline{E_\beta} = 311.4\ keV$$

$$\overline{E_\beta} = \overline{E_h} + \bar{E}_t \qquad \text{(Eq. 4.10)}$$

The energy deposited to tumor tissue is a function of (a) how far the β must travel through the tumor tissue before reaching healthy tissue (denoted by "c"), and (b) how far the β will travel before coming to rest (which will henceforth be denoted by "b"). By solving for the average energy deposited into surrounding healthy tissue and knowing that the average β will deposit $311.4\ keV$ of energy in total, Equation 4.10 will allow us to calculate the ratio of energy to cancerous tissue vs. total energy to surrounding healthy tissue; ideally this ratio should be as close to 1 as possible, meaning that all of the dose to the patient is deposited to cancerous tissue.

Recall integrating Equation 4.3 relates the β particle's range through human tissue to the energy it will lose slowing down through it. If we were to ask the question, "how much energy does a β emission deposit to human tissue that travels 906 μm before coming to rest", we would integrate Equation 4.3 using the lower and upper bounds of 0 μm to 906 μm, shown below.

$$E(R_\beta) = -0.367 + \int_0^{906} 3.33(R_\beta + 0.007)^{-0.435} + 0.0055{R_\beta}^{0.33}\, dR_\beta \approx 311.4\ keV$$

However, we now ask the question, "if the β first must travel through 850 μm of cancerous tissue before it reaches the healthy tissue, how much energy will the β deposit to healthy tissue as it comes to rest in this case?"; the same procedure is followed, only this time it travels 906-850=56 μm through healthy tissue.

$$E(R_\beta) = -0.367 + \int_0^{56} 3.33(R_\beta + 0.007)^{-0.435} + 0.0055{R_\beta}^{0.33}\, dR_\beta \approx 57.9\ keV$$

The general formula for the energy deposited to surrounding healthy tissue is equal to Equation 4.11 below, where "c" is the distance the β must travel through cancerous tissue to reach surrounding healthy tissue, and "b" is the total range of the β emission.

(Eq. 4.11)

$$E(b,c) = -0.367 + \int_0^{b-c} 3.33\left(R_\beta + 0.007\right)^{-0.435} + 0.0055{R_\beta}^{0.33}\, dR_\beta$$

We can use Equation 4.9 to calculate the average energy to the surrounding healthy tissue, "$\overline{E_h}$", as follows.

$$\overline{E_h} = \frac{\int_{c_{min}}^{c_{max}} \int_{b_{min}}^{b_{max}} f(b,c)w(b)w(c)\, dbdc}{\int_{c_{min}}^{c_{max}} \int_{b_{min}}^{b_{max}} w(b)w(c)\, dR_\beta dbdc}$$

$$f(b,c) = -0.367 + \int_0^{b-c} 3.33\left(R_\beta + 0.007\right)^{-0.435} + 0.0055{R_\beta}^{0.33}\, dR_\beta$$

The weight functions in this case are PDFs, which are normalized, so the denominator in the above equation is unity. For ^{198}Au, the β emission can only travel up to 4505 μm through unit-density tissue (the upper bound), and since we are looking at only the energy deposited to cancerous tissue, its lower bound must be "c". The maximum value for "c" through the sphere is its diameter. If the tumor diameter is smaller than the maximum β path length (4505 μm in the case of ^{198}Au), the equation can be rewritten as shown below. Figure 4.11 illustrates the associated geometry. The weight functions

$w(b)$ and $w(c)$ are the usual PDFs of range and tumor path length from Figure 4.4 and Equation 4.9, respectively.

$$\overline{E_h} = \int_0^{2R} \int_c^{4505} f(b,c)w(b)w(c)\,dbdc$$

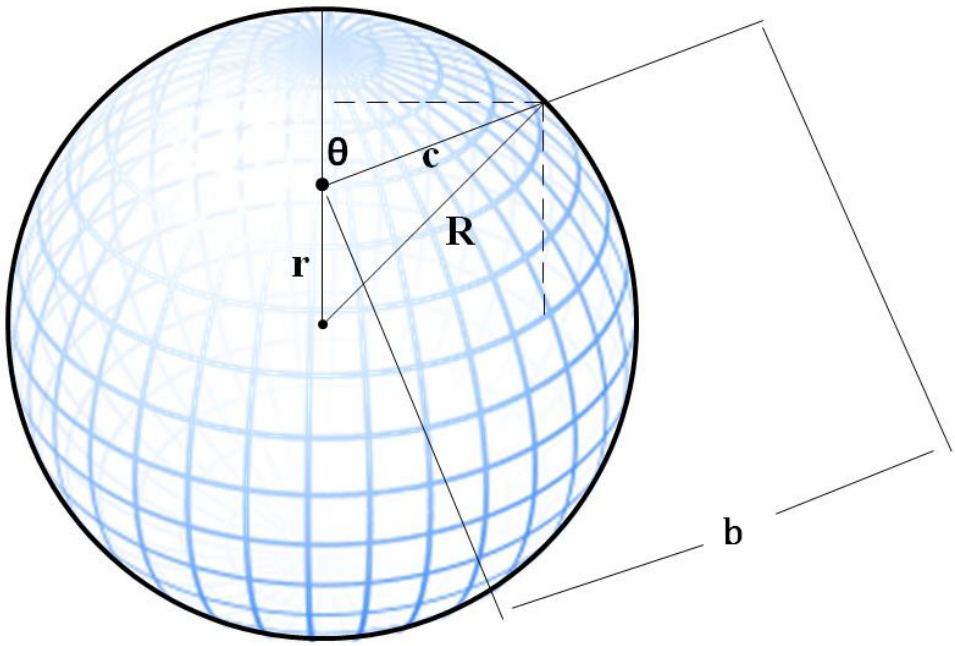

Fig. 4.11: Illustration of β Path through Tissue

If the tumor diameter is larger than the maximum β path length, then some of the emissions will inevitably deposit 100% of their energy into the tumor. This can be accounted for by calculation the proportion of path lengths which are larger than the

maximum β path length. This value will henceforth be defined as the factor "g", shown below in Equation 4.12.

$$g = \int_{4505}^{2R} \left(\frac{3}{2}\right)\left(\frac{1}{2R}\right)\left[1 - \left(\frac{c}{2R}\right)^2\right] dc \qquad \text{(Eq. 4.12)}$$

In the case of a tumor whose diameter is larger than the maximum β path length, the average energy deposited to healthy surrounding tissue is:

$$\overline{E_h} = (1-g) \int_0^{4505} \int_c^{4505} f(b,c) * P(b) * P(c)\, dbdc$$

The general formula for energy deposited to healthy tissue surrounding a tumor or cancer cell is given by Equation 4.13. For the case of the radionuclide ^{198}Au, the maximum β range "b_{max}" through unit-density tissue is 4505 μm.

(Eq. 4.13)

$$\overline{E_h}(b,c) = \begin{cases} \int_0^{2R} \int_c^{b_{max}} f(b,c) * P(b) * P(c)\, dbdc, & R \le b_{max} \\ (1-g) \int_0^{b_{max}} \int_c^{b_{max}} f(b,c) * P(b) * P(c)\, dbdc, & R > b_{max} \end{cases}$$

The SI unit of dose in radiation dosimetry is the Gray (Gy), which is equal to 1 joule per kilogram of tissue. Equation 4.13 must therefore be converted from keV to joules. Assuming the density "ρ" of tissue is constant (which may not be the case if, for example, cancerous tissue is located in or near bones or other densifications), the mass of a tumor is given by:

$$m_{tumor} = \frac{4}{3}\pi R^3 \rho$$

The mass of the surrounding healthy tissue is equal to the shell of healthy tissue surrounding the tumor multiplied by tumor density, whose outer radius is equal to the maximum β travel length, given by Equation 4.14 below. These tissue geometries are illustrated below in Figure 4.12, where the red line is the radius of the tumor "R" and the green line is the maximum β travel length "b_{max}".

$$m_{healthy} = \frac{4}{3}\pi[(b_{max} + R)^3 - R^3]\rho \qquad \text{(Eq. 4.14)}$$

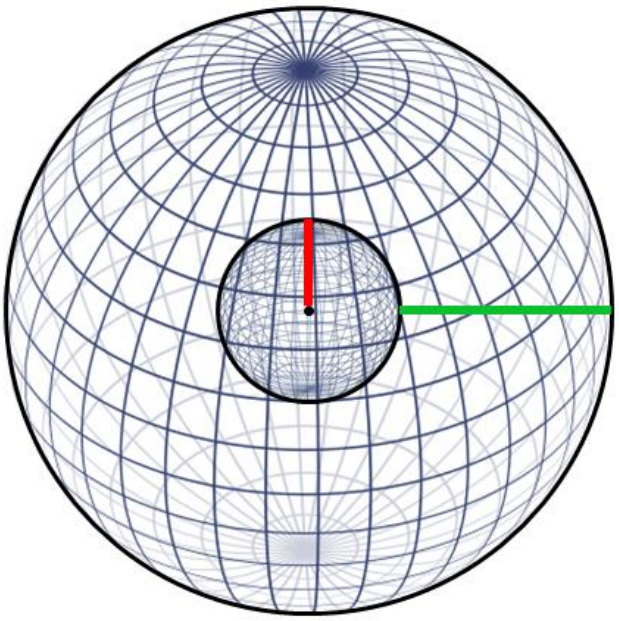

Fig. 4.12: Illustration of Tumor and Surrounding Healthy Tissue

Combining Equation 4.13 with Equation 4.14 yields Equation 4.15, the average dose deposited to healthy tissue surrounding cancerous tissue per decay.

$$\overline{E_h}\left[\frac{keV}{kg}\right] = \begin{cases} \dfrac{\int_0^{2R}\int_c^{b_{max}} f(b,c) * P(b) * P(c)\, dbdc}{\frac{4}{3}\pi[(b_{max}+R)^3 - R^3]\rho}, & R \le b_{max} \\ \dfrac{(1-g)\int_0^{b_{max}}\int_c^{b_{max}} f(b,c) * P(b) * P(c)\, dbdc}{\frac{4}{3}\pi[(b_{max}+R)^3 - R^3]\rho}, & R > b_{max} \end{cases}$$

(Eq. 4.15)

$$\overline{E_h}[Gy] = \begin{cases} (1.602 * 10^{-16})\dfrac{\int_0^{2R}\int_c^{b_{max}} f(b,c) * P(b) * P(c)\, dbdc}{\frac{4}{3}\pi[(b_{max}+R)^3 - R^3]\rho}, & R \le b_{max} \\ (1.602 * 10^{-16})\dfrac{(1-g)\int_0^{b_{max}}\int_c^{b_{max}} f(b,c) * P(b) * P(c)\, dbdc}{\frac{4}{3}\pi[(b_{max}+R)^3 - R^3]\rho}, & R > b_{max} \end{cases}$$

Table 4.1 below shows the variability of these distribution functions for different sized tumors, including leukemia cells whose average radius is assumed to be 7.5 μm [87]. In Table 4.1, $D_{Healthy}$, D_{Tumor}, and D_{Total} are the doses to healthy tissue, tumor tissue, and total to all tissue, respectively. Tumors A, B, C, and D are spherical tumors with radii of 50 μm, 0.5 mm, 5 mm, and 2.5 cm, respectively.

Table 4.1: Energy Deposition and Dosimetry Ratios of Cancerous vs. Surrounding Healthy Tissue Subject to Nano-TRT

Tumor I.D.	Radius	Avg. E_{tumor} (keV)	Avg. $E_{healthy}$ (keV)	$\frac{D_{tumor}}{D_{total}}$
Leukemia	7.5 μm	11.2	300.2	0.9999988
A	50 μm	34.4	277	0.99989
B	0.5 mm	126.4	185	0.9985
C	5 mm	290.5	20.9	0.988
D	2.5 cm	303.8	7.6	0.961

4.2 Dose as a Function of Radius

Table 4.1 yields a logical result when considering energy deposited to tumors of varying radius: the larger the tumor, the more average energy deposited to the tumor. The average dose to the tumor, however, decreases as the tumor size increases. Though this may seem counterintuitive, it is true since the proportion of healthy/cancerous mass

is smaller for smaller tumors, and dose deposited to tissue is not linear with respect to tumor radius.

Tumors B (left) and D (right) are illustrated below in Figure 4.13. Again, the red line is the tumor radius, and the green like is the maximum β travel length denoting exposed healthy tissue; i.e. the green lines are the same length in both cases. Note that mass of healthy tissue is much larger than the mass of cancerous tissue in Tumor B, but is much smaller in Tumor D. Dose is defined as energy deposited per unit mass, and smaller tumors are associated with a proportionally larger mass of surrounding healthy tissue.

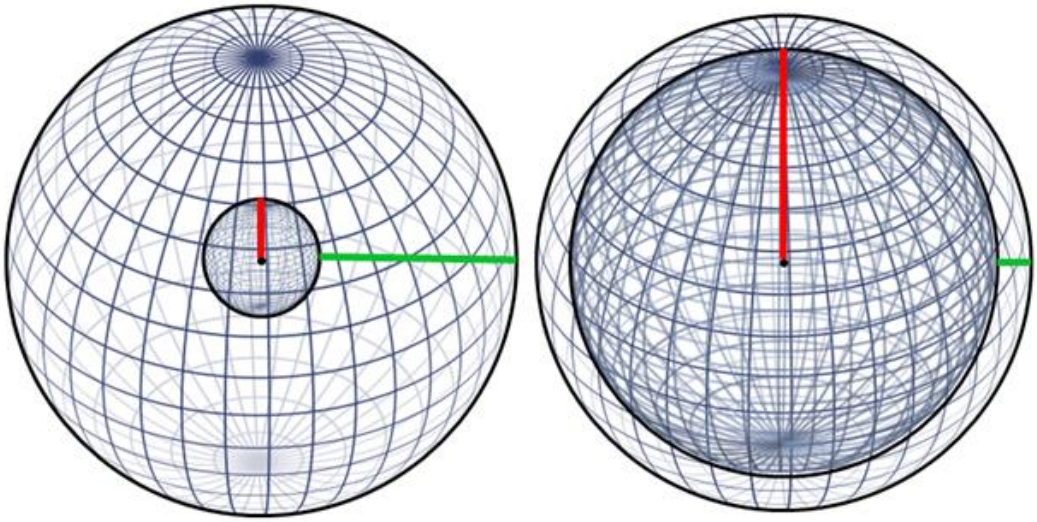

Fig. 4.13: Tumors B (left) and D (right) with Exposed Healthy Surrounding Tissue

To better understand nano-TRT dose vs. tumor size, consider a tumor that is much larger than the maximum β travel length, such as Tumor D from Table 4.1 (radius

of 2.5 cm). This tumor can be illustrated by Figure 4.14 below. Each colored circle has a radioactive nanoparticle at its center, and the average β emission will reach the edge of its colored region. This means that half of the decays will reach beyond its own colored region (i.e. emissions from the green center circle might leak into the red region). Emissions which originate in the green, blue, and red circles cannot reach surrounding healthy tissue; however, emissions which originate in the yellow circles can reach healthy tissue.

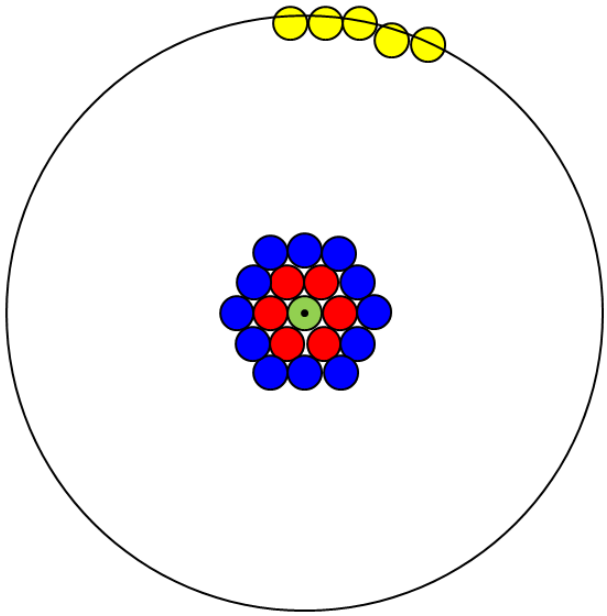

Figure 4.14: Illustration of Tumor D Dose vs. Radius

Emissions which occur in the green, red, or blue region can be thought of as being in an infinite medium of cancerous tissue which is populated with isotropically distributed radioactive nanoparticles because no boundary is within the range of the β.

In this case, the dose with respect to distance is constant because each point is receiving even contributions of exposure from all directions. In other words, if the PDF of finding nanoparticles a distance "r" from the center of the tumor is given by $P(r)$, and the mass with respect to tumor radius is given by "$m(r)$", then the dose as a function of radius for the center or "bulk" of a large tumor (i.e. green, red, and blue regions) is constant, shown below.

$$P(r) \propto r^2$$

$$m(r) \propto r^2$$

$$D(r_{bulk}) \propto \frac{P(r)}{m(r)} \propto 1$$

However, radial positions close to the cancer/healthy tissue boundary (i.e. yellow circles) will receive exposure from the radially inward direction (cancerous tissue), but receive no exposure from the radially outward direction (healthy tissue) because there are no radioactive nanoparticles bound to healthy tissue. The rate at which dose to the tumor decreases near the cancer/healthy tissue boundary for a point source is proportional to r^{-2} multiplied by a "boundary effects term", $f_B(r)$. This boundary effects term accounts for the fact that β emissions start with a distribution of energies, they have a non-uniform stopping power (see Equation 4.3), and pharmacokinetic non-uniformity

which may be specific to the tumor of interest. To summarize, the dose to cancerous tissue as a function of radial position for a point source is given by Equation 4.16 below.

$$D(r) \propto \begin{cases} 1, & 0 < r < (R - b_{max}) \\ \frac{1}{r^2} * f_B(r), & (R - b_{max}) < r < R \end{cases} \quad \text{(Eq. 4.16)}$$

To better understand the implications of these dose distributions, let's look at two different sized tumors which both have uniform nanoparticle distributions. To make the math easier, we have approximated the boundary effects function to be constant (which would require all particles to be emitted at the same energy and stopping power to be constant). The tumor radii (R) with respect to the particles' range (b) are chosen arbitrarily as follows.

Larger Tumor: $b = 0.1R$

Smaller Tumor: $b = R$

The dose as a function of radius is these situations is given in Figure 4.15 for the larger tumor and Figure 4.16 for the smaller tumor.

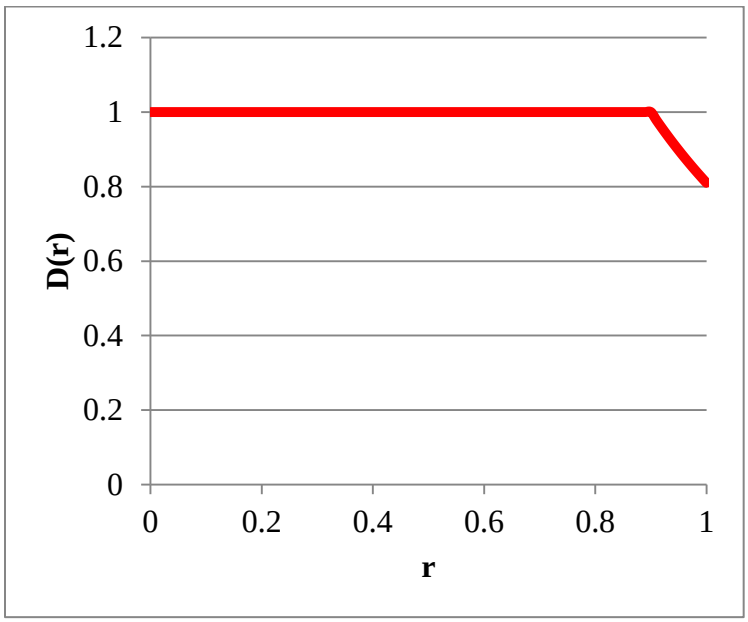

Fig. 4.15: Approximate Dose to Cancerous Tissue vs. Radial Position, $b = 0.1R$

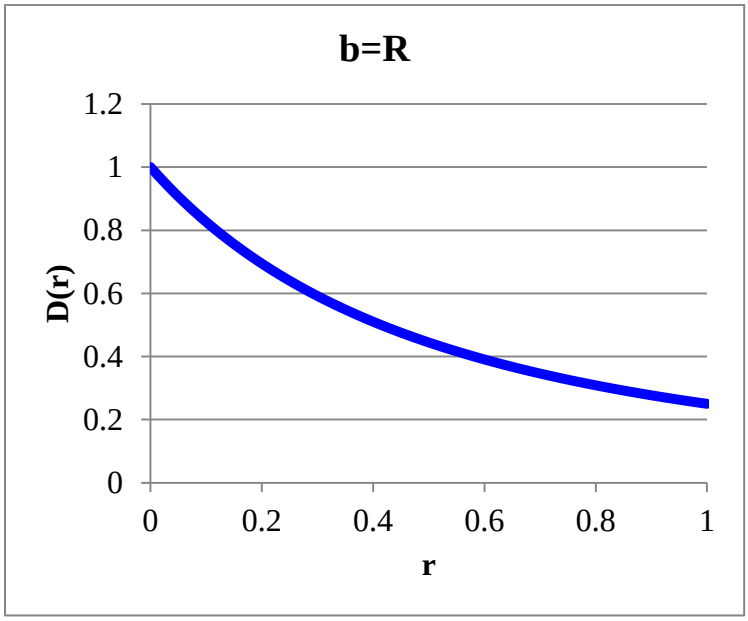

Fig. 4.16: Approximate Dose to Cancerous Tissue vs. Radial Position, $b = R$

Figures 4.15 and 4.16 suggest that treating a patient based on an "average tumor dose" may not be appropriate for treating tumors. The average dose may be noticeably higher than the dose deposited to the outer rim of the tumor in some cases.

4.3 Generic Case Study: 1 cm Diameter Tumor

XRT inevitably subjects healthy tissue to radiative assault since the beam must first travel through healthy tissue to reach the cancerous tissue [88]. The appropriate dose for primary tumors using XRT is generally less than 100 Gy, while an acceptable dose level to tissue outside the tumor is between 5-50 Gy [89]. Some areas of the body are more sensitive to radiation than others; for tumors near the pelvic region, for example, risk of major complications increases at doses above 40 Gy (at 2 Gy per fraction) [90]. XRT fractionation means that the total dose is spread out over several small treatments. The lethal potential of radiation is not only a function of dose, but how long it takes to deliver the dose [91-94].

If we intend to treat a 1 cm diameter tumor with an average dose of 40 Gy (as done currently in practice) using nano-TRT, we need to know the dose deposited to surrounding healthy tissue, the total number of AuNPs used, the ^{198}Au distribution among the AuNPs, and the activation time required to produce this distribution. The first step is to determine how much dose the surrounding healthy tissue receives for this treatment (which was derived in chapter 4.1). According to Table 4.1, a 1 cm diameter tumor receives 98.8% of the total dose using nano-TRT (Tumor C), assuming a uniform nanoparticle distribution. Therefore, if the tumor is to receive an average dose of 40 Gy,

the total average dose must be 40.48 Gy. The healthy tissue surrounding this tumor will receive an average dose of only 0.48 Gy.

Assuming a tissue density of 1 g cm^{-3}, the mass of surrounding tissue is approximately $3.07*10^{-3}$ kg, and the average energy deposited to the healthy tissue per decay is about 20.9 keV, or about $3.35*10^{-15}$ J. Given the mass and dose, the total energy can be calculated; if the surrounding healthy tissue has a mass of $3.07*10^{-3}$ kg and will receive a dose of 0.48 Gy, a total energy of $1.474*10^{-3}$ J is required. Dividing the total required energy by the average amount of energy deposited per decay yields the number of decays required to deposit this dose, which in this case is $(1.474 * 10^{-3}\ J)/(3.35 * 10^{-15}\ J/decay) = 4.4 * 10^{11}$ decays. Again assuming that the drug has a residence time of about 3 weeks, we can calculate the necessary initial number of ^{198}Au atoms we need to produce by noticing that 3 weeks is over ten times longer than the radioactive half-life of ^{198}Au (2.69 days). This allows us to approximate that all $4.4 * 10^{11}$ radioactive atoms will have decayed within the 3 week residence time.

Assuming a 50 nm diameter AuNP (to maximize receptor-mediated nanomaterial endocytosis discussed in Chapter 3), we can now choose how many radioactive atoms per nanoparticle we wish to have (on average), which will yield the number of AuNPs in total. We have arbitrarily chosen an average of 22 radioactive atoms per AuNP, which will require $2*10^{10}$ AuNPs. Using Poisson statistics from Chapter 2.5, the distribution of ^{198}Au per 50 nm diameter AuNP is shown below in Figure 4.17. Based on neutron activation analysis (Chapter 2.3), an activation time of 1.2 hours is required to produce these nanoparticles in the TAMU NSC nuclear reactor.

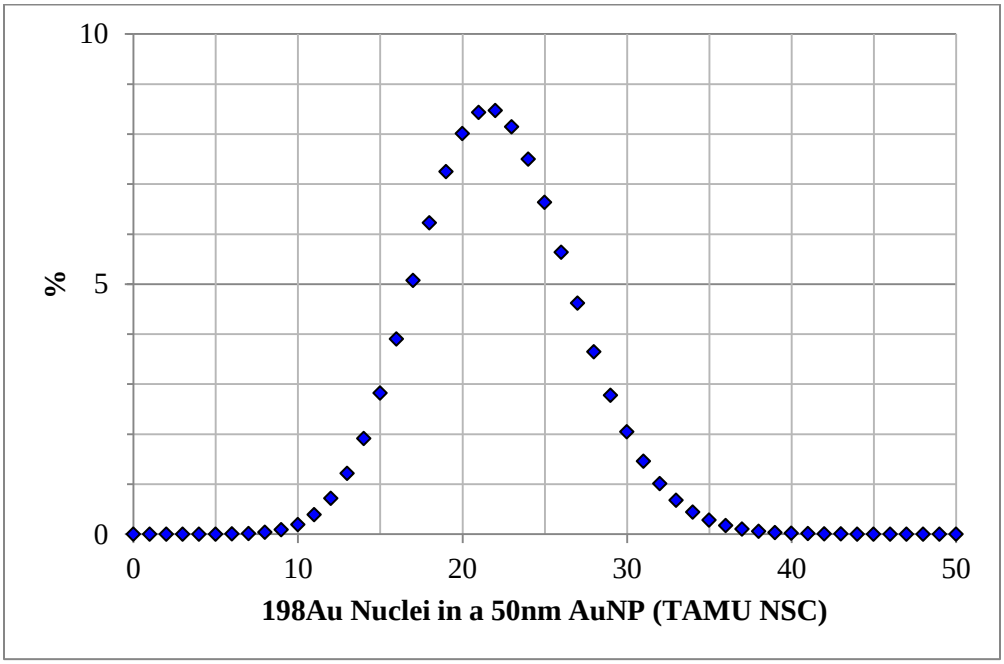

Fig. 4.17: Distribution of ^{198}Au Nuclei per 50 nm AuNP for General Case Study

5. FUTURE WORK

Two primary avenues for future work are necessary for the continuation of this research: (1) the production of radioactive gold nanoparticles must be optimized, and (2) time-dependent quantification of the pharmacokinetics of conjugated nanoparticles must be quantified defined.

The AuNP activation procedures must be optimized to minimize surfactant failure and AuNP agglomeration. It is possible to activate 100 nm AuNPs by irradiating the samples at full reactor power for one hour or less using the TAMU NSC reactor. It may be possible to further reduce γ exposure to the surfactant by surrounding the sample with a lead shield.

A promising alternative to the procedures above is to use the TAMU NSC reactor to activate small pure gold foils, then dissolve the radioactive foils and synthesize AuNPs in a radiochemistry laboratory [95]. Alternatively, solution samples of $HAuCl_4$ could be activated, and then radioactive AuNPs could be directly synthesized and coated with a citrate stabilizing agent. Since the nanoparticles are synthesized after neutron activation in this manner, the high temperature/radiative fluence environment inside the nuclear reactor cannot compromise the surfactant and is of no concern. Furthermore, the gold can be activated much closer to saturation without agglomeration concerns. The synthesis of radioactive citrate-stabilized nanoparticles can be carried out by chemical means in a radiochemistry laboratory as follows. Add 20 mL of 1.0 mM $HAuCl_4$ to a 50 mL beaker or Erlenmeyer flask on a stirring hot plate. Use a magnetic

bar to stir the solution and bring the solution to a boil. Add 2 mL of a 1% solution of trisodium citrate dihydrate ($Na_3C_6H_5O_7 \cdot 2H_2O$) to the boiling/stirring solution. The gold sol gradually forms as the citrate reduces the gold (III). Remove from heat when the solution has turned deep red or 10 minutes has elapsed.

Each method of producing radioactive gold nanoparticles has respective costs and benefits. Purchasing the nanoparticles from a vendor and activating them in a nuclear reactor is inherently simpler and less time-consuming as the nanoparticles are already formed, and the cost is cheaper due to the cost of reagents used to synthesize large quantities of gold nanoparticles. However, avoiding surfactant failure due to the high temperatures and high radiative fluence found inside the NSC reactor is a major benefit of synthesizing the nanoparticles after neutron activation. Funding and time were key factors when deciding which approach to take for this project, so we decided to purchase the nanoparticles from a vendor.

One additional possibility for the production of large samples of radioactive AuNPs is to solicit the use of a higher flux nuclear reactor. The Missouri University Research Reactor (MURR), for example, has a thermal neutron flux of $6x10^{14}$ n s^{-1} cm^{-2} (compared to the NSC's 10^{13} n s^{-1} cm^{-2}). Furthermore, the MURR operates at a T_{hot} of 58 °C (compared to the NSC's 80 °C).

When using a nuclear reactor with a higher flux such as MURR and activating for only 10 minutes (allowing 24 hours of decay to ship across state lines back to our lab), Figure 5.1 below represents the Poisson distribution which estimates the discrete

probability distribution of radioactive atoms (^{198}Au) per 100 nm nanoparticle, followed by the dose to cancerous tissue in Figure 5.2.

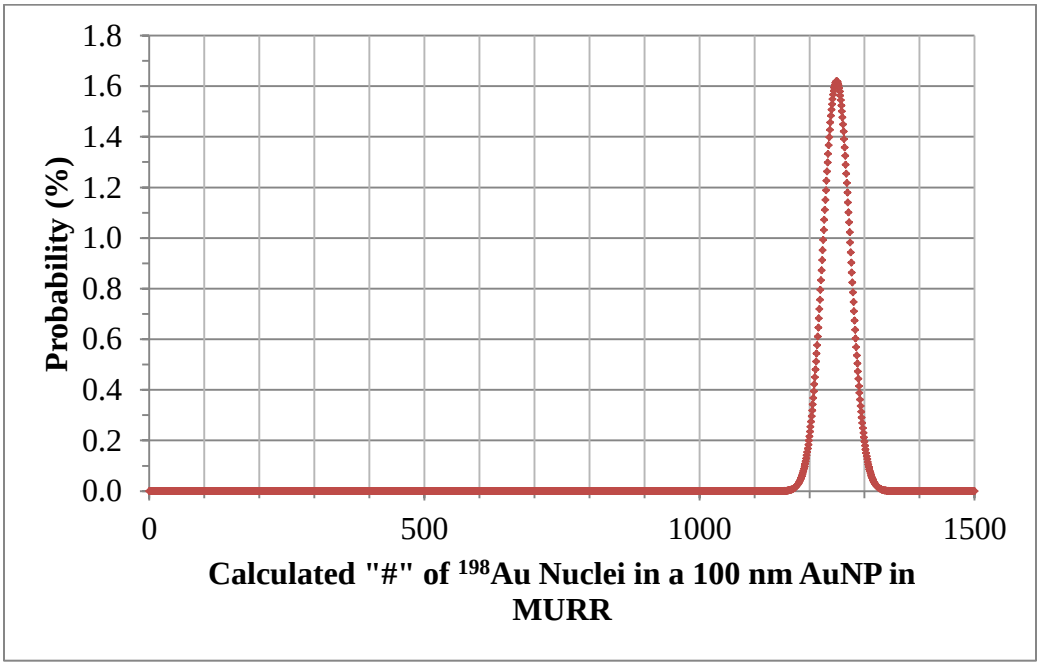

Fig. 5.1: Discrete Poisson Distribution of Calculated ^{198}Au Nuclei per 100 nm Diameter AuNP Given t_{irr} = 10 min, and t_d = 24 h in the MURR

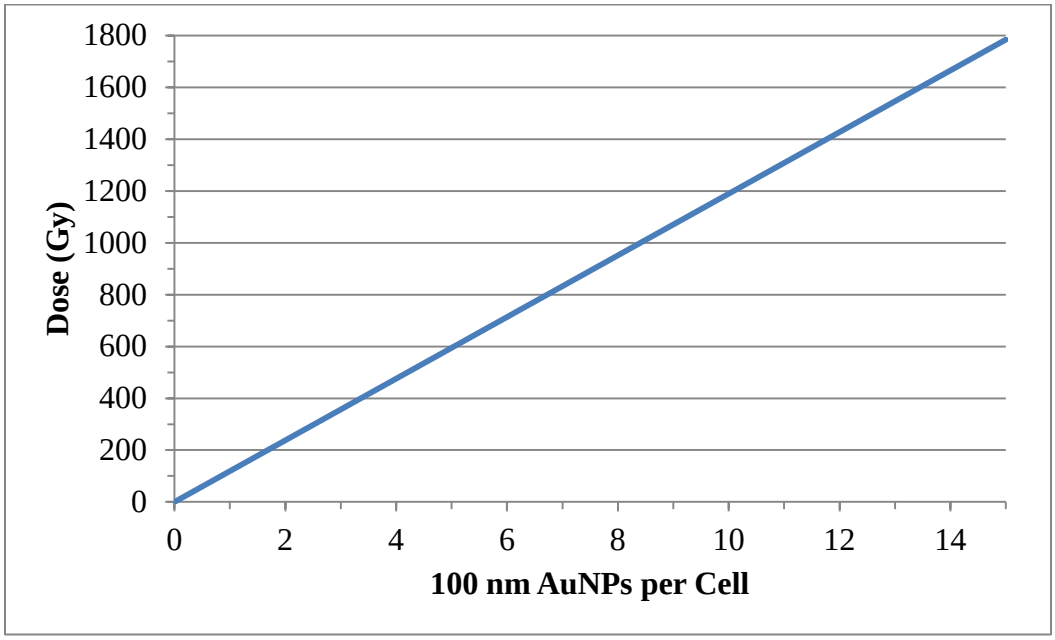

Fig. 5.2: Calculated Dose (Gy) from Primary β^- Emission of MURR-Activated 100 nm AuNPs vs. 100 nm AuNPs per Cell, Given t_{irr} = 10 min, and t_d = 24 h, Assuming Infinite AuNP Residence Time Approximation

6. SUMMARY

Controllable mechanisms of surfactant failure include (1) the high temperature environment, and (2) the high-fluence bombardment of high energy γ-radiation. The effects resulting from these conditions may be ameliorated by using a lower temperature nuclear reactor, by employing lead shielding around the sample, or by reducing activation time. Though neutrons and γ rays inevitably interact with and damage surfactant nuclei, we successfully activated AuNPs without causing surfactant failure by using larger 100 nm diameter AuNPs, which have a lower surface energy and are composed of many more nuclei compared to 10 nm and 17 nm AuNPs.

The larger nanoparticles required significantly less activation time than the smaller nanoparticles (1 hour down from at least 6 hours) to meet the criterion of having at least 1 radioactive atom per nanoparticle even after several hours of decay. The 100 nm AuNP surfactant appeared to survive the 1 hour neutron activation in the TAMU NSC nuclear reactor to the naked eye; however, further characterization could not be executed due to project cancellation.

We provided a method to calculate the number of radioactive atoms per nanoparticle using the Poisson distribution. By using the xCELLigence system, we demonstrated a method of comparing nano-enhanced TRT with other treatments as a function of time, though these experiments were not carried out. The derivation of the efficacy of nano-TRT includes dose distributions to cancerous vs. surrounding healthy tissue when using nano-TRT. If pharmacokinetic probability distributions are available, the general formula for dose to cancerous vs. healthy surrounding tissue (Eq. 4.15) is applicable to any size tumor and any radionuclide.

REFERENCES

1. Institute, N.C. *SEER Stat Fact Sheets: All Sites*. Surveillance Epidemiology and End Results 2012 [cited 2012 Aug. 18]; Available from: http://seer.cancer.gov/statfacts/html/all.html.
2. Laboratory, L.L.N. *An Inside Attack on Cancer*. Science & Technology 2003 [cited 2012 Aug. 18]; Available from: https://www.llnl.gov/str/JulAug03/Hartmann-Siantar.html.
3. Zola, H., Bernadette Swart, Alison Banham, Simon Barry, Alice Beare, Armand Bensussan, Laurence Boumsell, Chris D. Buckley, Hans-Jorg Buhring, Georgina Clark, Pablo Engel, David Fox, Bo-Quan Jin, Peter J. Macardle, Fabio Malavasi, David Mason, *CD Molecules 2006 - Human Cell Differentiation Molecules.* Journal of Immunological Methods, 2007. **319**: p. 1-5.
4. Humm, J.L., *Dosimetric Aspects of Radiolabeled Antibodies for Tumor Therapy.* Journal of Nuclear Medicine, 1986. **27**(9): p. 1490-1497.
5. O'donoghue, J.A., M. Bardies, and T.E. Wheldon, *Relationships between Tumor Size and Curability for Uniformly Targeted Therapy with Beta-Emitting Radionuclides.* The Journal of Nuclear Medicine, 1995. **36**(10): p. 1902-1909.
6. Jacene, H.A., R. Filice, W. Kasecamp, and R.L. Wahl, *Comparison of 90Y-Ibritumomab Tiuxetan and 131I-Totitumomab in Clinical Practice.* Journal of Nuclear Medicine, 2007. **48**(11): p. 1767-1776.

7. Carter, P., *Improving the Efficacy of Antibody-Based Cancer Therapies.* Nature Review: Cancer, 2001. **1**: p. 118-129.

8. Sumer, B. and J.M. Gao, *Theranostic Nanomedicine for Cancer*. Nanomedicine, 2008. **3**(2): p. 137-140.

9. Technologies, F.P. *P/N Junctions & Band Gaps*. Solar Cell Central 2011 [cited 2012 Aug. 18]; Available from: http://solarcellcentral.com/junction_page.html.

10. Taton, A., Gang Lu, and Chad Mirkin, *Two-Color Labeling of Oligonucleotide Arrays via Size-Selective Scattering of Nanoparticle Probes.* The Journal of the American Chemical Society, 2001. **123**: p. 5164-5165.

11. Anker, J.N., et al., *Biosensing with Plasmonic Nanosensors.* Nature Materials, 2008. **7**(6): p. 442-453.

12. Wang, J.T., et al., *FRET-Like Fluorophore-Nanoparticle Complex for Highly Specific Cancer Localization.* Oxygen Transport to Tissue Xxxi, 2010. **662**: p. 407-413.

13. Ray, P., Gopala Darbha, Anandhi Ray, Joshua Walker, and William Hardy, *Gold Nanoparticle Based FRET for DNA Detection.* Plasmonics, 2007. **2**: p. 173-183.

14. Sun, Y., et al., *FRET Microscopy in 2010: The Legacy of Theodor Forster on the 100th Anniversary of his Birth.* Chemphyschem, 2011. **12**(3): p. 462-74.

15. Sanju, K.S., P.P. Neelakandan, and D. Ramaiah, *DNA-Assisted White Light Emission through FRET.* Chem Commun (Camb), 2011. **47**(4): p. 1288-90.

16. Loura, L.M. and M. Prieto, *FRET in Membrane Biophysics: An Overview.* Front Physiol, 2011. **2**: p. 82.

17. Wang, J., et al., *FRET-Like Fluorophore-Nanoparticle Complex for Highly Specific Cancer Localization.* Oxygen Transport to Tissue Xxxi, 2010. **662**: p. 407-13.

18. Perez, M., Lee Josephson, and Ralph Weissleder, *Use of Magnetic Nanoparticles as Nanosensors to Probe for Molecular Interactions.* ChemBioChem, 2004. **5**: p. 261-264.

19. Hans, M.L., and A.M. Lowman, *Biodegradable Nanoparticles for Drug Delivery and Targeting.* Current Opinion in Solid State and Materials Science, 2009(6): p. 319-327.

20. Kam, N.W.S., Michael O'Connell, Jeffrey A. Wisdom, Hongjie Dai, *Carbon Nanotubes as Multifunctional Biological Transporters and Near-Infrared Agents for Selective Cancer Cell Destruction.* Proceedings of the National Academy of Sciences, 2005. **102**(33): p. 11600-11605.

21. Hergt, R., Silvio Dutz, Robert Müller, and Matthias Zeisberger, *Magnetic Particle Hyperthermia: Nanoparticle Magnetism and Materials Development for Cancer Therapy.* Journal of Physics: Condensed Matter, 2006. **18**: p. S2919-S2934.

22. Hainfeld, J.F., et al., *Radiotherapy Enhancement with Gold Nanoparticles.* J Pharm Pharmacol, 2008. **60**(8): p. 977-85.

23. Berbeco, R.I., W. Ngwa, and G.M. Makrigiorgos, *Localized Dose Enhancement to Tumor Blood Vessel Endothelial Cells via Megavoltage X-rays and Targeted Gold Nanoparticles: New Potential for External Beam Radiotherapy.*

International Journal of Radiation Oncology, Biology, Physics, 2011. **81**(1): p. 270-6.

24. Zhang, X.D., et al., *Irradiation Stability and Cytotoxicity of Gold Nanoparticles for Radiotherapy.* Int J Nanomedicine, 2009. **4**: p. 165-73.

25. McMahon, S.J., et al., *Radiotherapy in the Presence of Contrast Agents: A General Figure of Merit and its Application to Gold Nanoparticles.* Phys Med Biol, 2008. **53**(20): p. 5635-51.

26. Polf, J.C., et al., *Enhanced Relative Biological Effectiveness of Proton Radiotherapy in Tumor Cells with Internalized Gold Nanoparticles.* Appl Phys Lett, 2011. **98**(19): p. 193702.

27. Katti, K.V., et al., *Hybrid Gold Nanoparticles in Molecular Imaging and Radiotherapy.* Czechoslovak Journal of Physics, 2006. **56**: p. D23-D34.

28. Gibson, N., et al., *Radiolabelling of Engineered Nanoparticles for in vitro and in vivo Tracing Applications using Cyclotron Accelerators.* Archives of Toxicology, 2011. **85**(7): p. 751-773.

29. Wikipedia.org. *Decay Scheme*. 2012 [cited 2012 Aug. 18]; Available from: http://en.wikipedia.org/wiki/Decay_scheme.

30. Agency, N.E. *Janis*. 2012 [cited 2012 Aug. 18]; Available from: http://www.oecd-nea.org/janis/.

31. Zheng, Y., et al., *Radiosensitization of DNA by Gold Nanoparticles Irradiated with High-Energy Electrons.* Radiat Res, 2008. **169**(1): p. 19-27.

32. Zhang, X.D., et al., *Size-Dependent Radiosensitization of PEG-Coated Gold Nanoparticles for Cancer Radiation Therapy.* Biomaterials, 2012. **33**(27): p. 6408-19.

33. Xiao, F., et al., *On the Role of Low-Energy Electrons in the Radiosensitization of DNA by Gold Nanoparticles.* Nanotechnology, 2011. **22**(46): p. 465101.

34. Herbst, R.S., *Review of Epidermal Growth Factor Receptor Biology.* Int J Radiat Oncol Biol Phys, 2004. **59**(2 Suppl): p. 21-6.

35. Hudis, C.A., *Trastuzumab--Mechanism of Action and Use in Clinical Practice.* New England Journal of Medicine, 2007. **357**(1): p. 39-51.

36. Cancer, I.A.f.R.o. *GLOBOCAN 2008 Fast Stats - Section of Cancer Information*. 2008 [cited 2012 Aug. 18]; Available from: http://globocan.iarc.fr/factsheets/populations/factsheet.asp?uno=900.

37. Bazley, L.A. and W.J. Gullick, *The Epidermal Growth Factor Receptor Family.* Endocrine-Related Cancer, 2005. **12 Suppl 1**: p. S17-27.

38. Earp, H.S., 3rd, B.F. Calvo, and C.I. Sartor, *The EGF Receptor Family--Multiple Roles in Proliferation, Differentiation, and Neoplasia with an Emphasis on HER4.* Trans Am Clin Climatol Assoc, 2003. **114**: p. 315-33; discussion 333-4.

39. Tan, B.J.Y., et al., *Fabrication of Size-Tunable Gold Nanoparticles Array with Nanosphere Lithography, Reactive Ion Etching, and Thermal Annealing.* Journal of Physical Chemistry B, 2005. **109**(22): p. 11100-11109.

40. Jung, S.H., et al., *Preparation of Radioactive Core-Shell Type Au-198@SiO2 Nanoparticles as a Radiotracer for Industrial Process Applications.* Applied Radiation and Isotopes, 2010. **68**(6): p. 1025-1029.

41. Kumar, S., J. Aaron, and K. Sokolov, *Directional Conjugation of Antibodies to Nanoparticles for Synthesis of Multiplexed Optical Contrast Agents with both Delivery and Targeting Moieties.* Nat Protoc, 2008. **3**(2): p. 314-20.

42. Lim, A., A. Reed-Bogan, and B.J. Harmon, *Glycosylation Profiling of a Therapeutic Recombinant Monoclonal Antibody with Two N-Linked Glycosylation Sites using Liquid Chromatography Coupled to a Hybrid Quadrupole Time-of-Flight Mass Spectrometer.* Analytical Biochemistry, 2008. **375**(2): p. 163-172.

43. Wang, A., C.J. Wu, and S.H. Chen, *Gold Nanoparticle-Assisted Protein Enrichment and Electroelution for Biological Samples Containing Low Protein Concentrations - A Prelude of Gel Electrophoresis.* J Proteome Res, 2006. **5**(6): p. 1488-1492.

44. Hasenoehrl, C., et al., *Enhanced Detection of Gold Nanoparticles in Agarose Gel Electrophoresis.* Electrophoresis, 2012. **33**(8): p. 1251-1254.

45. Jans, H., et al., *Dynamic Light Scattering as a Powerful Tool for Gold Nanoparticle Bioconjugation and Biomolecular Binding Studies.* Anal Chem, 2009. **81**(22): p. 9425-9432.

46. Hoo, C.M., et al., *A comparison of Atomic Force Microscopy (AFM) and Dynamic Light Scattering (DLS) Methods to Characterize Nanoparticle Size Distributions.* Journal of Nanoparticle Research, 2008. **10**: p. 89-96.

47. Vysotskii, V.V., et al., *On the Feasibility of Determining Nanoparticle Concentration by the Dynamic Light Scattering Method.* Colloid Journal, 2009. **71**(6): p. 739-744.

48. Dasary, S.S., et al., *Highly Sensitive and Selective Dynamic Light-Scattering Assay for TNT Detection Using p-ATP Attached Gold Nanoparticle.* ACS Appl Mater Interfaces, 2010. **2**(12): p. 3455-60.

49. Geronimo, C.L. and R.I. MacCuspie, *Antibody-Mediated Self-Limiting Self-Assembly for Quantitative Analysis of Nanoparticle Surfaces by Atomic Force Microscopy.* Microscopy and Microanalysis, 2011. **17**(2): p. 206-14.

50. Helm, C.A. *Atomic Force Microscopy*. Biophysics of Soft Matter 2012 [cited 2012 Aug. 25, 2012]; Available from: http://www3.physik.uni-greifswald.de/method/afm/eafm.htm.

51. Wikipedia.org. *Atomic Force Microscopy*. 2012 [cited 2012 Aug. 25]; Available from: http://en.wikipedia.org/wiki/Atomic_force_microscope.

52. Steinhauser, I., et al., *Trastuzumab-Modified Nanoparticles: Optimisation of Preparation and Uptake in Cancer Cells.* Biomaterials, 2006. **27**(28): p. 4975-4983.

53. Mi, Y., et al., *Multimodality Treatment of Cancer with Herceptin Conjugated, Thermomagnetic Iron Oxides and Docetaxel Loaded Nanoparticles of Biodegradable Polymers.* Biomaterials, 2012. **33**(30): p. 7519-29.

54. Leyland-Jones, B., et al., *Pharmacokinetics, Safety, and Efficacy of Trastuzumab Administered Every Three Weeks in Combination With Paclitaxel.* Journal of Clinical Oncology, 2003. **21**(21): p. 3965-9371.

55. Gruaz-Guyon, A., O. Raguin, and J. Barbet, *Recent Advances in Pretargeted Radioimmunotherapy.* Current Medicinal Chemistry, 2005. **12**(3): p. 319-338.

56. Bayraktar, U.D., et al., *Simultaneous Measurement of ERalpha, HER2, and PhosphoERK1/2 in Breast Cancer Cell Lines by Flow Cytometry.* Breast Cancer Research and Treatment, 2011. **129**(2): p. 623-8.

57. Galanzha, E.I., et al., *In vivo Multispectral, Multiparameter, Photoacoustic Lymph Flow Cytometry with Natural Cell Focusing, Label-Free Detection and Multicolor Nanoparticle Probes.* Cytometry A, 2008. **73**(10): p. 884-94.

58. Watson, J.V., *The Early Fluidic and Optical Physics of Cytometry.* Cytometry, 1999. **38**(1): p. 2-14.

59. Biolegend , I. *PE Anti-Human CD340 (erbB2/HER-2) Antibody*. 2012 [cited 2012 Aug. 26]; Available from: http://www.biolegend.com/pe-anti-human-cd340-erbb2-her-2-3766.html.

60. Stausbolgron, B., et al., *Selective Assessment of in-Vitro Radiosensitivity of Tumor-Cells and Fibroblasts from Single Tumor-Biopsies Using*

Immunocytochemical Identification of Colonies in the Soft Agar Clonogenic-Assay. Radiotherapy and Oncology, 1995. **37**(2): p. 87-99.

61. Lu, F. and S. Wong, *Long Term Regeneration Capacity of Neural Stem Cells in Irradiated Adult Rat Spinal Cord: In vivo/in vitro Clonogenic Assay.* Radiotherapy and Oncology, 2005. **76**: p. S35-S35.

62. Zhang, X., et al., *A Novel Clonogenic-Assay for the Growth of Human Myeloma Cells in-Vitro.* Blood, 1994. **84**(10): p. A175-A175.

63. Franken, N.A.P., et al., *Clonogenic Assay of Cells in Vitro.* Nature Protocols, 2006. **1**(5): p. 2315-2319.

64. Ke, N., et al., *The xCELLigence System for Real-Time and Label-Free Monitoring of Cell Viability.* Methods Mol Biol, 2011. **740**: p. 33-43.

65. Quereda, J.J., et al., *Validation of xCELLigence Real-Time Cell Analyzer to Assess Compatibility in Xenotransplantation with Pig-to-Baboon Model.* Transplant Proc, 2010. **42**(8): p. 3239-43.

66. Urcan, E., et al., *Real-Time xCELLigence Impedance Analysis of the Cytotoxicity of Dental Composite Components on Human Hingival Fibroblasts.* Dent Mater, 2010. **26**(1): p. 51-8.

67. Science, R.A. *xCELLigence System*. 2012 [cited 2012 Oct. 7]; Available from: www.roche-applied-science.com.

68. Bouchat, V., et al., *Radioimmunotherapy with Radioactive Nanoparticles: First Results of Dosimetry for Vascularized and Necrosed Solid Tumors.* Medical Physics, 2007. **34**(11): p. 4504-4513.

69. Bouchat, V., et al., *Radioimmunotherapy with Radioactive Nanoparticles: Biological Doses and Treatment Efficiency for Vascularized Tumors with or without a Central Hypoxic Area.* Medical Physics, 2010. **37**(4): p. 1826-1839.

70. Nuttens, V.E., et al., *Determination of Biological Vector Characteristics and Nanoparticle Dimensions for Radioimmunotherapy with Radioactive Nanoparticles.* Applied Radiation and Isotopes, 2008. **66**(2): p. 168-172.

71. Föll, H. *Surface Reconstruction*. Semiconductor Technology 2012 [cited 2012 Aug. 29]; Available from: http://www.tf.uni-kiel.de/matwis/amat/semitech_en/kap_3/advanced/t3_3_1.html.

72. Varadan, V., et al., *Nanoscience and Nanotechnology in Engineering.* World Scientific, 2010: p. 50-51.

73. Park, P. *Surface Tension and Surface Energy*. Materials Engineering for Civil Engineers, CVEN 306 2012 [cited 2012 Nov. 11]; Available from: http://philippark.weebly.com/uploads/5/1/1/8/5118986/lecture_07_slide.pdf.

74. Pan, Y., et al., *Size-Dependent Cytotoxicity of Gold Nanoparticles.* Small, 2007. **3**(11): p. 1941-1949.

75. Marsh, M. and H.T. McMahon, *Cell biology - The Structural Era of Endocytosis.* Science, 1999. **285**(5425): p. 215-220.

76. Albanese, A., P.S. Tang, and W.C.W. Chan, *The Effect of Nanoparticle Size, Shape, and Surface Chemistry on Biological Systems.* Annual Review of Biomedical Engineering, Vol 14, 2012. **14**: p. 1-16.

77. Lu, B.L. and S. Torquato, *Chord-Length and Free-Path Distribution-Functions for Many-Body Systems.* Journal of Chemical Physics, 1993. **98**(8): p. 6472-6482.

78. Lafontaine, C., *Formalization of the Vdm Reification in the Deva Meta-Calculus - the Human-Leukocyte-Antigen Case-Study*. Programming Concepts and Methods, 1990: p. 333-368.

79. Weber, M., *Formalization of the Bird-Meertens Algorithmic Calculus in the Deva Meta-Calculus.* Programming Concepts and Methods, 1990: p. 201-231.

80. Filipe, V., A. Hawe, and W. Jiskoot, *Critical Evaluation of Nanoparticle Tracking Analysis (NTA) by NanoSight for the Measurement of Nanoparticles and Protein Aggregates.* Pharmaceutical Research, 2010. **27**(5): p. 796-810.

81. Markutsya, S., et al., *On Brownian Dynamics Simulation of Nanoparticle Aggregation.* Industrial & Engineering Chemistry Research, 2008. **47**(10): p. 3338-3345.

82. Humm, J.L., R.W. Howell, and D.V. Rao, *Dosimetry of Auger Electron-Emitting-Radionuclides - Report No-3 of Aapm Nuclear-Medicine Task Group No-6 (Vol 21, Pg 1901, 1994).* Medical Physics, 1995. **22**(11): p. 1837-1837.

83. Svaruna. *Solid Angle Pictures*. 2012 [cited 2012 Sept. 28]; Available from: http://withfriendship.com/user/svaruna/solid-angle.php.

84. Wolfram Research, I. *Sphere Point Picking*. Wolfram Mathworld 2012 [cited 2012 Oct. 3]; Available from: http://mathworld.wolfram.com/SpherePointPicking.html.

85. Koopman, B.O., *Hamiltonian Systems and Transformations in Hilbert Space.* Proceedings of the National Academy of Sciences of the United States of America, 1931. **17**: p. 315-318.

86. King, F. *Probability*. 2008 [cited 2012 Nov. 3]; Available from: http://www.cl.cam.ac.uk/teaching/0708/Probabilty/.

87. Isobe, T., Y. Ikeda, and H. Ohta, *Comparison of Sizes and Shapes of Tumor-Cells in Plasma-Cell Leukemia and Plasma-Cell Myeloma.* Blood, 1979. **53**(5): p. 1028-1030.

88. Milano, M.T., L.S. Constine, and P. Okunieff, *Normal Tissue Toxicity After Small Field Hypofractionated Stereotactic Body Radiation.* Radiat Oncol, 2008. **3**: p. 36.

89. Xu, X.G., B. Bednarz, and H. Paganetti, *A Review of Dosimetry Studies on External-Beam Radiation Treatment with Respect to Second Cancer Induction.* Physics in Medicine and Biology, 2008. **53**(13): p. R193-241.

90. Ijaz, T., et al., *Radiation Therapy of Pelvic Recurrence After Radical Hysterectomy for Cervical Carcinoma.* Gynecol Oncol, 1998. **70**(2): p. 241-6.

91. Papiez, L. and R. Timmerman, *Hypofractionation in Radiation Therapy and its Impact.* Medical Physics, 2008. **35**(1): p. 112-8.

92. Astrahan, M., *Some Implications of Linear-Quadratic-Linear Radiation Dose-Response with Regard to Hypofractionation.* Medical Physics, 2008. **35**(9): p. 4161-72.

93. Yuan, J., et al., *Hypofractionation Regimens for Stereotactic Radiotherapy for Large Brain Tumors.* Int J Radiat Oncol Biol Phys, 2008. **72**(2): p. 390-7.

94. Bartelink, H. and R. Arriagada, *Hypofractionation in Radiotherapy for Breast Cancer.* Lancet, 2008. **371**(9618): p. 1050-2.

95. Inyang, O.E., Reece, W.D., Poston, J.W., Walker, M.A., *Development of a Prompt-Gamma, Neutron-Activation Analysis Facility at the Texas A&M University Nuclear Science Center*, in *Department of Nuclear Engineering*2008, Texas A&M University: College Station, Texas.

APPENDIX

A.1 1-D Weight Function – Throwing Darts at a Dart Board

If we are throwing darts at a dart board of radius "R" and the impact location of the dart onto the board is random and isotropic with respect to area, the average location of impact is the center of the dart board ($r = 0$). If we instead ask, "what is the average distance between the bull's-eye (the center of the dart board) and the locations the darts land", the answer is different; it cannot be "$r = 0$" in this case, because that would require that every single dart hit the bull's-eye. We must now consider the weight function which describes the relative probability of the dart landing a distance "r" from the bull's-eye. In general, "$f(r)$" can be thought of as "what you are looking to find the average of". The solution to the problem is shown below. This solution should not be surprising, because the circumference on the dart board increases with radius by a factor of r, meaning that the answer must be between "$0.5R$" and "R".

$$\bar{r} = \frac{\int f(r)w(r)\,dr}{\int w(r)\,dr}$$

$$f(r) = r$$

$$w(r) = 2\pi r$$

$$\bar{r} = \frac{\int_0^R (r)(2\pi r)\,dr}{\int_0^R (2\pi r)\,dr}$$

$$\boldsymbol{\bar{r} \approx 0.66R}$$

A.2 1-D Nested Weight Function – Cosine

In this example we will calculate the average value of the cosine function from 0 to π radians. This problem is different from the previous examples in two ways: (1) the independent variable is nested within a function of "what we are looking to find the average of", i.e. the angle is nested within the cosine function, and (2) there is no preference to angle; i.e. the angle is isotropic, with all angles having the same weight. The solution may then be calculated as follows.

$$f(\varphi) = \cos(\varphi)$$

$$w(\varphi) = 1$$

$$\overline{\cos(\varphi)} = \frac{\int_0^{\pi} (\cos(\varphi))(1)\, d\varphi}{\int_0^{\pi} (1)\, d\varphi}$$

$$\therefore$$

$$\boldsymbol{\overline{\cos(\varphi)} = 0}$$